Department of Physics

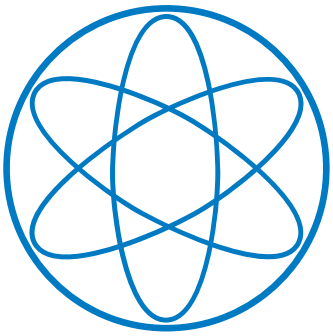

A Compact and Versatile Electrospray Ion Beam Deposition Setup

Advanced Sample Preparation for Experiments in Surface Science

Tobias Kaposi

Dissertation

Technical University Munich

Technische Universität München

Lehrstuhl E20 - Molekulare Nanowissenschaften und Chemische Physik von Grenzflächen

A Compact and Versatile Electrospray Ion Beam Deposition Setup

Advanced Sample Preparation for Experiments in Surface Science

Tobias Kaposi

Vollständiger Abdruck der von der Fakultät für Physik der Technischen Universität München zur Erlangung des akademischen Grades eines Doktors der Naturwissenschaften (Dr. rer. nat.) genehmigten Dissertation.

Vorsitzender:		Prof. Dr. Michael Knap
Prüfer der Dissertation:	1.	Prof. Dr. Johannes Barth
	2.	Prof. Dr. Ulrich K. Heiz

Die Dissertation wurde am 31.3.2016 bei der Technischen Universität München eingereicht und durch die Fakultät für Physik am 17.5.2016 angenommen.

Again the message to experimentalists is: Be sensible but don't be impressed too much by negative arguments. If at all possible, try it and see what turns up.

- Francis Crick

For Marlene

Abstract

Over the course of surface science's almost 100 year long history, a particular class of experimental problems, namely self-assembling organic molecules adsorbed on pristine surfaces, has earned special interest. Especially the fabrication and control of functional molecular films and nanoarchitectures have been a strong motivational driving force in this regard. For the express purpose of depositing organic molecules onto surfaces under ultrahigh vacuum (UHV) conditions organic molecular beam epitaxy (OMBE) has so far been the method of choice. OMBE, however, suffers from a severe limitation due to molecular thermolability, which renders deposition of high mass molecules impossible.

In order to push the boundaries towards molecules of arbitrary mass a specialized sample preparation setup utilizing the concept of electrospray ion beam deposition (ESIBD) has been developed and built during this thesis. In contrast to OMBE, this technique is of a more intricate nature and requires careful control of several closely intertwined system parameters. Due to the critical source processes being conducted at atmospheric pressure a differential pumping system has to be implemented. Ions then have to be transmitted through this using radio frequency (RF) driven ion guidance systems in order to minimize beam current losses. Critical parameters of the pumping and ion guiding systems have to be controlled using an embedded system with integral control capabilities. The setup presented here fulfills all of these requirements in an unprecedented compact and versatile manner. It has been used to conduct a series of proof-of-principle sample preparations using a well known molecule. Additionally, a series of STM experiments have been conducted using OMBE as the preparation technique in order to put the capabilities of this method into perspective.

Kurzfassung

Während der beinahe einhundertjährigen geschichtlichen Entwicklung der Oberflächenphysik hat sich die Klasse der selbstanordnenden organischen Moleküle auf hochreinen Oberflächen als Objekt wissenschaftlichen Interesses besonders hervor getan. Insbesondere die Herstellung und Modifikation von funktionellen Molekülschichten und Nanoarchitekturen waren treibende Kräfte dieser Entwicklung. Für die Deposition organischer Moleküle auf Oberflächen unter Ultrahochvakuum (UHV) war bisher die Organische Molekularstrahlepitaxie (OMBE) die Methode der Wahl. Diese ist jedoch limitiert aufgrund der thermischen Instabilität von Molekülen hoher molarer Masse, welche deswegen zur Deposition nicht zur Verfügung stehen.

Um die Deposition beliebig schwerer Moleküle zu ermöglichen wurde im Rahmen der vorliegenden Arbeit ein hoch spezialisiertes Präparationssystem entwickelt und aufgebaut, welches auf dem Prinzip der Elektrospray-Ionenstrahldeposition (ESIBD) beruht. Im Gegensazu zu OMBE ist dieses jedoch deutlich komplexer und setzt die präzise Steuerung meherer, stark verflochtener Systemparameter voraus. Da die Ionen-erzeugenden Prozesse bei Umgebungsdruck stattfinden ist der Bau eines differentiell gepumpten Kammersystems von Nöten, durch welches die erzeugten Ionen mithilfe von hochfrequent betriebenen Ionenleitern geführt werden müssen, um Verluste zu minimieren. Kritische Parameter des Pumpsystems und der Ionenleitenden Systeme müssen von einem embedded system mit umfassendem Steuerungspotential kontrolliert werden. Der hier präsentierte, überaus kompakte und flexible Aufbau erfüllt all diese Bedingungen und wurde bereits verwendet um eine Reihe erster Versuchsdepositionen mit einem wohl bekannten Molekül durchzuführen. Außerdem wurden in einer Serie von STM Experimenten, bei denen OMBE als Präparationsmethode verwendet wurde, die Fähigkeiten der beiden Techniken verglichen.

Contents

1

Introduction and Motivation

Nanoscience is the investigation and controlled manipulation of material systems which exhibit one or more of their three spatial dimensions in the nm range. Here, matter behaves differently, with material properties showing a strong dependence on system size and quantum mechanical effects. It is, today, one of the most busy fields of research even though its history only dates back to the early 1980's with Binnig and Rohrer's invention of the scanning tunneling microscope (STM) [1, 2] and the discovery of C_{60} [3], a relatively short time-frame compared to other scientific areas. This has largely been motivated due to the rapid developments in semiconductor technology, where upholding Moore's law [4] has now made the control of processes at the nanometer scale mandatory in order to reach a sufficiently small feature size, a development which had been predicted for quite some time [5]. In turn, a broad shift of focus towards this regime has occurred in other fields as well, such as chemistry and engineering in general (see below).

The field's spiritual roots go back to the beginnings of surface science [6, 7], with which it is closely related to quite some extent. Richard Feynman is often cited as the original instigator of research into nanoscience due to his immensely foresighted 1959 talk, "There's plenty of room at the bottom" [8], in which he predicted systems verging on science fiction then, some of which have been realized by now. His influence, however, has been found to be retro-fitted, very much akin to a classical *post hoc ergo propter hoc* fallacy, as the talk only really came to fame in the 1990's, well after the first groundbreaking experiments [9]. Whatever its true origins, nanoscience has now sprouted into a multitude of diverse sub-areas, spread out, for the most part, diffusely over the classical fields of chemistry, physics, and electrical engineering. Amongst its most heavily investigated topics are such diverse elements as: catalysis [10–12], quantum computing [13, 14], spintronics and magnetic information storage [15–17], molecular machinery [18–20], and even tribology [21, 22].

The Science of Molecules at Interfaces

One particularly interesting and much studied class of phenomena in nanoscience is the behavior of single molecules (or ensembles thereof) adsorbed on well-defined semiconductor or metal surfaces. Due to the predominance of electrostatic and dipole forces at these length scales an intriguing interplay between molecules and surface arises. This can manifest itself as an attractive interaction between molecules, leading to self-assembled structures exhibiting properties very much worth investigating in itself as molecular machines [23] or novel sources for the bottom-up fabrication of nanosized patterns [24]. The latter are often cited as promising candidates for etching templates or nano-sized beakers [25, 26]. However, because these structures consist of molecules with distinct chemical and/or physical properties frequently surpassing those of classical building materials, a whole meta-level of purposeful design possibilities arises. Why go to great lengths in making a molecular etching mask for nano-electronics, when you can "just as easily" fabricate a molecular transistor or circuit [27–29] using similar techniques, for example? The true power of self-assembled molecular architectures on surfaces thus lies in the possibility to combine form with function, as these two aspects, which are usually strongly separated in systems design, converge at the nano-scale.

The biggest challenge in designing such systems, which science has yet to overcome, lies in the reliable prediction of the aforementioned interactive behavior. Whether molecules will be attracted more or less to each other or even the surface depends strongly on their chemical nature and functional moieties, opening up a vast hyperspace of possible assembly and on-surface reaction pathways [30–32]. Minute changes in chemical composition and/or surface constitution can thus have a large influence on the resulting behavior upon adsorption. Although experienced researchers can usually design a molecule such that it behaves within certain predictable limits, a level of control needed to build truly complex systems is still very much out of reach. Finding general relationships, which govern these dependencies, is thus currently of great interest in both experimental and theoretical surface science [33, 34]. Furthermore, surface contaminations may also have a devastating impact, making the use of ultra-clean sample preparation and analysis techniques necessary.

More is More - A Motivation

In conjunction with the empiric nature of scientific research it would thus be beneficial to expand the scope of systems which can be investigated in order to arrive at far-reaching and universal correlations. This would, in turn, enable the tailored manufacture of nano-systems by means of a sort of nano-cookbook. It is exactly this proposed expansion of

scope, which represents the motivational basis for the present thesis. So far, only one sample preparation technique has been commonly used to deposit organic molecules on surfaces under ultra-clean conditions, namely organic molecular beam epitaxy (OMBE) [35]. However, this technique is, as will be shown later on, considerably limited in the scope of molecules available for deposition with it due to thermolability, which runs counter to the aforementioned desired expansion. Apart from that, it also features some other, more minor drawbacks, as we will see. Suitable alternative techniques, which allow for thermolabile molecules to be deposited and subsequently investigated thus have to be found and developed.

In the following chapters one such technique, called electrospray ion beam deposition (ESIBD), will be presented and discussed. In chapter 2 an overview and theoretical discussion of all relevant techniques, including both mentioned preparation methods as well as STM, will be given. During this thesis, a series of STM experiments with the aim of investigating different molecules adsorbed on noble metal substrates in ultrahigh vacuum (UHV) have been conducted, using the traditional OMBE deposition method. These molecules were specifically chosen to be at the limit of OMBE's capabilities. Results of these investigations will be presented in chapter 3 with a special emphasis on such findings, which directly or indirectly result from complications during sample preparation and thus highlight OMBE's limitations.

Furthermore, in order to push back these boundaries and embark on the road to sample preparations with thermolabile molecules an ESIBD setup was developed and built during the present thesis. In contrast to OMBE's straightforward approach, however, ESIBD is a complex process necessitating precise control of many intricately interacting system parts. This starts at the purely mechanical level of a differential pumping system, which is intertwined closely with a series of ion beam guiding devices. These, in turn, are in need of a suitable electronic power supply, which should itself be precisely controllable along with several other system parameters. An almost completely custom-made system consisting of mechanical and electronic hardware, an embedded control system, as well as a suitable control software has been developed and built. It is being presented and discussed in detail in chapter 4 and has already been successfully used to conduct proof-of-principle depositions of a well known molecule onto coinage metal surfaces, which were subsequently investigated using STM. It is, in contrast to setups used for similar purposes, extremely compact and versatile, allowing connection to a multitude of different experimental setups. However, ample room for improvements exists and some refinement and reconstruction proposals will be given alongside the conclusion in chapter 5.

2

Fundamentals and Theory

One rather striking similarity between almost all surface science techniques is the need for a special sample preparation procedure in order to conduct measurements on a well defined system. Some spectroscopic techniques, which allow the experimentalist, under certain circumstances, to simply place an otherwise untreated sample into the setup and start measuring may be the rare exceptions to this rule [36–39]. While some preparative procedures, such as scotch-tape exfoliation [40, 41], are very straightforward, in the great majority of cases a more or less time consuming and elaborate process has to be followed long before the actual experiment can take place. Sometimes this procedure is even more complex and lengthy than the measurement itself, this being largely due to the fact that physics on the atomic scale works very fast and thus probing phenomena in surface science often allows for quite short data acquisition times. It is also a very crucial part of the overall procedure as, depending on its complexity, different degrees of errors can be made by the experimenter which sometimes only become apparent after the measurement when analyzing the data [42]. As today there is a sheer plethora of surface science techniques in use, many of which are being utilized in rather different, specialized fields of research, a comparable amount of sample preparation techniques has been developed. For example, scanning probe microscopy with its relatively young history of about 30 years has already spawned dozens of "sub-techniques" focused on different particular working effects [43, 44], most of which make use of specialized sample preparation procedures with those commonly used in semiconductor research probably being the most time consuming ones. Due to this significant importance it is of course worthwhile to invest time and effort into the continued development of sample preparation techniques in order to both improve experimental data as well as establish new venues for scientific research. In the following chapter, the theoretical basis of one of the most prominent representatives of all scanning probe techniques and two complementing sample preparation procedures will be laid out.

2.1 Scanning Tunneling Microscopy

Scanning Tunneling Microscopy is the forefather of all scanning probe microscopy (SPM) techniques and has since its invention in the early 1980's by Binnig and Rohrer [1, 2] lead to a downright deluge of experimental findings in various sub-areas of surface science and the development of many further techniques [43].

2.1.1 Theoretical Aspects

STM's core functionality, namely the ability to atomically resolve a sample surface [45], stems from the effect of quantum tunneling whereby electrons can seemingly pass through an energy barrier, which would be considered insurmountable in classical mechanics. Figure 2.1 schematically represents an electron tunneling from left to right through a barrier with potential energy V_B higher than the wave function's energy eigenvalue E_Ψ. To the left and right of the barrier the wave can propagate freely. Within the barrier however, one observes an exponential decay, leading to a reduced probability density on the right hand side ("after" tunneling).

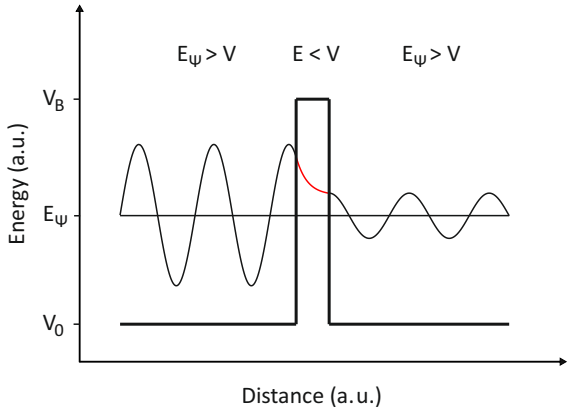

Figure 2.1: Sketch of an electron tunneling through an energy barrier.

This phenomenon had first been discovered and described in theory by Hund in 1927 for energetically equivalent states in isomers [46] and was almost immediately used to explain the process of alpha decay [47, 48] utilizing a then novel method developed by Wenzel, Kramer, Brioullin and others (the WKB method) to approximate non-constant potentials [49–52]. Shortly after Hund's findings it also played a prominent role in Fowler's and Nordheim's theoretical explanation of field electron emission [53]. The effect was first theoretically proposed to be applicable to the contact resistance between two metals separated by a thin insulating layer in 1930 by Frenkel [54], a theory improved upon by Holm in 1950 [55]. It was first experimentally observed in p-n

junctions of germanium [56] and later in superconducting metal-oxide-metal samples [57, 58], quite some time before observations in a metal-vacuum-metal environment could be made [59]. This hold-up was largely attributed to the need for very low vibrational disturbance [60] as stable metal to metal distances of under 100 Å had to be provided, but a first working prototype setup for measuring surface microtopography was then developed very quickly [61].

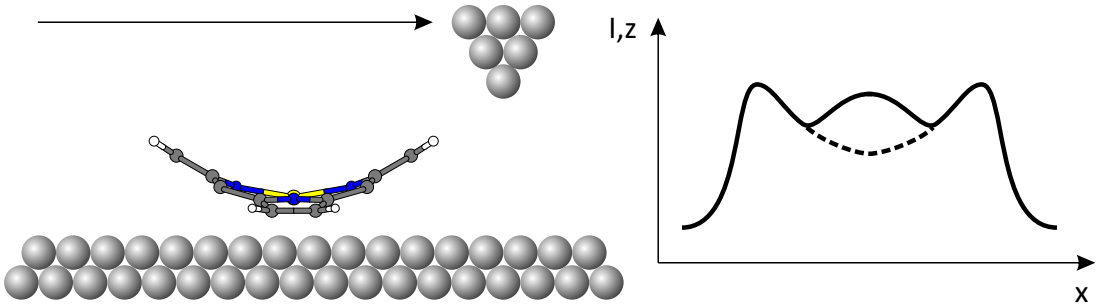

Figure 2.2: Schematic representation of the tip-sample interaction in the STM scanning process. The left side shows a metal single crystal surface with an organic molecule adsorbed and the tip scanning over it. The graph on the right hand side represents the resulting tunneling current or tip height, depending on the measurement mode (see Section 2.1.2). As the resulting data are a convolution of topography and electronic structure one may obtain additional features like the local maximum in the middle where topographically one would expect something more akin to the dashed line.

The experimental power of vacuum tunneling electrons comes from the fact that the wave function features an exponential decay characteristic in the barrier. If tunneling electrons are collected as a current and its magnitude is measured, this results in an exponential dependence of current on the vacuum barrier's width which allows for high vertical resolution and thus contrast as the current passing through a typical barrier of 3-5 eV changes by approximately one order of magnitude over the distance of just 1 Å [43, 62]. This, now, is the working principle of scanning tunneling microscopy, wherein a sharp tip is scanned across a sample surface at distances in the Å regime and the resulting tunneling current is amplified and measured, thus generating a digital image of the sample surface (see figure 2.2). The microscopic course of events, as is so often the case, is of course more complicated than this simple one-dimensional model. Apart from tip-sample distance a multitude of other factors play both minor and major roles influencing the magnitude of the actual tunneling current. Most prominent of these is the local density of electronic states (LDOS) at the Fermi level $\rho_s(E_F)$, which greatly influences the tunneling current. Areas of high LDOS result in high tunneling probability and vice versa, which leads to a proportional dependence of tunneling current

I_t on $\rho_s(E_F)$ [43]:

$$I_t \propto V\rho_s(E_F)\exp\left[-2\frac{\sqrt{2m(V_B-E_\Psi)}z}{\hbar}\right] \propto V\rho_s(E_F)\, e^{-1.025\sqrt{V_B}z} \tag{2.1}$$

with bias voltage V and electron mass m. This, especially in the investigation of molecules on surfaces, leads to a convolution of topographic and electronic data in the resulting image as is illustrated in figure 2.2 where the current measured by scanning over an adsorbed molecule displaying a U-like shape actually contains a third maximum in the middle because of a high local electron density due to chemical composition. The assiduous experimenter thus has to take great care in interpreting his or her experimental data so as not to arrive at false conclusions. Of course, the tip shape and density of states may also influence the results, but Tersoff and Hamann showed that (2.1) is valid under some assumptions, namely low bias and temperature, approximation of the tip wave function as a spherical, s-type wave function, and that $\rho_s(E_F)$ is actually probed at a distance of $z+R$ to the sample, where R is the radius of the tip, or in other words in the middle of the tip [63, 64]. This is an important first approach to explaining the high spatial resolution of STM even though tip apexes are usually in the range of 100 to 1000 Å, although a more localized d-state of the tip also plays a significant role in this regard [43, 65–67]. A further consequence of (2.1) is that:

$$\frac{dI}{dV} \propto \rho_s(E_F) \tag{2.2}$$

a direct proportionality between LDOS and differential conductance. This relation is an important implication allowing acquisition of so-called scanning tunneling spectra, as it can be expanded to LDOS at energies different from E_F (see section 3.1.2).

2.1.2 STM Control

As groundbreaking and expansive as STM's working principles may appear, its actual implementation is just as important to obtain solid experimental results. First and foremost one must be capable of precisely controlling tip position and movement. This is commonly achieved by utilizing piezoelectric actuators for all three degrees of freedom which can be controlled precisely by applying a voltage boosted by a HV amplifier. Different designs of such piezo-stages are available on the market and have been the focus of intensive research since the advent of scanning probe microscopy [69–73]. All systems however share a common basic structure, an example of which is shown in figure 2.3, representing one of the STM setups used within the framework of this thesis which is commercially available from SPS-Createc GmbH and was initially developed by Meyer [68, 74]. The whole custom-built machine complete with liquid He cryostat

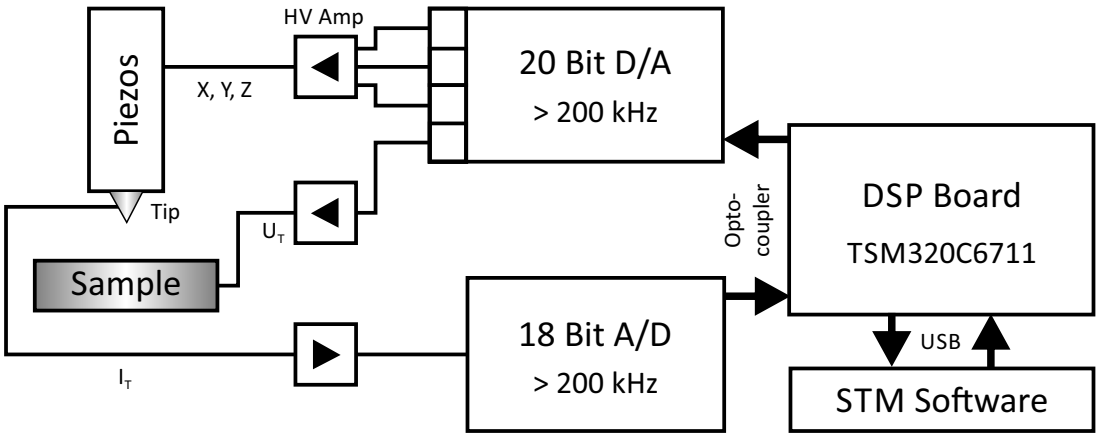

Figure 2.3: Working diagram of the SPS-Createc STM setup used in this thesis. Control voltages and tunneling current read-out are generated and, respectively, processed by the digital signal processor (DSP) board which constantly communicates with the measurement software via USB [68].

and additional facilities for sample handling and preparation has been described in more detail elsewhere [75, 76]. The second setup used in this thesis is custom-built as well, but features a commercially available variable-temperature STM unit by SPECS GmbH [77]. This machine has been described in detail in other works as well [78, 79]. Further information on experimental procedures can be found in appendix A.1.

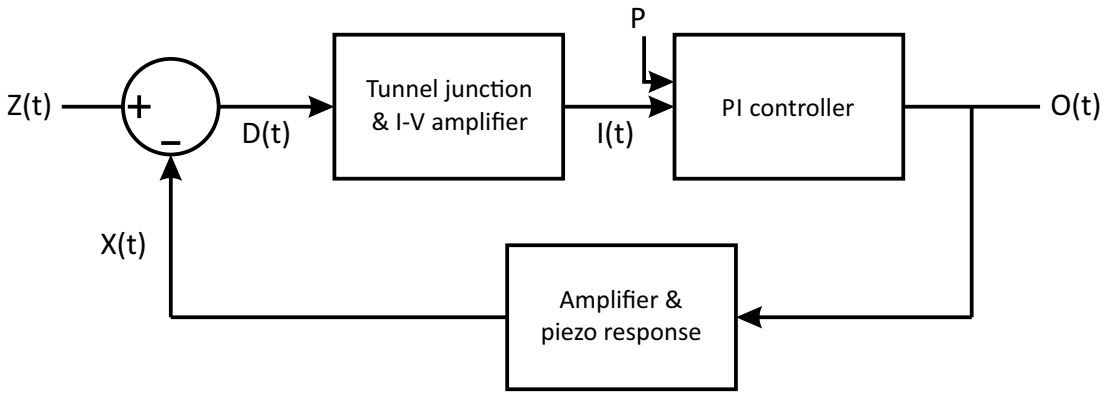

Figure 2.4: Flow chart of a simple PI feedback loop model to control tip-sample distances in constant current mode. From [80] with modifications.

Basically, there are two fundamental working modes in STM: constant height and constant current mode. In the first one the tip is held at a constant height while scanning and the resulting tunneling current used to construct the image, while in the second the tip-sample distance is continuously adjusted in order to hold the current constant. The second mode is the one which has been used most commonly within the framework of this thesis. In constant current mode the tip height as a function of lateral position is

used to construct the image. This mode is the one more commonly used as it effectively prevents the tip from crashing into the sample at sudden changes in topography. It does, however, make the use of a more or less sophisticated proportional-integral (PI) feedback loop necessary which constantly calculates deviation of the tunneling current I(t) from a constant set-point and adjusts the tip-sample distance D(t) accordingly by changing the z-piezo's driving voltage. In the model shown in figure 2.4 at every sampling point t the sample height Z(t) is subtracted from the piezo height X(t) and the resulting distance logarithmically converted into the tunneling current I(t). This is then compared to the set-point P and the resulting output O(t) in turn applied to the piezo amplifier. Note, that this represents a theoretical control setup for modeling the PI feedback response in a generic SPM setting including e.g. AFM or others, where no physical tunneling current is being acquired. In an actual STM setup the set-point would be compared directly to the measured tunneling current [80].

2.1.3 Sample Geometries

As is the case for piezo-stages there is likewise a multitude of different sample holders for all kinds of SPM setups available on the market. Two different ones have been used during this thesis, they are shown in figure 2.5. In order to reduce vibrational interference sample holders are usually built in a somewhat sturdy fashion as the one from SPS-Createc (fig. 2.5a) shows. The sample can be heated via direct contact to an oven which in turn is driven by a simple heating wire coiled up inside a ceramic part (not clearly visible in the drawing) which makes for reasonable thermal retention. Heating wires as well as a thermocouple attached to the oven are fed through ceramic inlays to reach the back contacts. Whenever the sample is clamped to a manipulator spring-loaded contacts on said manipulator provide contacting to electrical feed-throughs in the manipulator flange. Mounting the actual sample to the holder involves a series of complicated procedures, including soldering and spot-welding at multiple locations.

The SPECS holder (fig. 2.5b) relies on sandwiching the sample between two Mo plates using screws. In this case, a thermocouple can be spot-welded to the bottom plate and fed in such a way through a ceramic block opposite the fixture where the manipulator attaches that it forms exposed ends on the ceramic, which can again be contacted by some spring-loaded counterpart. This makes measuring the sample temperature impossible while attached to a manipulator, but as this geometry relies on indirect electron beam heating special sample heating facilities in the chamber have to be used or a sample holder gripping the sample from the ceramic side constructed

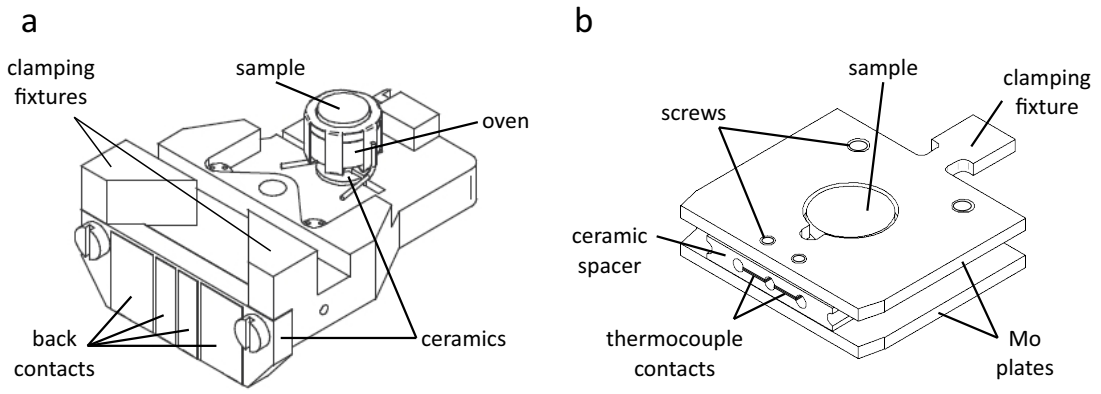

Figure 2.5: Isometric drawings of the two STM sample holders used in this thesis. **a** - SPS-Createc sample holder with direct Joule heating oven. In practice a thermocouple is spot-welded to the oven as close as possible to the sample. Both thermocouple and heating wires are soldered to the back contacts on the hidden side of the back ceramic. From [75] with modifications. **b** - SPECS sample holder design. Thermocouple contacts are created by repeatedly threading the strands through holes in the ceramic spacer. Both images have different scales, the samples are actually of similar size.

anyway. Regarding experimental procedures appendix A.1 contains more information on sample cleaning.

2.1.4 A Few Words on Commensurability

Some important practical aspects of the technique have been mentioned now, but data analysis has been neglected so far. A common point of interest when investigating layers of self-assembling molecules on surfaces is to check for commensurability of the assembly. This is given if its periodicity matches the periodicity of the underlying crystal in such a way that every molecule is adsorbed on a similar site relative to the crystal lattice. If commensurability is not formed in such a system usually a characteristic Moiré pattern emerges due to periodicity between surface and assembly arising on a much larger scale. Adsorption sites then change gradually from molecule to molecule which can lead to topographical corrugation as well as gradual changes in LDOS, both of which can be observed in the resulting image. A sort of in-between state exists, however, where adsorption sites change back and forth between adjacent molecules in an ABAB fashion. Here, no Moiré pattern emerges, we will thus call it quasi-commensurate. Whatever the state of commensurability of a system is, it arises due to either molecule-sample or molecule-molecule interactions being predominant and is thus a good indicator to gauge these interactions [81, 82].

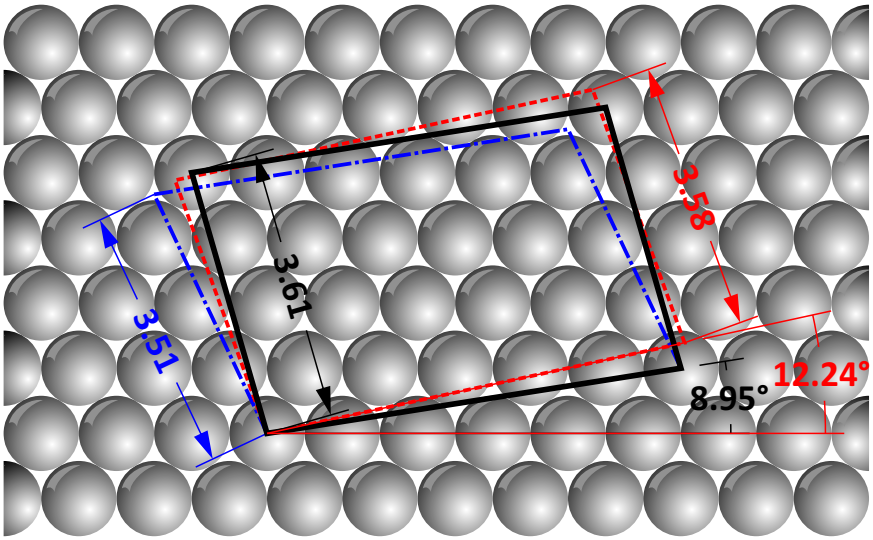

Figure 2.6: A simple method to check for commensurability in an investigated system by trying to fit an experimentally determined unit cell to the underlying crystal lattice. Measured lengths are given in multiples of a fictitious lattice constant. The red dashed line represents the unit cell measured from experimentally acquired data, both the blue and the black outline are possible solutions with the blue one being quasi-commensurate.

Checking for commensurability is often carried out in a very time-consuming and cumbersome way by overlaying a model of the assembly onto a model of the crystal in some image processing software suit and then fiddling around with the relative angles and precise size of the images in order to get them to align. Within this thesis a much more straightforward approach has been utilized wherein first the assembly's unit cell dimensions are measured from a high resolution STM image with as much accuracy as possible. It is worth mentioning here that angles are notoriously more challenging to measure accurately than distances, because overlaying an angle-measuring grid is an inherently approximating method whereas measuring distances can be accomplished very repeatably by averaging several line profiles. Relative errors for distances are usually around 3 % while measured angles have been found to deviate by some 5° when conducting data analysis during this thesis, although they may be more precise in other systems. Nevertheless, a rough estimate of the angle formed between the crystal's dense-packed directions and the unit cell vectors has to be made. This can be obtained by controlled crashing of the tip into the sample such that an indentation of a few tens of nm is formed. The sides of this indentation will be parallel to the crystal's dense-packed directions and can thus yield the crystal's orientation relative to the image axes. If the tip is crashed more forcefully into the sample even larger dislocation lines will be produced from which orientation angles can be measured more precisely. The resulting unit cell is then simplified to the corresponding tetragon and one of its corners fixed to

a random adsorption site (see figure 2.6) with the unit cell rotated relative to the lattice accordingly. From there it is quite easy to see if a possible commensurate solution to the problem exists which still satisfies the STM calibration's accuracy.

In the example shown one would rather go with the black solution for two reasons: one, it is the commensurate one whereas the blue one is only quasi-commensurate and two, and more importantly, the relative deviation from the measured model is only half as big. Note, that the relative angles have much less significance compared to the length, as both solutions deviate from the measurement by a comparable amount which is well within the range of accuracy for measuring angles from an STM image. As this approach nicely puts the problem into the realm of computational geometry one could very easily write a short piece of code which automatically calculates possible solutions and shows whether or not they are within a reasonable margin of error with regard to the setup's calibration.

2.2 Organic Molecular Beam Epitaxy

By and large, organic molecular beam epitaxy (OMBE), more generally called organic molecular beam deposition, is the single most prevalent method for the clean deposition of sublimable organic molecules in ultra-high vacuum setups onto samples which can then be investigated by a variety of surface physical techniques such as the aforementioned STM and others [35, 83, 84]. At its core the process is rather straightforward. The molecular powder to be investigated is heated, while contained within a quartz or other inert crucible in order to minimize contamination and unwanted chemical reactions, and sublimates into the vacuum chamber, usually through some form of shutter or aperture to reduce contamination of the system. A sample is placed conveniently within the resulting beam of molecules such that deposition can occur (see figure 2.7a, shutter omitted for simplicity). Whether or not the overall process indeed leads to epitaxial results or not depends on the pair of substrate and molecule chosen [85], so "organic molecular beam deposition" seems to be the more suitable description. For reasons of continuity and consistency with previous works however "organic molecular beam epitaxy" and its abbreviation will be used throughout this thesis.

Duration of the deposition as well as sufficient sublimation temperature of course depend on the molecule to be investigated and can range from minutes to several hours and from room temperature to a few hundred °C, respectively. Purity of the powder is usually ensured by a process referred to as "degassing" wherein the powder is heated prior to the actual preparation in order to evaporate chemical byproducts and contaminants. Heating can be facilitated via both direct or indirect methods and is commonly

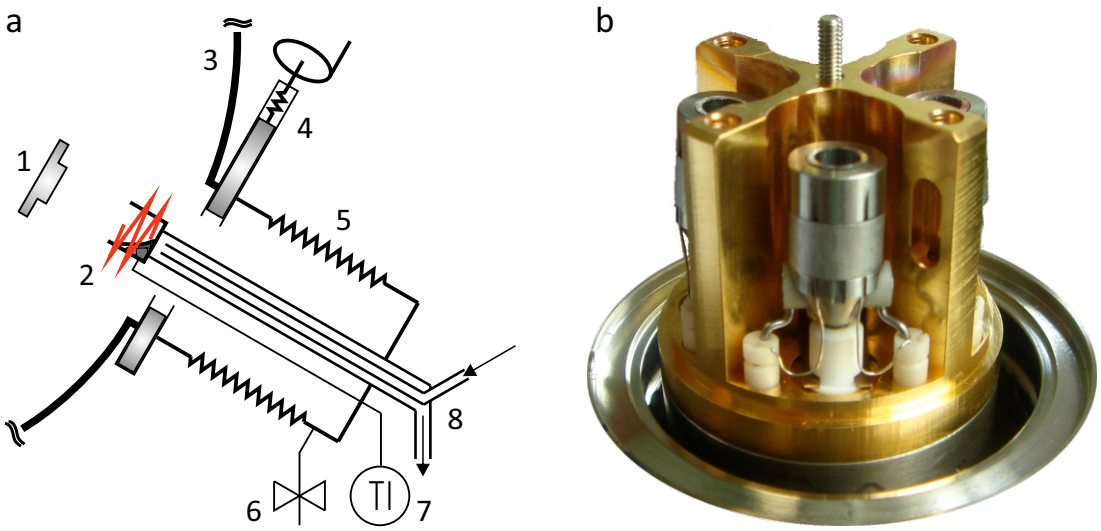

Figure 2.7: **a** - Schematic drawing of an organic molecular beam epitaxy setup showing its crucial components: 1 - sample, 2 - heated crucible, 3 - chamber wall, 4 - gate valve, 5 - bellow, 6 - pumping valve, 7 - temperature sensor, 8 - water cooling system. **b** - Photo of an actual OMBE with three ovens and a metal evaporator (hidden in the back) in four separate compartments. Heating and thermocouple contacts can be seen below the ovens and quartz crucibles inside them. The threaded rod on top is used to mount a simple rotary shutter.

checked by direct measurement with an incorporated thermocouple, making a simple form of temperature control loop possible if the thermocouple readout is digitized with an analog-to-digital converter. Depending on the type of heating method such systems tend to be rather slow in response, thus a simple PI controller is usually a sufficient software solution. However, if direct heating is applied to the oven and the thermocouple is in electrical contact to the heating power supply care has to be taken to measure the thermoelectric voltage with a floating unit. In this way the heating voltage will not be read as a thermoelectric voltage which would otherwise significantly skew the temperature readings. Appendix B.1 contains a wiring diagram and PCB layout for a basic control unit capable of both digitizing thermoelectric voltages with a small superimposed heating voltage as well as generating a control voltage to drive an external heating power supply.

In order to reduce chamber contamination from degassing surfaces, as well as unnecessary loss of material, a water cooling system is often added to the design to keep most of the apparatus cold and allow instant cool-down of the remaining powder after the preparation has been finished. This can also be used to keep further crucibles containing different molecules cool, which are commonly employed because such a setup is integrated into the vacuum chamber to a certain degree and changing different molecu-

lar species can be a tedious maintenance job. Figure 2.7a thus also shows a gate valve, bellow and pumping valve needed to routinely disconnect the OMBE from the main chamber and change molecules. Such a procedure requires at least a mild bake-out before opening the gate valve again and usually takes one day. Figure 2.7b shows a photo of the "inner workings" of an actual OMBE with three ovens available for holding quartz crucibles as well as an additional metal evaporator which simply consists of a Tungsten filament around which a suitable metal wire can be wound. These four compartments are separated in order to prevent cross-contamination between crucibles which of course could otherwise lead to erroneous experimental data.

Apart from the rather cumbersome way of changing molecules there are several other drawbacks to this method, many of which will be discussed in much more detail in section 3.3, but some prominent ones certainly warrant mentioning here. For sure the most limiting factor in OMBE is inherently given by the need to sublimate organic molecules which works reasonably well for sufficiently small (that is to say, low in molecular mass) species, but becomes more and more complicated and eventually impossible for bigger molecules which tend to undergo cracking or polymerizing reactions at elevated temperatures. Furthermore, deposition parameters are often hard to estimate for novel substances and even with a previously investigated species these may vary over time as the crucible filling is reduced or parts of the substance undergo some sort of detrimental reaction. There is also the matter of cleanliness of the preparation as sometimes impurities may still be contained in the molecular powder which are hard or impossible to eliminate even with thorough degassing of the substance. All of these disadvantages, but mainly the method's limitation to molecules below around 1000 $\frac{\mathrm{g}}{\mathrm{mol}}$ call for a more flexible and powerful alternative.

2.3 Electrospray Ionization

Generating ions from nonvolatile compounds has been of scientific interest for over fifty years and this has generally been accomplished by using desorption techniques such as laser desorption (LD), fast atom bombardment (FAB), plasma desorption (PD), matrix-assisted laser desorption/ionization (MALDI) and others [86]. Most of these techniques however, are limited to a certain range of molecular masses or classes of molecules, and/or experimentally very challenging, such as field desorption for example [87]. They also tend to generate only very low ion beam currents which, for their common purpose as ion sources in mass spectrometry [88], tends not to be a major drawback. This does however limit their use as ion sources for deposition purposes as it would lead to disproportionately long sample preparation times, a circumstance which

especially in ultrahigh vacuum setups is considered a major drawback due to continued contamination of the sample by residual background gas. Fortunately, an alternative has been under development since the 1960's: electrospray ionization (ESI).

In essence, the process of ESI involves pumping a solution of molecules through a needle into a high electric field. The electrostatic forces acting upon the liquid result in a spray, with ions subsequently being generated from the spray's charged droplets (see section 2.3.2). The technique's roots date back to 19th's century physics with both the Plateau-Rayleigh instability as well as the Rayleigh limit playing a major role at the core of the process [89–91]. The next crucial steps were Zeleny's observations of liquid surfaces under the influence of an applied charge [92, 93], but although some additional findings were made in the following decade [94, 95] it took almost 50 years until Taylor developed a theory to describe the behavior of such surfaces during the 1960's while underpinning his findings with very demonstrative experimental data [96–99]. During this time Dole first reported the use of electrospray ionization as an ion source for mass spectrometry (ESI-MS) [100], a combination which was greatly improved by Fenn and coworkers during the 1980's [101–103]. As a deposition method electrospraying has had a history since the 1950's when it was used in nuclear physics as a fabrication technique for thin radioactive emitters [104], but it was only after the advent of ESI-MS that it's worth was really recognized, especially for preparing samples of polymers and biomolecules for all sorts of analytical investigations [105–108].

2.3.1 Spray Modes

A schematic view of some of the fundamental processes in electrospray ionization can be seen in figure 2.8. The overview sketches a fictional syringe supplying analyte solution to the spraying needle to which a high electrostatic potential is applied. The counter electrode across from it may serve an additional purpose as atmospheric pressure interface into the first differentially pumped vacuum chamber if the ESI source is used in conjunction with MS or other systems which operate in a vacuum environment. Depending on the sign of the high voltage applied to the needle positive or negative spray modes are possible, wherein also either positive or negative ions will be produced, respectively. All basic principles are similar for both modes, thus, for the sake of clarity, from now on all considerations and discussions will be made pertaining to the positive mode.

The zoomed insert depicts (not to scale) the microscopic processes. Due to the strong electrostatic force acting on the solvent a so-called Taylor cone is formed at the needle which represents the system's equilibrium state between electrostatic force

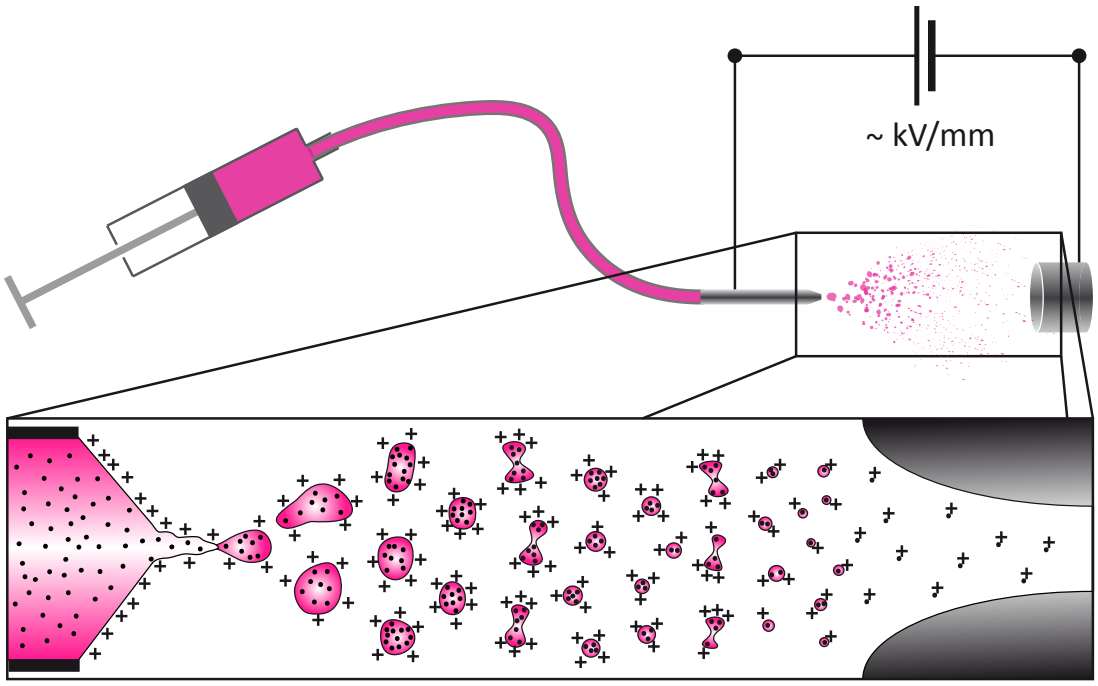

Figure 2.8: Sketch of ESI's "inner workings" showing the characteristic Taylor cone with a very short jet and droplets undergoing repeated cycles of solvent evaporation and Coulomb fission until only charged molecules are left over to enter the atmospheric pressure interface to the right. From [109] with modifications.

and surface tension [110]. Once a certain threshold potential is overcome the surface tension is too weak to completely compensate the electrostatic pull and due to some perturbation the cone begins ejecting charged liquid towards the counter electrode. The exact manner of this ejection depends on a series of parameters such as applied potential, pumping speed, viscosity and conductivity of the liquid, and a range of different spray regimes has been observed experimentally [111, 112]. There is ample evidence that even early stage phenomena such as these spray modes as well as inherent electrochemical processes within the needle can influence the nature and chemistry of generated ions [113–115], a strong testament to the technique's immanent intricacies. One particularly stable spray mode is the so-called cone-jet mode where a fine jet originating from the cone eventually destabilizes into a spray of fine droplets (see figure 2.9).

2.3.2 Ion Generation

How actual ions are formed from the spray's resulting droplets is still a matter of some debate and several models exist (see further below), however, a common feature of sprayed droplets in a strong electric field is the phenomenon of Coulomb fission [116]. Due to their high curvature droplets have high evaporation rates, but their initial charge

stays more or less constant and has to be accommodated on an ever shrinking area. Already Rayleigh showed that a spherical, charged drop is stable so long as the charge is below the so-called Rayleigh limit q_R [91]:

$$q_R = \sqrt{8\pi^2\epsilon_0\gamma d^3} \tag{2.3}$$

with vacuum permittivity ϵ_0, surface tension γ, and droplet diameter d.

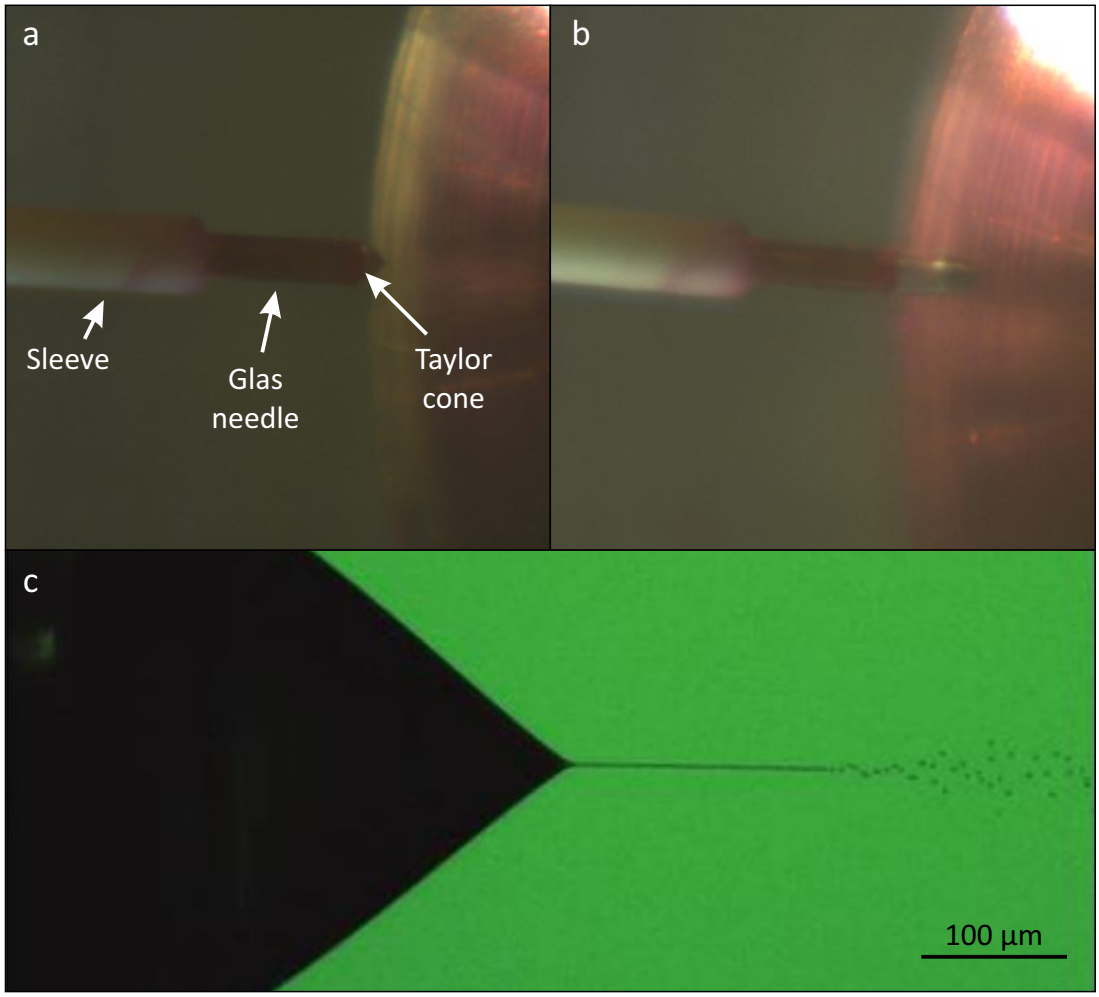

Figure 2.9: Photos of different Taylor cone modes, a and b taken during experiments on the setup used and developed in this thesis, c is from [113] with modifications. **a** - Taylor cone in stable cone-jet mode. **b** - Elongated Taylor cone at a higher voltage. This mode is much less stable and frequently leads to irreversible breakaway of the cone which, due to a hysteretic behavior, necessitates re-adjusting the voltage. **c** - Close-up of the stable cone-jet mode which can be clearly seen to break up into very fine droplets.

Once a sufficient amount of solvent has evaporated and the Rayleigh limit is overcome the droplet in turn ejects a so-called Rayleigh jet to again increase its surface to volume ratio and form yet another stable state with $q < q_R$. This process of solvent

evaporation and Coulomb fission can, in principle, continue even outside of the electrostatic field, as small perturbations at the droplet surface suffice to initiate Rayleigh jet formation. For the subsequent generation of ions there are, as mentioned above, three major models in use and these had been wildly contested until recently [117–119], as it became apparent that ions may be generated differently depending on certain circumstances. See figure 2.10 for a descriptive representation of these models and [120] for a comprehensive review on the subject from which some of the following standpoints have been collated.

Ion Evaporation Model (IEM): In this model an analyte molecule of low molecular weight is already ionized inside the droplet by protonation (usually organic acids are added to electrospray solutions to facilitate protonation and increase conductivity) and is ejected out of it through acceleration by the droplet's own electric field [121]. This process shows some similarities to Coulomb fission, thus a distinction between the two may be impossible for droplets in the nano-size regime [122].

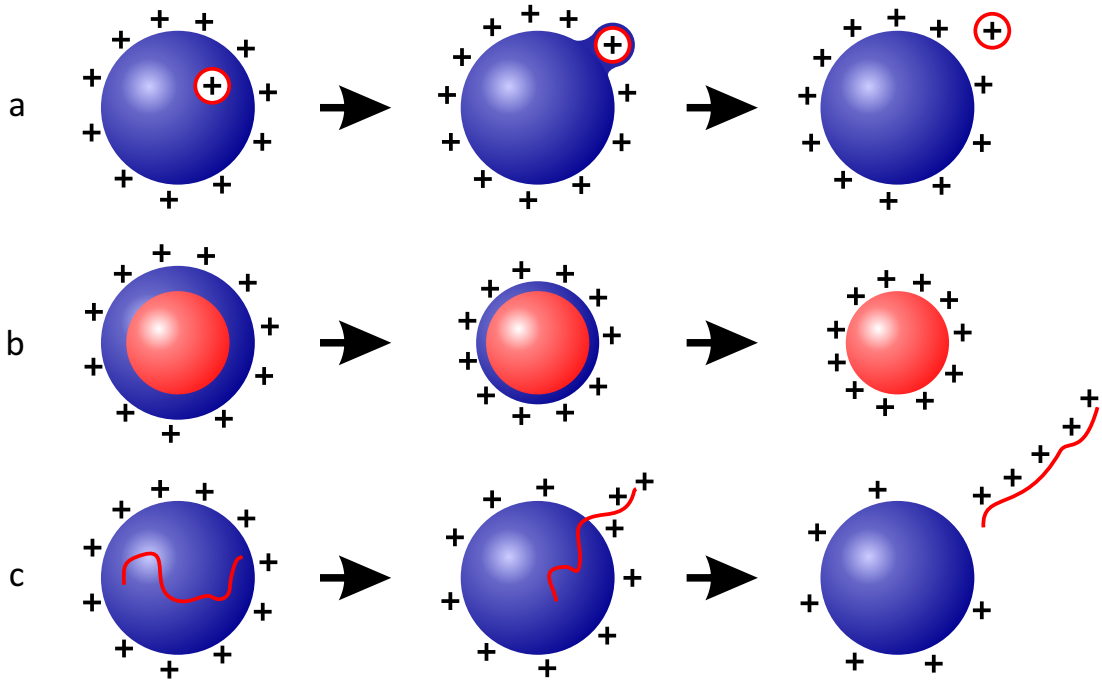

Figure 2.10: Overview of the three most commonly used models of ion generation in ESI. **a** - Ion evaporation model (IEM). **b** - Charged residue model (CRM). **c** - Chain ejection model (CEM). From [120] with modifications.

Charged Residue Model (CRM): As IEM seems to be a suitable model for ions of low molecular mass CRM is its counterpart for large, globular molecules which remain inside the droplet until even the last solvent layer has been evaporated and the remaining surface charge is transferred to the molecule, thus forming the analyte ion. As for

some ions charge states beyond the Rayleigh limit have been observed it is assumed that during the droplet shrinking process in CRM small ions are able to carry the excess surface charge and may be emitted via IEM, thus forming a combined CRM-IEM process [123].

Chain Ejection Model (CEM): Lastly, this model explains the generation of ions from long, unfolded and slightly hydrophobic polymer chains. For these the droplet presents an energetically unfavorable environment which causes them to drift towards the surface. There, they are partially charged and ejected step-wise while acquiring more and more charge. This difference in ion generation processes between folded and unfolded proteins is assumed to play an important role in the latter's disproportionately higher MS intensities [124].

Eventually, no matter which model was "followed" by mother nature, a beam of ions remains from the sprayed solution which now has to be handled by the experimenter according to her needs. In a simple deposition setup the counter electrode may directly be the sample to be deposited on, in others the generated ion beam passes an atmospheric pressure interface of sorts and has to be axially contained further downstream.

2.4 Vacuum Ion Guidance Systems

Ever since ions and charged particles in general have been investigated in the gas phase one of the most prominent questions posed has been how to effectively and efficiently contain them. Answers to this question have taken many forms, depending on the special circumstances under which containment is desired, with electro- and magnetostatic systems having been among the earliest representatives [125–127]. The field was expanded considerably after Paul and Steinwedel introduced the electrodynamic quadrupole ion trap or mass filter in the 1950's [128, 129] which has since literally opened up its own era in analytical chemistry and from which several improvements and branchings have been derived over the past 60 years [130, 131]. Many more uses for such field-driven confinement systems have been found and investigated, particularly in particle accelerator and nuclear fusion research [132–134]. Out of necessity regarding the setup developed within the framework of this thesis however, the following sections will solely focus on radio frequency (RF) driven ion optics, but the inclined reader can find more on electrostatic and magnetic confinement in the literature [135, 136].

The basic working principle of a quadrupole mass filter stems from the interplay of RF and DC voltages applied to its rods (see figure 2.11). This causes ions traversing its length to oscillate and although stable trajectories exist which allow an ion to pass the device this is at any given set of parameters usually only the case for a very narrow

band of mass to charge ratios, hence the term "mass filter". This application of RF and DC voltages onto a set of electrodes is a general theme also for higher order multipoles and stacked ring ion guides and it's the fundamental reason for their ability to confine and focus ion beams (see sections 2.4.2 and 2.4.3). Whether these electrodes are then arranged parallel or perpendicular to the ion beam is, at first surprisingly so, of little consequence for the actual confining effect which will be discussed in more detail in the following sections.

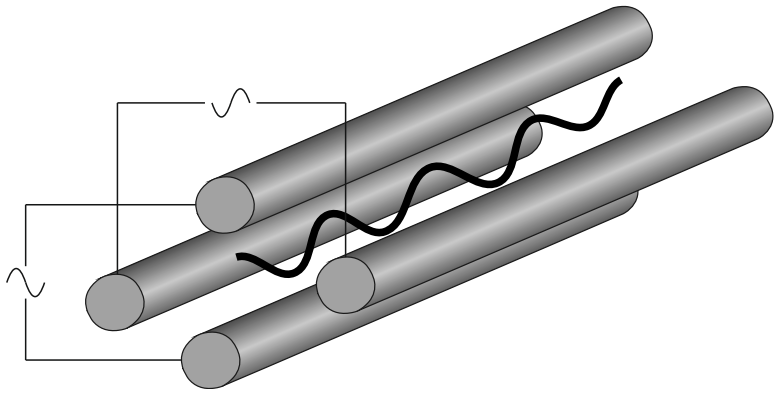

Figure 2.11: Schematic view of a stable ion trajectory inside a quadrupole mass filter. Two RF voltages of identical wavelength and amplitude are applied in such a manner that neighboring electrodes are phase shifted by π with respect to each other. Furthermore, a DC potential is applied between the two RF voltages.

2.4.1 Theory of RF-driven Ion Guides

Ion confinement in rapidly oscillating electrodynamic fields has one unifying physical source which is known as the ponderomotive force [137, 138]. A charged particle is alternating between attraction and repulsion to and from an ion guide's electrodes as the RF potential runs the course of its oscillation. During the attractive half-periods it will thus be closer to the electrodes than during the repulsive ones and this circumstance in conjunction with the inhomogeneity of the field, which is stronger at points closer to the electrodes, leads to a net force pointing away from them. This unifying feature is the boon for theoretical considerations regarding all RF-driven ion guides, because although for one special case, the quadrupole, solutions to the ion's equation of motion can be derived by solving the Mathieu equations [139], this seems not to be possible for higher order multipoles of any form. Solving the Mathieu equations for the quadrupole leads to two dimensionless parameters governing the stability of ion trajectories through such a device:

$$a_u = \pm \frac{8qV_{DC}}{mr_0^2\Omega^2} \tag{2.4}$$

$$q_u = \pm \frac{4qV_{RF}}{mr_0^2\Omega^2} \tag{2.5}$$

with elementary charge q, ion mass m, and inscribed radius r_0. One can see that these only depend on the RF voltage's angular frequency $\Omega = 2\pi f$ and its amplitude V_{RF} as well as the DC potential's magnitude V_{DC}. It is thus possible with a quadrupole mass filter to reach a so-called resonant mode by tuning these parameters, where ions of a certain mass to charge (m/z) ratio are transmitted through the device. Investigations into ion trajectories for higher order multipoles with more than two electrode pairs have yielded much more complicated correlations where sadly no analytical solutions exist [140–143]. In general, higher order multipoles are used for transmission of a broad band of m/z ratios instead of mass filtering. This works just as well without a DC potential, leaving only the RF-field's capability to restrain ions to be discussed.

In a comprehensive review Gerlich used the more general ponderomotive force ansatz to nonetheless derive some fundamental theoretical aspects of ion motion in RF-driven ion guides and the following deductions can be found in more detail there [144]. The classical, non-relativistic equation of motion for such a particle is:

$$m\ddot{r} = qE(r,t) + q\dot{r} \times B(r,t) \tag{2.6}$$

with particle position r, electric field E, and magnetic field B. Neglecting the magnetic field contribution is valid due to the ion's low velocities and hence low Lorentz forces, as compared to electrons. Another simplification can be made by using a superposition ansatz to split the electric field into a static part $E_s(r)$ and a time dependent part thus yielding:

$$m\ddot{r} = qE_0(r)\cos(\Omega t + \delta) + qE_s(r) \tag{2.7}$$

with the external field's amplitude E_0, and a phase-shift δ. To solve for the particle's position $r(t)$ one then considers a separation of the motion into a slow drift term $\mathrm{R}_0(t)$ and a rapidly oscillating one $\mathrm{R}_1(t)$:

$$r(t) = R_0(t) + R_1(t) = R_0(t) - a(t)\cos\Omega t \tag{2.8}$$

A time-independent amplitude a can be approximated from the corresponding oscillating motion in a homogeneous field and is then given as:

$$a = \frac{qE_0}{m\Omega^2} \tag{2.9}$$

The validity of this approximation as well as the separation ansatz used for (2.8) however depends on the nature of the interaction between ions and the RF field. If this interaction is adiabatic, that is, no energy is being transferred between the two, a will

indeed be constant over time and (2.9) valid. Also, in this case, oscillating motion and drift motion are truly decoupled from one another. This is a commonly used method called the adiabatic approximation [145] and it has been found to be valid for regions inside an ion guide which are not too close to the electrode surfaces where spatial variation of the electric field is smooth enough, such that during one oscillation period the field changes only insignificantly [144].

Following a short mathematical conversion using a Taylor expansion and some vector analysis one arrives at a differential equation for the non-oscillating drift motion $R_0(t)$:

$$m\ddot{R}_0 = -\frac{q^2}{4m\Omega^2}\nabla E_0^2 - q\nabla\Phi_s \tag{2.10}$$

with the electrostatic potential Φ_s. The first part of this result is precisely the aforementioned ponderomotive force, always pointing toward lower field regions and independent of the ion charge's sign, as it is squared. Also worth noting is its dependence on Ω^2. This decrease of force with increasing frequency can be nicely visualized, as the ion switches back and forth more rapidly and hence travels a shorter distance in the repulsive potential. One can write (2.10) in the form:

$$m\ddot{R}_0 = -\nabla V^*(R_0) \tag{2.11}$$

with the so-called pseudopotential:

$$V^*(R_0) = \frac{q^2}{4m\Omega^2}E_0^2 + q\Phi_s \tag{2.12}$$

This is a universal result for all RF-driven ion guides although the pseudopotential's actual shape will vary with the design as $E_0(R_0)$ depends on the geometry of the electrodes. Furthermore, due to the assumptions made, this result can no longer be applied to the quadrupole's mass filtering capabilities. Also, the spatial limits of the adiabatic approximation's validity will change as the so-called adiabaticity parameter:

$$\eta = \frac{2q}{m\Omega^2}\cdot|\nabla E_0| \tag{2.13}$$

which should always be considerably smaller than unity also depends on $E_0(R_0)$ and thus electrode geometry.

2.4.2 Multipole Ion Guides

As has been mentioned above the quadrupole mass filter has lead to many design branchings over the years as experimenters were looking for solutions to ever more specialized problems, some of which require completely disparate developments. A commercial

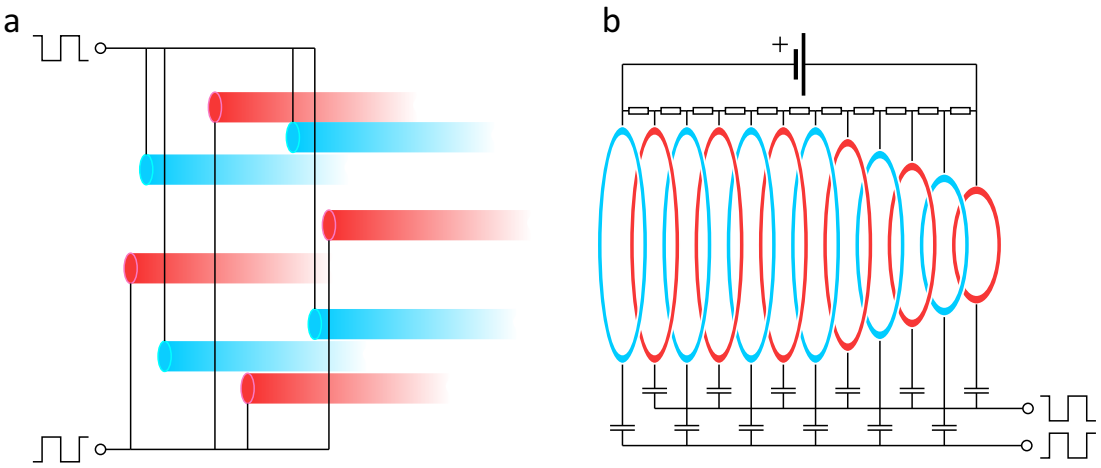

Figure 2.12: Schematic drawings of two types of RF-driven ion guides used and developed in this thesis. **a** - A multipole consisting of eight electrodes arranged parallel to the beam, hence a so-called octopole. **b** - An ion funnel with ring-electrodes stacked perpendicular to the beam direction. Explained in more detail in section 2.4.3.

quadrupole for example is usually built from steel or Mo rods of circular cross section although an ideal quadrupole field would require a hyperbolic cross section. As this deviation from the ideal case has an adverse influence on the filtering solution attempts have been made to approximate a hyperbolic electrode by using an array of thin wires [146, 147]. On the other hand, high mass resolution may not be desired if one is looking for a conducting ion guide where high transmission of a range of different masses is asked for. This express purpose is being fulfilled by multipole ion guides [148–150] which feature a number of electrode pairs $N > 2$ (see figure 2.12).

The pseudopotential without its electrostatic part in such a geometry takes the form [151]:

$$V^* = N^2 \frac{q^2}{4m\Omega^2} \frac{V_{RF}^2}{r_0^2} \left(\frac{r}{r_0}\right)^{(2N-2)} \tag{2.14}$$

One can easily deduce the significant influence of the number of electrode pairs on the pseudopotential's shape from this. The more electrodes are being used the steeper the potential will be in their vicinity and correspondingly flatter in the middle of the device. This in turn plays an important role in the transmission capabilities of such devices as more charge will fit into the inscribed diameter and steeper repulsive potential with higher N, although this effect will be discussed in more detail in section 4.4.1. There, we will also see that, although it is not apparent from the formulas derived here, a resonance condition depending on m/z of the transmitted ions also exists for higher order multipole ion guides.

Another property rising proportional to N is a multipole's ability to shield its inscribed volume against influences from externally applied fields, because at constant

inscribed radius r_0 the space between electrodes reduces with N (see figure 2.13). This correlation is experimentally of importance if badly conducting surfaces in the vicinity of a multipole are charging up during an experiment. See section 4.4.3.

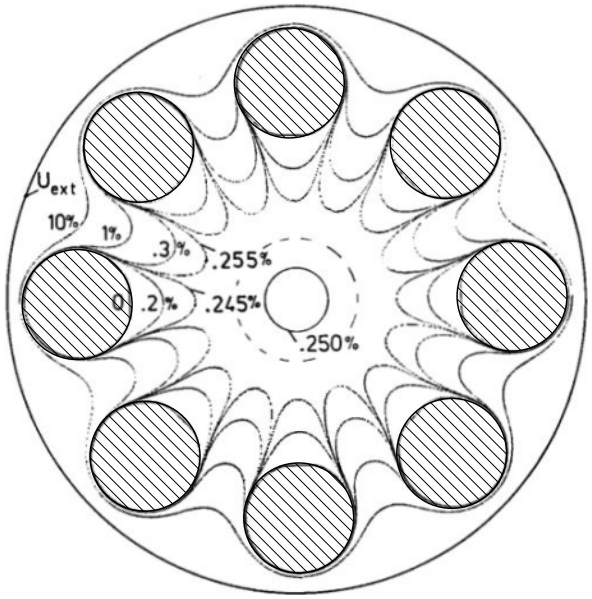

Figure 2.13: Contour plot of field penetration in an octopole with a potential U_{ext} applied on the outside of the octopole with the rods' potentials set to zero. Rod cross sections are hatched. The percentage values are given relative to the external potential. From [144] with modifications.

2.4.3 Ion funnel

Although multipoles have certainly improved greatly upon the quadrupole's transmission capabilities, their use for this purpose is limited to a certain set of circumstances. They tend to work poorly in pressures above 10^{-2} mbar and although they have been used as collisional focusing devices and in buffer gas cooling experiments, their ability to focus an ion beam's diameter down to smaller sizes is severely limited [130, 152, 153]. There is also no straightforward way to focusing simply by geometric adjustments to the electrode array, e.g. by arranging them in such a way that the inscribed cylinder is tapered towards one end. This would inadvertently lead to a gradual change of resonance or stability parameters over the length of the device and ions of all mass to charge ratios would be confined poorly at some point or another, thus leading to significant losses. However, a device which perfectly compensates the multipole's drawbacks does exist: the ion funnel. In contrast to the axially parallel alignment of a multipole the electrodes in an ion funnel are stacked perpendicular to the ion beam (fig. 2.12), a method of confinement which had been predicted to be possible by Gerlich and has

been under constant development predominantly by Smith an coworkers since the 1990s [144, 154–157]. This now renders focusing of ions possible by sequentially reducing electrode diameters towards the rear end of the device. However, some considerations have to be taken into account when doing this.

The pseudopotential in such a configuration can be written as [158]:

$$V^*(r,z) = \frac{V_{max}}{I_0^2(r_0/\delta)}\left[I_1^2(r/\delta)\cos^2(z/\delta) + I_0^2(r/\delta)\sin^2(z/\delta)\right] \tag{2.15}$$

with the maximum effective potential at r_0:

$$V_{max} = \frac{qV_{RF}^2}{4m\Omega^2\delta} \tag{2.16}$$

which depends on the spacing between electrodes d via a characteristic length $\delta = \frac{d}{\pi}$. I_0 and I_1 are zeroth and first order first kind modified Bessel functions which, for arguments $x \gg 1$, can both be approximated to be $I_n(x) \approx \exp(x)/\sqrt{2\pi x}$. Again, after a short mathematical conversion this allows for a more intuitive look at the pseudopotential:

$$V^*(r) \approx V_{max}\frac{r_0}{r}\exp\left(\frac{r-r_0}{\delta/2}\right) \tag{2.17}$$

This highlights a fundamental correlation between electrode spacing and pseudopotential reach, namely that if δ is halved so is the reach of V^*, because similar potential values will be obtained if the exponent stays constant, which will be the case for proportionally smaller distances from the electrodes $r - r_0$. Thus, especially in the case of space charge limited transmission, higher charge capacities can be reached by decreasing the electrode spacing.

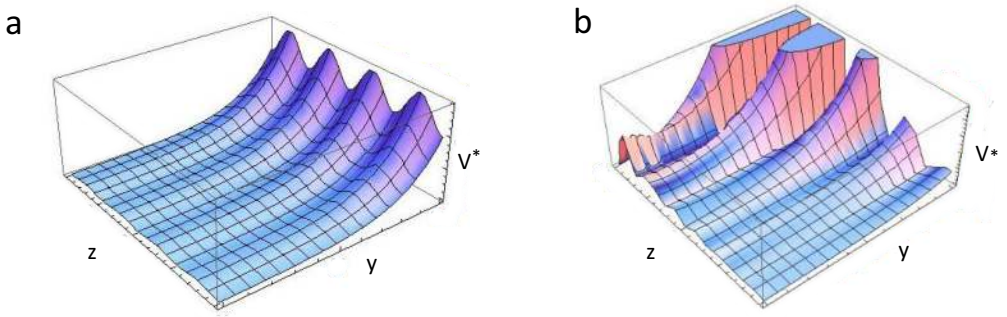

Figure 2.14: Potential landscape in an ion funnel at a height x cutting through the center of the device. *a* - Potential produced by rings with equal inner diameter. *b* - Potential arising from rings with inner diameter decreasing in z-direction. From [159].

Over the course of the last mathematical conversion the pseudopotential's dependency on z was lost, but this can again be derived for areas close to the central axis from 2.15 by assuming $r = 0$, because $I_0(0) = 1$, while $I_1(0) = 0$:

$$V^*(0,r) = V_{trap}\sin^2\left(\frac{z}{\delta}\right) \tag{2.18}$$

Here V_{trap} is the so-called trapping potential, which equals the fractional prefactor in 2.15 and can be approximated to be:

$$V_{trap} \approx V_{max} \frac{2\pi r_0}{\delta} \exp\left(\frac{2r_0}{\delta}\right) \tag{2.19}$$

This dependence is of utmost importance at the focusing stage of an ion funnel where the electrodes' inner diameters are constantly decreased, which in turn leads to an exponentially proportional increase in trapping potential barriers along z, which have to be overcome by the ions, thus leading to significant losses at this stage (see figure 2.14).

Usually, a pulling DC potential is applied to an ion funnel in order to mitigate this effect, which has so far been neglected in all equations for the pseudopotential, but as can be seen from figure 2.14b at the very narrow stages towards the funnel's rear end this effect is so pronounced that it may lead to losses either way, because of the effect's inherent exponential behavior, which a linear DC potential will eventually be unable to overcome. Similar to the pseudopotential penetration range, however, the trapping potential is likewise exponentially dependent on the electrode spacing. Stacking the electrodes more closely towards the funnel's focusing end should thus be a viable option, an approach which has been used in constructing an ion funnel within the present work, see section 4.4.2. On the other hand, Julian et al. have taken the counterintuitive approach of using large electrode spacing with the argument that in this configuration the ions are already confined more closely to the axis due to the farther reaching potential and can thus be more easily focused into a small aperture [160]. The downside of this approach is of course reduced charge carrying capacity in the space charge limited regime.

2.4.4 Ion Trajectory Simulations

Calculating the trajectories and overall behavior of ions traveling through RF-driven ion guides is, as has been mentioned in the previous sections, at best challenging and at worst impossible due to the complexity inherent in higher order multipole fields. And this is already the case for just one particle; once an ensemble of ions is investigated the Coulomb interaction between them leads to a classical many-body problem, thus not only completely prohibiting an analytical solution but also greatly increasing the expense and computing time of numerical approximations. Such approaches have been of considerable interest in physics for almost a hundred years now and especially in plasma physics the so-called particle-in-cell method has been an early representative capable of

tackling many-body charged particle problems via a fluid dynamic, mixed Lagrangian-Eulerian frame ansatz [161–163]. Simulations of ion trajectories in RF-driven guides can be conducted with a somewhat simpler model by eliminating the Lagrangian fluid frame. For this purpose the commercially available software package SIMION 8.1 was utilized in this thesis, which has its roots in an electrostatic optics program developed in the 1970's and has been greatly improved by Dahl and Manura since the 1990's [164–166]. It has been used to solve a multitude of charged particle problems including electron trajectories in different settings [167, 168], ion motion in quadrupoles and other ion guides [158, 169], mobility spectrometers [170], and ion trajectories at atmospheric pressure [171], among others.

At its core SIMION calculates electric and magnetic fields at discrete mesh points utilizing finite different methods and a Runge-Kutta solver for solving differential equations, most importantly the Laplace equation [166]. From these fields and the ions' positions in them forces acting on the ions are then calculated, which in turn lead to their trajectories (again via an adaptive step size Runge-Kutta solver). This process is repeated over several time steps until a certain termination condition is met. A very powerful feature is the ability to run custom-coded segments (written in Lua) at specific points during this iterative process, which allows the user to e.g. influence electrode potentials or have the ions scatter with neutral background gas atoms or molecules (see figure 2.15).

Space charge or Coulomb repulsion between ions can be taken into account using a built-in factor repulsion approach where simulated ions are point charges actually consisting of bunches of ions (a super-particle approximation) and each point charge's effective charge is the product of a single ion's charge times a given multiplication factor (which we will call *repulsion factor* from here on) [172]. One super-ion thus generated typically emulates around 5000 real ions and in turn simulations contain anywhere between 10^3 and 10^4 super-ions enabling simulation of ensembles of up to $10^{10}\,\mathrm{cm}^{-3}$ ions, a reasonable number compared to laboratory ion beam densities [162]. This approximation however is only used in calculating the Coulomb repulsion between the ions, which scales with (repulsion factor)^2. Interaction with the electrodes' potential and scattering with neutral background gas are calculated for individual ions, not super-ions. Thus, for different calculations with constant total charge but different repulsion factors both kinetic and potential energy of the system scale with the number of simulated ions, but the Coulomb energy more or less stays constant [173].

Apart from physical electrode geometries, which can be defined by the user via several different methods, implementation of static pseudopotentials is also possible. Whatever the nature of the potential's source, ions are generally initialized at random

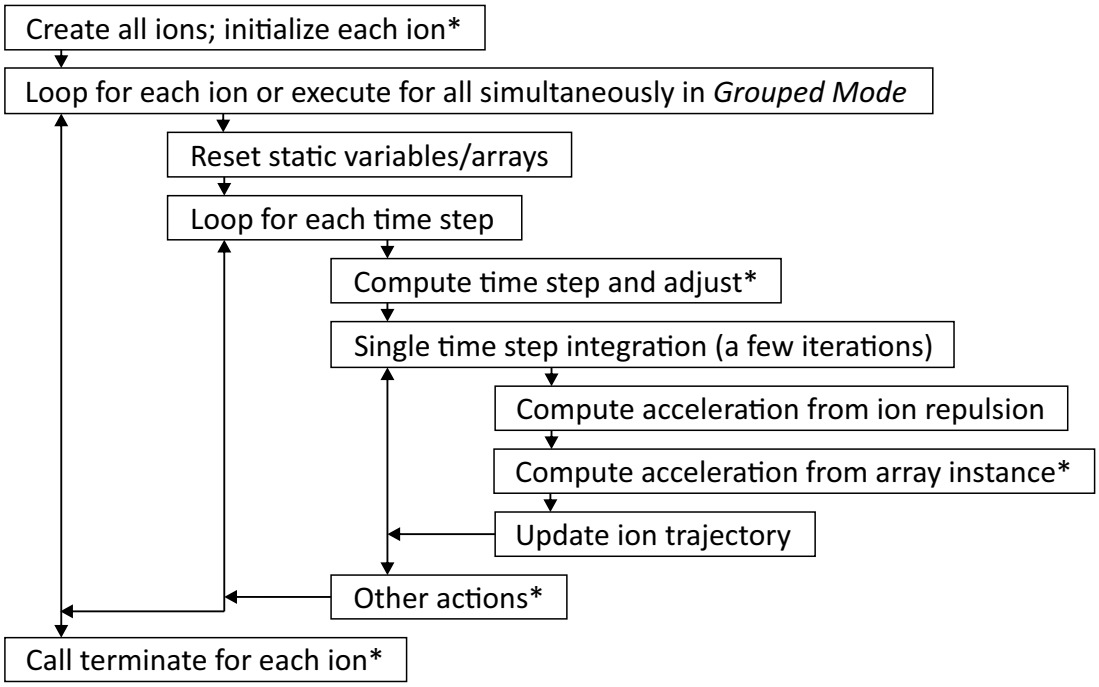

Figure 2.15: Flow diagram of SIMION's iterative ion trajectory simulation procedure. Entries marked with an asterisk allow for integration of user-made procedures. From [166] with modifications.

starting points. However, random initial distributions are known from particle-in-cell simulations to cause artificial over-excitation of the system resulting in high noise or even completely divergent behavior and simulation blow-up due to high energy regions where ions are placed too close to each other [161]. Several so-called "quiet start" methods have been developed to increase signal-to-noise ratio in such simulations by correcting initial moments or distributions [174]. In this thesis a "soft start" approach is used, where over the course of an adjustable initial alignment phase the ion charge q is logarithmically expanded from 1 to 100 %, thus slowly "turning on" space charge and allowing the ions to gradually relax into a more stable distribution, thereby greatly reducing the risk of simulation blow-up.

See appendix A.2 for more detailed information on chosen simulation parameters and models.

2.4.5 RF Power Supplies

One of the most fundamental technical requirements in the application of RF-driven ion guides is, of course, the prior generation of a suitable RF potential. Ever since the invention of the Paul trap sinusoidal signals have been the most commonly used form of potential due to the relatively low complexity of generation via simple oscillating

circuits [131]. These circuits are driven resonantly to the electrodes and have a fixed frequency. Mass selection is facilitated by sweeping RF and DC amplitudes such that the ratio V_{DC}/V_{RF} stays constant. Figure 2.16 shows the circuit diagram of one such sinusoidal power supply. Over the years, however, many groups have found that the waveform of said RF potential can take almost any form without compromising stability of ion trajectories, although there is certainly an influence on the boundaries of stable regions [175]. Square waves have been among the first "deviators" from the well-trodden path of sinusoidal potentials [176–178], but other forms are possible [179] and in general a theoretical treatment of stability has been conducted by studying solutions to the Hill equation, of which the aforementioned Mathieu equation is a subset for the case of sine waves [180]. Using square or other waves of course necessitates different forms of signal generation, which, in contrast to analog oscillating circuits, are commonly digital in nature. This has led to the development of the so-called digital ion trap, for example [181]. Two major advantages of these systems are their ability to abruptly start and stop signal creation as well as an inherent capability to easily sweep across a more or less wide band of frequencies, which distinctly sets them apart from their analog counterparts and allows for a completely different mode of operation [182, 183]. In exchange, however, there are some complications to keep in mind considering signal transduction in the cable due to its inherent dispersion, and the ion guides capacitance, which may lead to resonant behavior all along (see section 4.4).

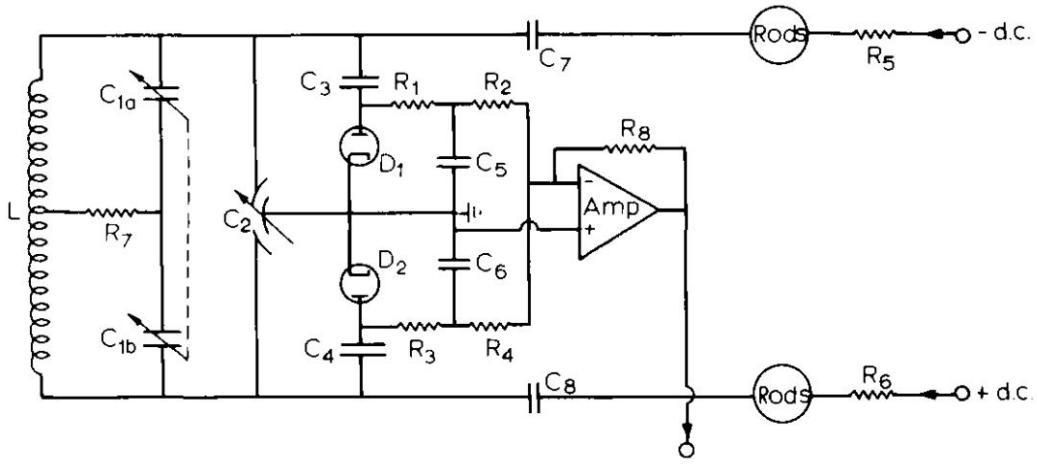

Figure 2.16: Circuit diagram of a simple multipole power supply operating in resonant mode with the electrodes (here *rods*). Capacitors C1 and C2 can be adjusted in order to reach resonance with rod setups of slightly different capacities. The RF voltage can be measured via two rectifying diodes connected to an operational amplifier. From [131].

3

STM: Case Studies of a Predicament

The importance of Scanning Probe Microscopy studies of organic molecules adsorbed onto pristine surfaces has been discussed exhaustively within the previous two chapters. Here, we will focus on two case studies of different molecules and their behavior when adsorbed on single crystal noble metal samples. Both have one preparative step in common, which is the use of an OMBE source for deposition of the different species. For the sake of a proper introduction and overall completeness, several noteworthy results regarding these two examples will be discussed, but they will be summarized in their respective sections rather than the thesis conclusion as they do not directly contribute to the main focus of this work. However, special emphasis will be put on such phenomena or experimental shortcomings directly related to the OMBE preparation technique, all of which will be discussed in the last section, including a few more systems, which have been the focus of prior works. Characteristic preparation parameters, if not mentioned within this chapter, can be found in appendix A.1. Scanning parameters of individual images will be mentioned in the corresponding figure captions in parentheses. All images were obtained in constant current mode unless noted otherwise.

3.1 Rare Earth Sandwich Complexes

Ever since the advent of single molecule magnets in the 1990's [184, 185] this class of materials has been under intense investigation as a possible candidate for future use in quantum computers, spintronics, and high density information storage [17, 186–188]. One specific subgroup, rare earth complexes with phthalocyanine-based ligands, have more recently risen to fame and attracted special interest due to their high single-ion

anisotropy [189–196], a comprehensive review on lanthanide single molecule magnets was given by Woodruff et al. [197].

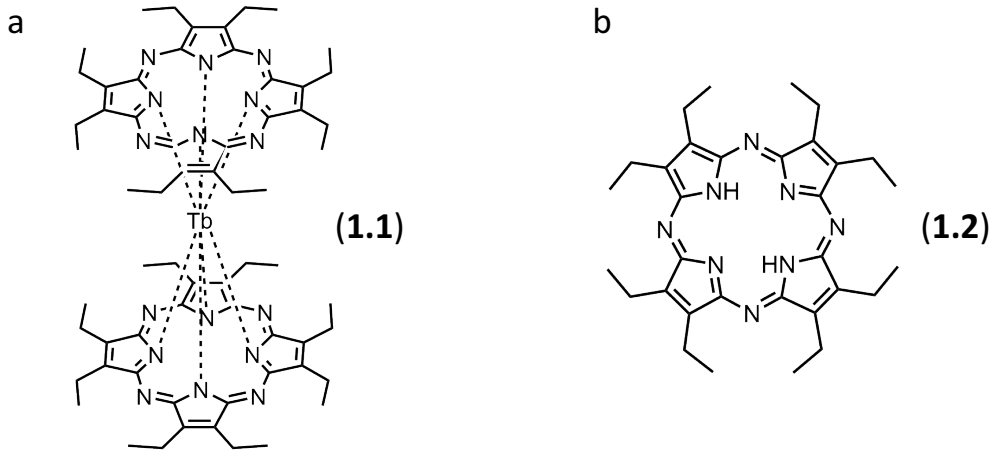

Figure 3.1: Chemical formulas of **a** - bis(2,3,7,8,12,13,17,18-octaethyl-5,10,15,20-tetraaza-porphyrinato)terbium (**1.1**), henceforth called $Tb(OETAP)_2$, and **b** - the single ligand OETAP (**1.2**).

During the course of this thesis one recently synthesized double-decker complex of this subgroup [198] consisting of a central Tb atom chelated by two ethyl-substituted porphyrazine macrocycles and thus forming a square antiprism geometry, from here on designated as $Tb(OETAP)_2$ (see figure 3.1a), was investigated using STM and XPS. Single molecular magnetism of this compound in solution has already been reported [198]. After deposition on Ag(111) at low surface coverages single molecules of this species adsorb flat-on and mostly decorate the crystal's step edges, although some can be found adsorbed on terraces. The decoration of step edges already hints at the molecule's ability to diffuse around the surface. They exhibit a characteristic four-fold, multi-lobed structure when probed at positive bias voltages (see figure 3.2a) which splits up into an eight-fold structure at negative bias (not shown). We attribute these lobes to the eight ethyl moieties of one ligand. Since the upper ligand is not attached to the surface and the central lanthanide atom allows for a certain degree of freedom, sandwich complexes can exhibit the ability to rotate even after adsorption [199, 200]. A straightforward way to check for intact molecules is hence given by scanning over a single molecule with relatively high current, thus increasing the interaction between tip and molecule, until said interaction leads to rotation or switching of the top ligand's orientation. This can be observed in sub-panels a through c of figure 3.2, which show a series of three images taken consecutively with the second one at an increased current. Due to the actual switching process being much faster than the STM's scanning speed it can not be resolved and is instead observed as a discontinuity from one line scan to

the next (marked by a thin white line in figure 3.2b). The same effect can be achieved by a so-called lateral manipulation experiment, wherein the tip is used as a somewhat sophisticated stick to push or pull adsorbates around. This is driven by either attractive or repelling tip-adsorbate interactions and experimentally realized by lateral movement of the tip above the sample at a fixed bias voltage.

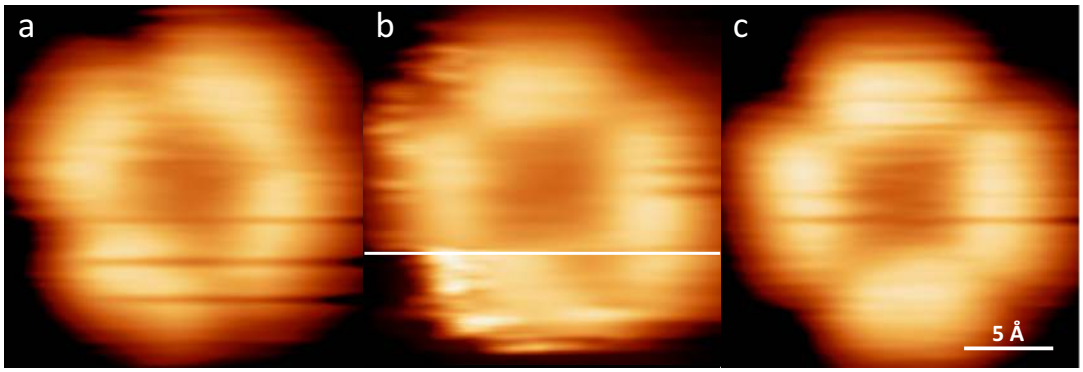

Figure 3.2: Rotation of the upper ligand of a single $Tb(OETAP)_2$ molecule adsorbed on Ag(111) due to interaction with the STM tip (a,c: +1.1 V, 8e-11 A; b: +1.1 V, 2e-10 A).

3.1.1 Self-assembly on Noble Metal Surfaces

Dosing higher amounts of OETAP double-decker molecules onto pristine noble metal surfaces leads to supramolecular structures formed by attractive van der Waals interactions between diffusing complexes. Figure 3.3 shows this self-assembling behavior. Assemblies on Ag(111) and Cu(111) were investigated for $Tb(OETAP)_2$ within the framework of this thesis while its closely related dysprosium counterpart, namely $Dy(OETAP)_2$, was the subject of interest in a collaborative work soon to be published [201] and is mentioned here because of its very similar behavior. Both lanthanide double-decker molecules exhibit the characteristic four-fold, multi-lobed shape at positive bias voltages, which was mentioned before (cf. black outline in figure 3.3b) which splits into eight lobes when measuring at negative bias (cf. figure 3.3f). However, at certain bias voltages one can observe an intriguing difference in apparent height between assembled molecules, which can be seen clearly in 3.3a. A few very bright spots can be attributed to second layer molecules (around 1-2 % in most preparations), especially since these molecules can be moved around on an island simply by scanning over them, but the difference in contrast of the surrounding assembly ($\sim 2\,$Å) does not correspond to an additional layer of either double-deckers ($\sim 3\,$Å) or single OETAP molecules ($\sim 1.5\,$Å, all apparent height measured at +1.2 V). In a first attempt to get to the bottom of this phenomenon a series of lateral manipulation experiments was conducted at an island

edge in order to take the assembly apart step by step. This only ever yielded intact $Tb(OETAP)_2$ molecules. Moreover, the appearance of this pattern strongly depends on applied bias and "bright" species can be irreversibly switched into "dark" ones through strong tip-sample interactions. Both effects will be discussed in more detail in the following subsection.

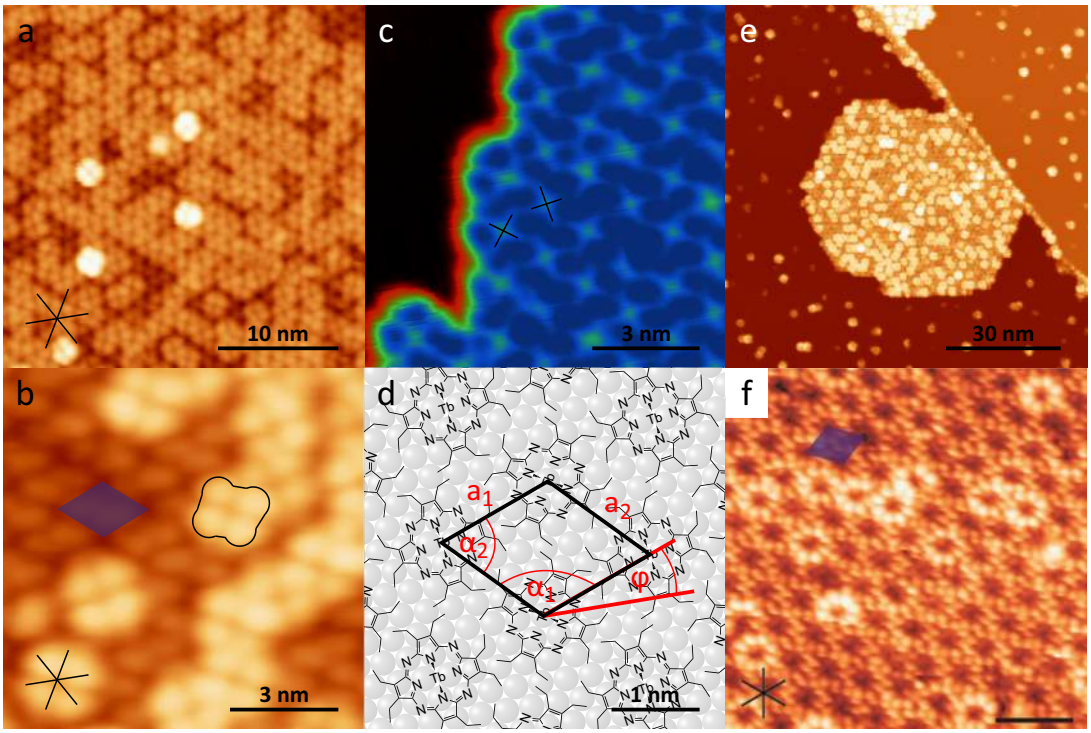

Figure 3.3: Self-assembling behavior of $Tb(OETAP)_2$ on Ag (111) (a-d) and Cu(111) (e) as well as $Dy(OETAP)_2$ on Au(111) (f). Dense-packed crystal directions are indicated by sixfold stars. **a** - Overview image (+1.2 V, 8e-11 A). **b** - High resolution close-up image (+1.0 V, 1e-10 A). **c** - False color high resolution image highlighting the orientations of single molecules (+1.5 V, 1e-10 A). **d** - Tentative model of the assembly and its characteristic dimensions. **e** - Overview image (+0.65 V, 1e-10 A). **f** - Overview image from [201], scale bar = 3 nm (-2.3 V, 6e-11 A).

$Tb(OETAP)_2$ forms extended and very well ordered islands on Ag(111) (figure 3.3a-d) with a rhombic unit cell with measured unit cell vectors of $a_1 = 14.1 \pm 0.4$ Å and $a_2 = 14.2 \pm 0.4$ Å, included angles $\alpha_1 = 114 \pm 5°$ and $\alpha_2 = 66 \pm 5°$, and an angle $\phi = 20 \pm 5°$ between a_1 and the closest dense-packed crystal direction. Overlaying a tentative model obtained with the methods described in section 2.1.4 onto a model of the Ag(111) crystal one can see that within the limits of the STM's calibration a quasi-commensurate overlayer is possible with exact unit cell parameters of $a_1 = 13.9$ Å, $a_2 = 14.2$ Å, $\alpha_1 = 114.2°$, $\alpha_2 = 60.5°$, $\phi = 20.5°$. Relative to the underlying crystal lattice this assembly can thus be designated as a $(\sqrt{93}\text{x}\sqrt{97})\text{R}20.5°$ superstructure [202].

In such an overlayer only every other molecule is adsorbed on a similar adsorption site, as can be seen in figure 3.3d. Bear in mind however, that the nature of the adsorption sites shown in this model (top and bridge, respectively) is pure speculation as this information can not be obtained from measuring characteristic dimensions alone. To this end an additional adsorption site determination experiment would have to be conducted, because although STM does allow for atomic resolution it is usually not possible to image molecules and the underlying crystal lattice at the same time [74, 203]. A quasi-commensurate overlayer will, however, be given in any case, no matter the actual adsorption sites. This is corroborated by the fact that, at certain bias voltages, the macrocycle backbones of single molecules within the assembly can be observed which express a sub-pattern of alternating vertical rows of similarly aligned molecules. Figure 3.3c shows such an image at high contrast and false coloration to better make out the cross-shaped backbones (two differently aligned molecules are marked with X's). Measuring the angle of orientation with respect to the crystal lattice is rather imprecise due to the small dimensions of the backbones, but a tentative guess has nevertheless been incorporated into figure 3.3d. It shows that similarly aligned molecules are likewise adsorbed on similar adsorption sites, which is a good indicator as to the validity of this model.

$Tb(OETAP)_2$ on Cu(111) as well as $Dy(OETAP)_2$ on Au(111) and Cu(111), and single OETAP molecules on Au(111) behave very similar to the self-assembly just described. The first case is shown in figure 3.3e and although either the attractive interaction between molecules and copper surface or the diffusion barrier is stronger to the point where markedly more single molecules can be observed on the free terraces there are still extensive and neatly ordered islands being formed. The unit cell dimensions here are a little extended in comparison, with: $a_1 = 14.2 \pm 0.5$ Å, $a_2 = 14.8 \pm 0.5$ Å, $\alpha_1 = 115 \pm 5°$, and $\alpha_2 = 65 \pm 5°$. No lattice directions were determined during this experiment, making even a tentative model impossible. A significant portion of the individual molecules, however, have been found to be single OETAP fragments, a fact which will be the main focus of subsection 3.3.1. Furthermore, the assemblies exhibit the exact same random contrast pattern mentioned before, which indicates that this phenomenon does not arise due to interaction with the surface. The same is apparently true for assemblies of $Dy(OETAP)_2$ shown in figure 3.3f. Although this image has been taken at negative bias where the molecules display their eight-fold HOMO state one can still make out differences in contrast, albeit more gradual than in the other cases. Lattice vectors here are again similar to the ones mentioned above and the same alternating alignment from one row to the next can be observed. The same goes for assemblies of single OETAP molecules (not shown here) [201]. Overall, this is a strong indicator for molecule-surface

interactions being rather weak compared to molecule-molecule interactions as obviously the choice of surface does not greatly influence the assembly characteristics. However, the formation of quasi-commensurate as opposed to perfectly commensurate assemblies does mitigate this indication somewhat. Usually, a markedly different behavior can be observed when comparing molecules on noble metal surfaces as surface reactivity is, for many systems, weakest for Au(111), stronger for Ag(111), and strongest for Cu(111) [204, 205].

3.1.2 Contrast through Orientation?

The phenomenon of bias voltage dependent molecular contrast in $Tb(OETAP)_2$ islands, which has been mentioned before, can be seen in more detail in figure 3.4. Sub-panels a to c show an overview of one island at +1.2, +1.4, and +1.6 V, respectively. With rising bias voltage one can clearly see a gradually more and more homogeneous appearance of the first layer until almost all of them appear to be of similar brightness at a certain threshold voltage, while the very few second layer molecules seem to remain unchanged. Towards lower positive biases below +1.2 V (not shown) even more molecules appear darker, that is to say at a lower apparent height, while some will stay bright down to very low bias values above the Fermi level. Also, the change is not sudden, but rather very gradual in a two-fold way: not all molecules exhibit the onset at the same voltage and when they do, contrast increases over a range of a few hundred mV for each individual molecule. There is thus at any given positive voltage below this "saturation" a wide range of apparent heights observable. Saturation voltages range from +1.6 to 2.0 V, probably depending on the tip state, although more statistics would have to be acquired in order to reliably gauge this influence. At negative biases assemblies appear non-uniform as well, but no such saturating behavior could be observed during our experiments in this regime. Very interestingly, sufficiently strong tip-sample interactions can change this individual contrast and irreversibly so.

Figures 3.4d-i show a series of images obtained during so-called vertical manipulation (VM) experiments. This procedure implies equilibrating the tip at a fixed position and distance (controlled via the tunneling current) above the sample surface and opening the PI-feedback loop. Afterwards, bias or distance may be sweeped in order to obtain characteristic I(V) and dI/dV(V) spectra; this process is generally known as scanning tunneling spectroscopy (STS). Sometimes, it is also worthwhile to sweep both parameters at the same time or keep both constant in order to induce some desired effect through tip-sample interactions. In this particular case at first a reference image was obtained after which the bias voltage was sweeped from -1.0 to 2.0 V at a position

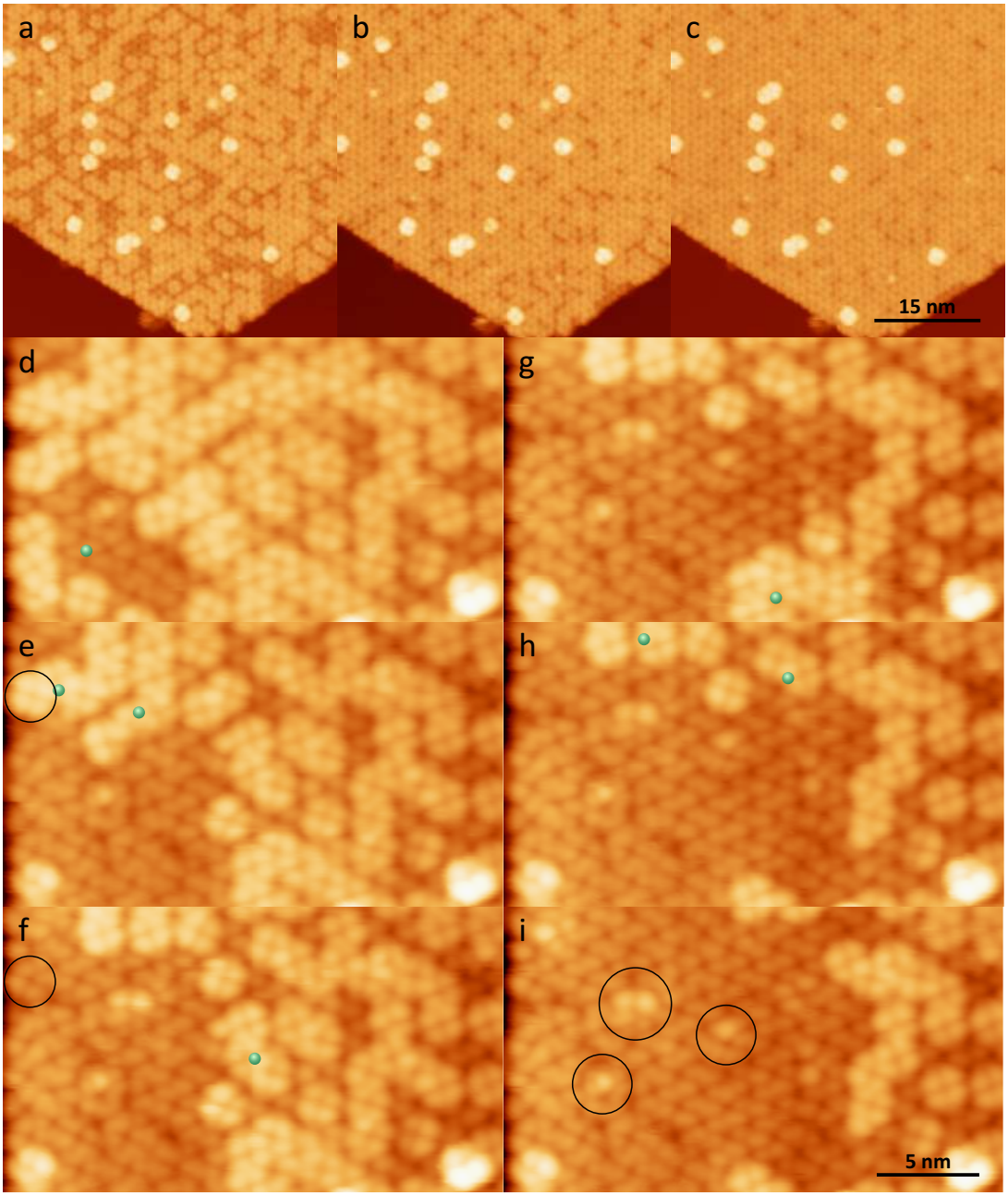

Figure 3.4: Molecular contrast in an assembly of $Tb(OETAP)_2$ on Ag(111) depending on bias voltage and tip-sample interactions. $a-c$ - Bias dependence showing more and more uniform contrast at higher bias voltages (a: +1.2 V, b: +1.4 V, c: +1.6 V; all: 8e-11 A). $d-i$ - Consecutive series of vertical manipulation experiments with tip positions indicated by green marks. Some images were obtained after two manipulations (all: +1.2 V, 1e-10 A).

indicated by the green spots. After the spectra were obtained another image was taken for comparison with the first. Sometimes, two vertical manipulations were conducted before the second image was taken (sub-panels e and h). One can clearly observe an irreversible and consistently reproducible switching of bright molecules to dark ones over an area of some nm^2, indicating either structural or electronic changes in individual molecules of the assembly. Another possible explanation would be that these molecules were simply picked up by the tip, but this usually results in rapid deterioration of the tip and hence image quality, which can not be observed here.

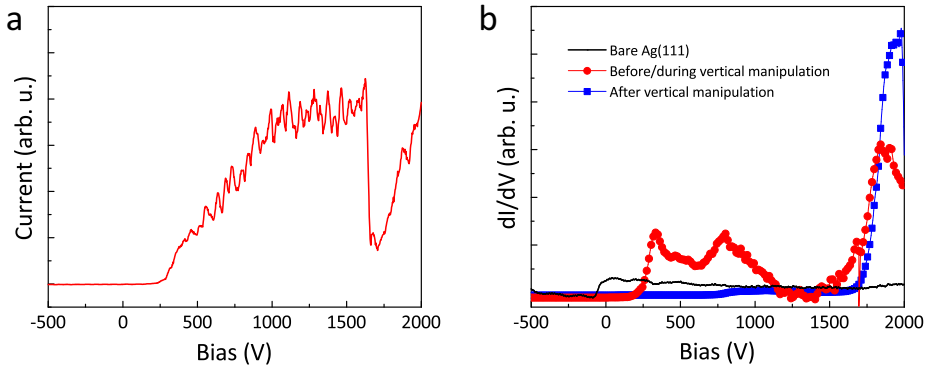

Figure 3.5: Selection of I(V) and dI/dV(V) curves obtained during the vertical manipulation experiments shown in figure 3.4d-i. **a** - I(V) spectrum obtained during vertical manipulation above a bright molecule. **b** - dI/dV(V) spectra obtained on bare Ag(111) (black line, no markers), during vertical manipulation above a bright molecule (red line, circular markers, corresponds to I(V) in sub-panel a), and afterwards on the now dark molecule (blue line, square markers). Voltages ramped from -1.0 to +2.0 V over a course of 30 s and 1056 steps, initial tunneling current 1e-10 A.

Apart from the obvious changes inflicted by this treatment, it is certainly interesting to investigate the obtained spectra, a selection of which is shown in figure 3.5. Sub-panel a shows a raw I(V) curve directly obtained during a VM procedure with the tip positioned above a bright molecule. A characteristic discontinuity can be seen around +1.7 V, which we associate with the actual switching process as it only appears if and when molecules change contrast and its position is more or less constant. dI/dV(V) spectra, such as those shown in sub-panel b, tend to be of more interest due to their direct relation to the sample's local density of states via eqn. (2.2). First, a spectrum is obtained above the pristine Ag(111) surface showing the characteristic surface state, which acts as a good indication that the tip is suitable for obtaining spectra, a condition usually referred to as a spectroscopic tip. This is also repeatedly done in between VM experiments and images to ward against sudden tip changes influencing the data. If this happens, a mild tip forming is usually sufficient to once again reach spectroscopic capabilities. dI/dV(V) spectra obtained above a bright molecule exhibit

a strong peak at approx. +1.8 V with two further peaks below +1 V, the latter two being completely absent when measuring over a dark molecule. A strong influence of this change in apparent height on the molecule's electronic state or vice versa is thus obviously given, although as to the nature of this change no conclusive evidence can be extracted from such spectra alone. It is worth noting, however, that this irreversible switching phenomenon can just as well be achieved by repeatedly scanning over an assembly at voltages above +1.7 V or by vertical manipulation with a constant voltage pulse above said threshold.

The question now arises, whether this observed switching is entirely electronic in nature or not. A change in the molecular backbone's orientation is, in any case, very hard to detect, even when a molecule directly at an island edge with more degrees of freedom is affected (see outlines in figures 3.4e and f). Nevertheless, a slight misalignment of one backbone with respect to the alternating pattern mentioned above, which is relaxed into the energetically more favorable position by tip-sample interactions, could still be possible. In many cases, however, even after switching a small residual bright part at the fringe of some molecules could be observed (outlines in figure 3.4i). This suggests an, at least partial, involvement of the ethyl moieties which, from a sterical point of view, would have enough degrees of freedom to account for such a restructuring effect. An attempt was made to find a relation between the number of bright species and sample temperature during deposition by cooling the sample with liquid nitrogen during the preparation or annealing the sample towards higher temperatures. The second method indeed leads to islands consisting of almost uniformly dark molecules with the same characteristic, low amount of second layer growth. A measurably larger number of bright molecules at low preparation temperatures would have allowed calculation of the activation energy of this switching process, but the data proved inconclusive due to too much contamination on the sample, which is common when preparing at very low temperatures.

In this case, a comprehensive conclusion can not be drawn from STM and STS data alone, if only because a large part of the molecule and especially its interaction with the substrate are experimentally simply not accessible. In order to shine some more light onto this effect, XPS measurements were conducted by Mateusz Paszkiewicz to gain information about chemical and electronic properties of the adsorbate (see figure 3.6). One should keep in mind that contrary to STM, however, XPS is a technique which inherently averages over a considerable surface area of an investigated sample, thus some results may be hard to reconcile at first. Any way, Lanthanide sandwich complexes are known to be able to switch between two different charge states of the central metal atom [206], an explanation which could account for this switching phenomenon. This may

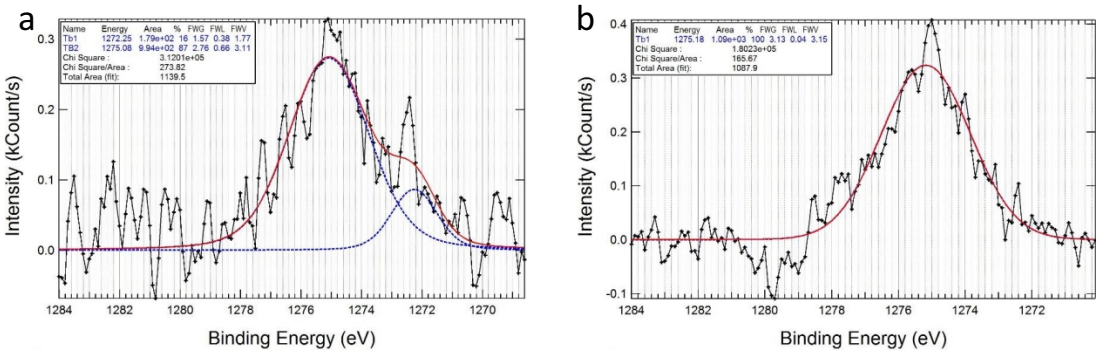

Figure 3.6: Tb 3d3/2 region of XP spectra of a monolayer of $Tb(OETAP)_2$ on Ag(111). **a** - After deposition onto a cold sample (-184°C). **b** - After annealing to 200°C.

be the case even though a gradual change in apparent height is observed, as molecules adsorbed on surfaces can very easily be partially charged [207], although the irreversibility of the process does not quite fit into this picture alone. XPS measurements were conducted with both room temperature and cold preparations, but no differences in the $Tb3d_{3/2}$ peak could be observed. However, the obtained peak intensity was rather low, thus a conclusive negative result can not be drawn from this observation. Furthermore, samples of different coverages were prepared in order to check for the metal surface's influence on the electronic state of either ligand or central atom, but again no differences could be observed. All in all, further studies have to be conducted in order to reach solid conclusions as to the origin of this puzzling phenomenon.

3.1.3 Summary

In this section, the combined STM and XPS study of a sandwich complex consisting of a terbium central atom and two peripherally ethyl-functionalized porphyrazines, called $Tb(OETAP)_2$, was discussed. These molecules, which are potential candidates for applications as single molecule magnets, are apart from being soluble also capable of being sublimed and deposited onto a sample surface where they adsorb in a flat-on fashion and self-assemble into regular, dense-packed islands even at low coverage. These assemblies show a remarkable independence of the substrate material used, with islands of $Tb(OETAP)_2$ on both Ag(111) and Cu(111) as well as $Dy(OETAP)_2$ on Cu(111) and Au(111), and single OETAP molecules on Au(111) all self-assembling in a very similar fashion, pointing to the fact that molecule-molecule interactions far outweigh surface-molecule interactions. Both double-decker species exhibit a peculiar random distribution of apparent heights or brightnesses in these islands, the source of which has yet to be determined. Brighter individuals can be irreversibly switched into darker ones by different forms of tip-sample interaction or annealing of the whole sample. The

central terbium atom's charge state has been investigated as a possible source of this effect with XPS, but a solid conclusion has yet to be reached.

3.2 Alkyne-functionalized Pyrenes

One recurring and successful *modus operandi* in surface science is to widen the scope of a study by investigating molecules, which are not only showing promising self-assembling behavior or other intermolecular interactions, but also some further physicochemical intramolecular property. This is especially the case for the chemical class of polyaromatic hydrocarbons (PAHs), which have certainly earned a significant amount of disrepute in human health-related issues [208, 209], but are nevertheless continually presenting valuable research examples in diverse branches of science, recently even in astrochemistry [210–212]. One such representative is pyrene (benzo[*def*]phenanthrene), one of the smaller PAHs, which, together with its derivatices, has a long-standing scientific history mainly because of its high quantum-yield fluorescence [213–217]. Further topics of interest are its ability to couple to and thereby functionalize carbon nanotubes and graphene [218–221], and its inherent self-assembling capabilities [222–227], both of which are usually investigated in conjunction with, or at least making use of, its fluorescence. Over the last fifteen or so years, pyrene derivatives have furthermore been investigated with scanning probe techniques [228–233], as they are under certain circumstances able to self-assemble on surfaces and due to their luminescence properties present just such an interesting dually capable system mentioned at the outset.

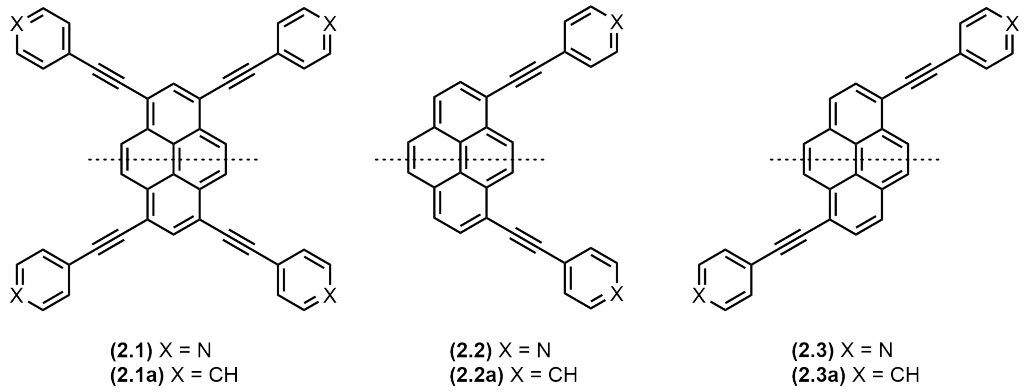

Figure 3.7: Chemical skeletal formulas of the pyrene derivatives investigated during this thesis.

Within this section the STM investigation of a family of pyrene derivatives functionalized with different ethynyl-based moieties shown in figure 3.7 will be discussed. The information contained herein is currently in preparation for publication [234] and a series

of preliminary studies have been conducted by Tobias Hoh [235]. In order to facilitate self-assembly upon adsorption pyrene backbones were functionalized with ethynylpyrid-4-yl moieties, which should be able to attractively interact with other such moieties via either H-bonds [225, 236] or pyridyl-metal-pyridyl coordination [237, 238] while still maintaining a certain degree of flexibility, which tends to be a favorable circumstance for self-assembling behavior. Backbones were either functionalized tetradentated (species (**2.1**)), designated as tetra-pyridyl-pyrene, or bidentated in a cis- ((**2.2**)) or trans-like ((**2.3**)) fashion, hence designated as cis- and trans-pyridyl-pyrene, respectively. The overall adsorption behavior without attractive intermolecular interaction other than possible van der Waals forces was investigated via a control group of pyrenes likewise functionalized with ethynylphenyl moieties (species (**2.1-3a**)) which will be designated in a similar way as x-phenyl-pyrene, where x is again either tetra, cis or trans.

3.2.1 Phenyl-terminated Control Group

Depositing molecules of the aforementioned control group onto a bare Ag(111) surface leads to flat-on adsorption for every member of the family (see figure 3.8). As expected, no attractive interaction between individual molecules can be observed in any case, instead a more or less uniform statistical distribution of molecules all over open crystal terraces becomes apparent, with step edges being decorated to saturation (not shown). The preferred decoration of steps indicates the molecules' ability to freely diffuse on the surface, which in turn points to physisorption rather than chemisorption.

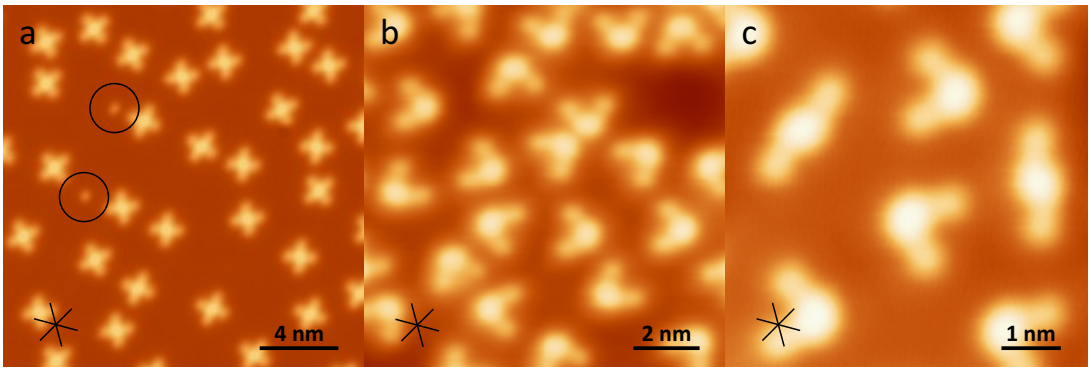

Figure 3.8: Adsorption behavior of phenyl terminated ethynyl-pyrenes on Ag(111). **a** - Overview image of tetra-phenyl-pyrene (**2.1a**) (+1 V, 5e-10 A). **b** - Closeup of cis-phenyl-pyrene (**2.2a**) (+0.1 V, 1e-10 A). **c** - High resolution image of two trans-phenyl-pyrene molecules (**2.3a**) in a preparation of (**2.2a**) (+0.1 V, 9e-11 A).

There is, however, still a distinct effect of surface-molecule interaction visible in the orientation of individual molecules. These tend to more or less closely align their short symmetry axis (dotted line in figure 3.7) with one of the dense-packed crystal

directions such that said axis is off to one side or the other by about 8 to 9±5°. This is especially nicely observable in the case of the cis-species (**2.2a**), which exhibits a characteristic pacman-like shape with one big, bright protrusion in the back attributed to the pyrene backbone and two dimmer lobes which can be attributed to the phenyl-ethynyl moieties (figure 3.8b), leaving no doubt as to the direction of the molecule's short symmetry axis. Surprisingly, this is not as easy for the x-shaped tetra-species (**2.1a**), because although the angles included between the legs (the four dim, peripheral lobes are attributed to the phenyl moieties) are nominally 120° and 60° and should thus be easily differentiated, this is in practice severely complicated due to the leg's, albeit limited, flexibility (figure 3.8a). Nevertheless, even if short and long symmetry axis can not be distinguished one at least observes the same three-fold orientational preference as in the cis case. Whether or not this is also true for the trans-species (**2.3a**) remains speculative, because only very few representatives of this module have been observed experimentally (figure 3.8c) as contamination in preparations of (**2.2a**), certainly not enough to acquire a sufficiently large dataset of statistical relevance. They exhibit an elongated z-shape, again with a bright central pyrene backbone lobe and two peripheral dime lobes attributed to the phenyl moieties, which due to its prochirality inherently leads to two different forms upon adsorption, both of which can conveniently be seen in the figure. From the adsorption behavior of their pyridyl-terminated counterpart (**2.1a**), which will be discussed in the following section, however, it is quite likely that also this species exhibits the same orientational preference. As an aside: in many preparations of phenyl-terminated species small, circular protrusions could sometimes be observed (see circles in figure 3.8a), which will be further discussed in section 3.3.2.

3.2.2 Pyridyl-mediated Self-assembly

As in the case of phenyl-terminated species the deposition of pyridyl-terminated molecules leads, in every case, to flat-on adsorption and free diffusion on a Ag(111) surface. Quite remarkably different now, however, is the intermolecular interaction, which leads to completely different self-assembled supramolecular architectures for the three species, even at low to medium coverages. Tetra-pyridyl-pyrene (**2.1**) readily forms extended, close-packed, and very regular islands even at low surface coverage (see figure 3.9a and b) with one border always attached to the bottom side of a step edge, suggesting that these act as nucleation sites.

The architecture exhibits a rhombic unit cell which, using the technique mentioned in section 2.1.4, can be tentatively assigned the following dimensions: a_1 = 15.6 Å, a_2 = 17.6 Å, α_1 = 99.2°, α_1 = 80.8°, and an angle ϕ = -13.5° between a_1 and the

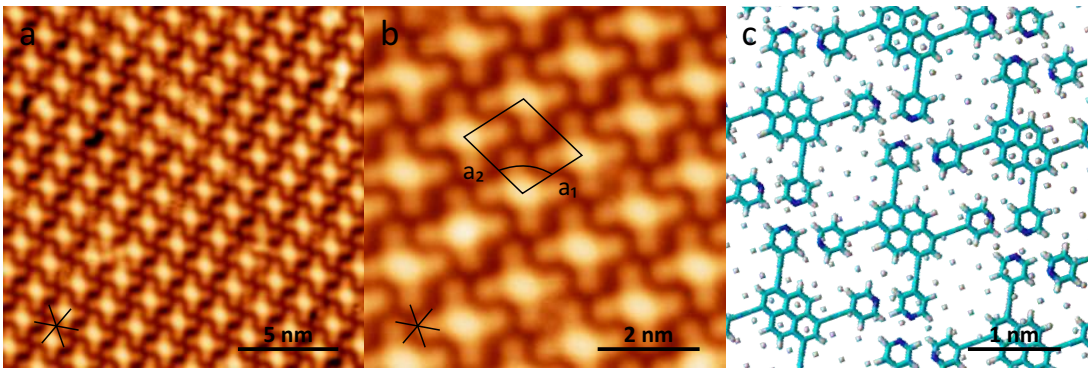

Figure 3.9: Self-assembled island of tetra-pyridyl-pyrene (**2.1**) on Ag(111). Stars indicate dense-packed crystal directions. **a** - Overview image (-0.2 V, 1e-10 A). **b** - High resolution image (-0.5 V, 1e-10 A). **c** - Tentative model of the assembly shown in sub-panel b.

closest dense-packed crystal direction (see figure 3.9c). The model reveals a quasi-commensurate overlayer where every other row of molecules in a_1-direction is adsorbed on identical adsorption sites (although the exact nature of these sites could not be determined experimentally, see section 3.1.1), which can be designated as $(\sqrt{29}\times\sqrt{37})$R-13.5° [202]. Again, as in the case of the phenyl-substituted species, a rotation of the molecule's short symmetry axis slightly off to one close-packed crystal direction is observable. The fact that this effect appears in all phenyl-terminated species and, as we will see, likewise in all assemblies of pyridyl-terminated ones, strongly suggests that its cause is an interaction between pyrene backbone and surface. Furthermore, a distinct interdigitation between adjacent molecules can be seen. This points to N-H bonds as the driving force of the assembly and, paired with the symmetry axis rotation, leads to an organizational chirality, as in principle for every crystal direction rotation off to both sides and thus two different interdigitation motifs (or synthons) should be possible with similar unit cells, but with either positive or negative angle ϕ. While indeed both of these mirror-symmetric domains were observed during our experiments (for example in figures 3.9a and b), all possible combinations or phases could not be recorded as this would have required extensive amounts of images of different islands. Also worth mentioning is a small cavity of $\sim$ 6x6 Å^2 can be observed between molecules in a_2-direction. This "pocket" will be of further interest in section 3.3.2.

Cis-pyridyl-pyrene (**2.2**) on the other hand tends not to form islands at coverages below one full monolayer, but instead agglomerates in the form of 1D-like chains or at most small clusters of six to ten individual molecules (see figure 3.10). Sub-panel a shows a preparation at low coverage. At medium coverages, shown in sub-panel b, (**2.2**) exhibits more irregular behavior with chains and clusters agglomerating in a seemingly uncontrolled way, although individual segments with a certain amount of

short-range order can still be observed. Chains and clusters are formed through two distinct intermolecular binding motifs: on the one hand N-H bonds between a pyridyl moiety and the pyrene backbone of an adjacent molecule (clearly observable within the cluster in figure 3.10a) and on the other a sort of head-to-head motif wherein two molecules face each other with some attractive interaction between adjacent pyridyl moieties, the latter of which is the predominant motif in chains and displays some kind of attractive interaction such that another pair of pyridyl-connected molecules may attach on either side, thus forming the chain. It is assumed that the head-to-head motif is facilitated by pyridyl-metal-pyridyl coordination involving a surface atom which is slightly pulled out of its plane by the attractive interaction [207].

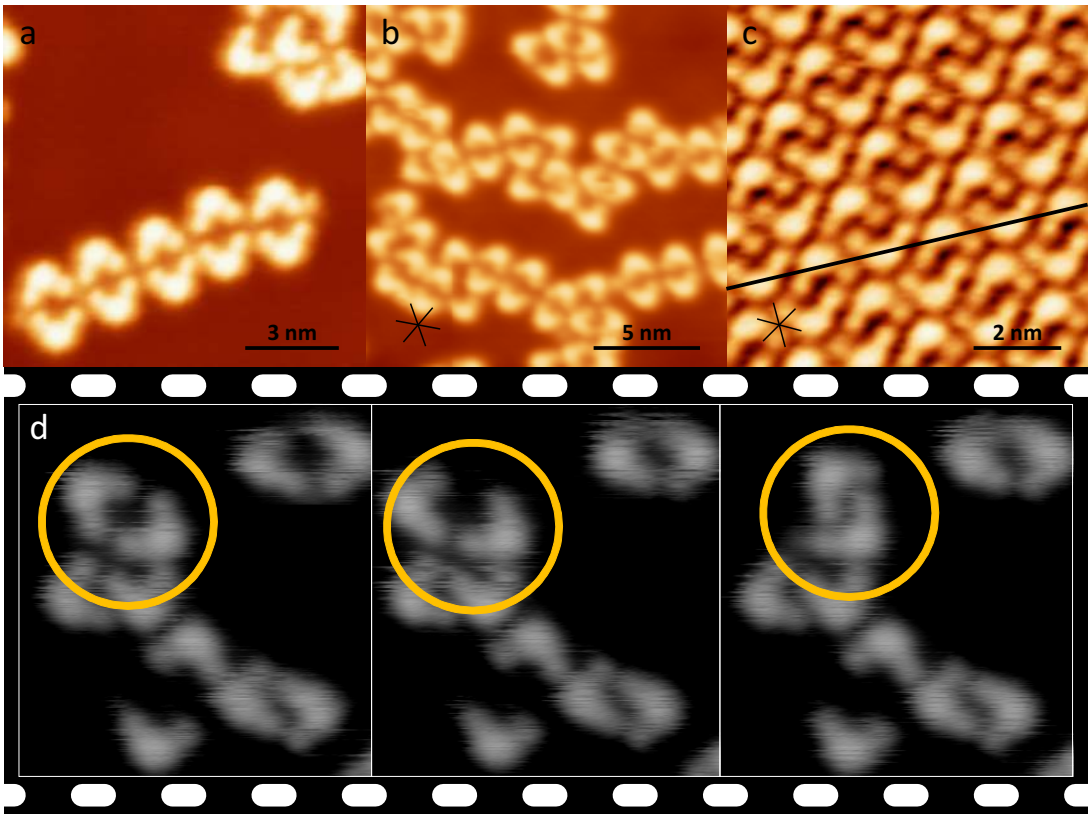

Figure 3.10: Supramolecular architectures of cis-pyridyl-pyrene (**2.2**) on Ag(111). Stars indicate dense-packed crystal directions. **a** - High resolution image of a short chain and a cluster at low coverage (-0.2 V, 1.5e-10 A). **b** - Closeup image of irregular chains at medium coverage (-0.2 V, 1e-10 A). **c** - High resolution image of (**2.2**) at ∼1 ML coverage (+0.1 V, 1e-10 A). **d** - Raw data image reel of a series of lateral manipulation experiments to investigate the head-to-head binding motif (-1.0 V, 8e-11 A).

The "bond" lengths between two head-to-head molecules forming such a dimer display a great range of flexibility, as can be seen in both low and medium coverage images, an effect which was investigated by a series of lateral manipulation experiments. This

was initially done to test the strength of a head-to-head bond by trying to move an intact dimer around on the surface, but quickly a great degree of freedom of the individual molecules became apparent (see figure 3.10d). It was even possible to instigate a third binding motif, wherein both molecules interdigitate to form a close-packed and chiral dimer, much like the interplay one can observe in self-assembled islands of the tetra-pyridyl species. This very binding motif, albeit a bit less dense with tiny pockets between the molecules, along with the N-H bond between legs and pyrene backbones mentioned above, defines the characteristic interaction when coverages around one monolayer are deposited and a tight-packed assembly can be observed (see figure 3.10c). Columns of dimers are held together by pyridyl-backbone attraction and in turn these columns are tightly packed by the sheer amount of molecules on the surface. At an angle to these columns a characteristic line pattern emerges, with molecules alternately facing in opposite directions. Due to the dimer's inherent chirality frequent crystal twinning can be observed along such lines (black line in figure 3.10c).

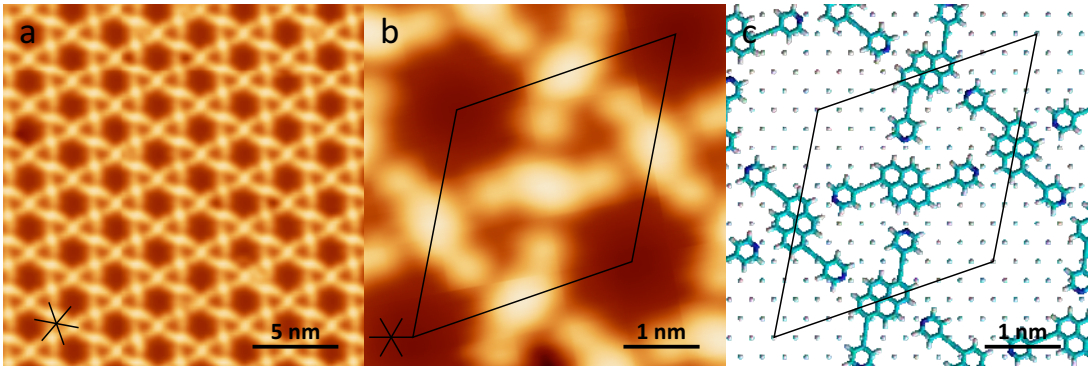

Figure 3.11: Self-assembled Kagome-patterned island of tetra-pyridyl-pyrene (**2.3**) on Ag(111). Stars indicate dense-packed crystal directions. **a** - Overview image (-0.2 V, 1e-10 A). **b** - High resolution image of the structure's unit cell (-0.02 V, 5e-10 A). **c** - Tentative model of the assembly shown in sub-panel b.

The third and only prochiral member of this family, trans-pyridyl-pyrene (**2.3**), forms, much like its tetra counterpart, very regular and extended islands, also at low surface coverage. These are once again always pinned on one edge to the bottom side of a step edge, which again hints to their role as nucleation sites. However, the pattern formed is now an intriguing, open-porous Kagome lattice or trihexagonal tiling with a perfectly hexagonal unit cell (see figure 3.11a) [239]. Characteristically for Kagome lattices these islands feature pores of two different diameters, namely ∼6 and ∼18 Å. High resolution images show that these assemblies are resulting from N-H bonds between pyridyl moieties and pyrene backbones of adjacent molecules. Similar to species (**2.1**) and (**2.2**) the molecules are again adsorbed in such a way that the short symmetry

axis of the pyrene backbone is rotated slightly off of a dense-packed crystal direction. Interestingly, islands of this kind are exclusively formed by molecules of the same chirality which in turn results in organizational chirality of the assembly, hence again, as in the case of the tetradentated species, two mirror-symmetric domains are possible (figures 3.11a and b show both of these). The resulting unit cell was obtained via the techniques mentioned in section 2.1.4 and found to be perfectly commensurate with the underlying crystal which is reflected in the model in figure 3.11c. The following dimensions were determined: $a_1 = a_2 = 30.6$ Å, $\alpha_1 = 1/2\alpha_2 = 60°$ with an angle included between either unit vector and the closest dense-packed direction of $\phi = \pm\ 19.1°$, depending on the chirality of the assembly. This overlayer can thus be designated as a $(\sqrt{112}\text{x}\sqrt{112})\text{R}\pm19.1°$ superstructure relative to the crystal lattice [202]. The lattice's commensurability in conjunction with the rigidity of its three-fold N-H bonded synthons leads to an amazingly steady long-range order. Islands in the 0.1 μm^2 size regime have been observed.

3.2.3 Summary

In conclusion, the STM study of a family of ethynyl-functionalized pyrenes was presented and discussed in this section. A control group of bi- or tetradentated pyrenes functionalized with ethynylphenyl moieties was capable of sublimation and flat-on adsorption on Ag(111) and showed, as expected, a random surface distribution and hence no attractive interaction between individual molecules. Ethynylpyridyl-terminated counterparts of these control molecules which also allowed for sublimation and flat-on deposition, however, exhibited significant attractive interaction through a multitude of different binding motifs. The molecular synthons thus formed lead to a diverse number of different supramolecular architectures, some of which exhibited surface-organizational chirality either through them consisting of prochiral monomers or chiral synthons, or both. Only the cis-pyridyl-pyrene species showed no capability of forming regular, self-assembled islands at sub-monolayer coverages, but still exhibited an interesting head-to-head binding motif, presumably incorporating silver surface atoms in a pyridyl-metal-pyridyl coordination. Good use was made of a method developed and discussed in section 2.1.4 to accurately deduce unit cell dimensions from approximately measured lengths and angles in order to fully characterize and describe most of the investigated architectures.

3.3 Limitations of OMBE

As this thesis is predominantly a work with a focus on highlighting the immense assets of electrospray ion beam deposition and its advantages compared to using such

techniques as organic molecular beam epitaxy we will, in this section, emphasize on some of the drawbacks of OMBE, particularly with respect to preparations for use with scanning probe microscopy techniques. Most of the material presented here stems from experiments conducted on the systems introduced within the two previous sections, but some additional findings from other works, or experiments conducted within the framework of this thesis, but too short to warrant granting them a separate section, will be featured as well.

3.3.1 Thermolability

Perhaps the most obvious and immutable drawback of OMBE, at least in the spirit of this work's introductory remarks on "more is more", is given by the thermolability inherent in all organic molecules, which are heavier than a certain molecular mass or of a particularly unstable structure, that is their "willingness" or ability to undergo decomposition, disproportionation or polymerization reactions at elevated temperatures. These molecules are thus not suitable for deposition via OMBE and put a somewhat natural stopper on the technique's capabilities and subsequently on the scope of possible surface scientific experiments as well. A defining thermolability criterion is not easily found and predicting a molecule's thermal stability is next to impossible, as this strongly depends on its chemical structure and potential energy landscape, most important about which are the number of possible decomposition pathways and their respective energy barriers [240–242]. However, empirical studies relating some basic elements of chemical structure to overall thermal stability have been conducted and may serve as guidelines for a rough estimate on whether or not a molecule may be suitable for deposition with OMBE [243–245]. Molecules at or above this limit of structural integrity are thus either completely inaccessible to STM studies relying on OMBE or can, at the very least, lead to contamination by co-adsorption of cracked species or byproducts, which have formed in the OMBE crucible due to intermolecular interactions. Furthermore, molecules investigated in scanning probe experiments are often tailor-made. Choosing a suitable molecule for de-novo synthesis is thus challenging in two regards, because even if its synthesis bears fruit there still remains the question of its suitability for deposition via OMBE. This is further complicated by the fact that publishing negative results in science, which in this case would mean studies of non-sublimable molecules for example, is increasingly getting out of style [246] while the number of peer-reviewed, but still irreproducible results steadily increases [247–249], even in very "hard" fields such as physics [250, 251]. The much cited paradigm of science having a kind of "self-correction" mech-

anism is thus slowly being undermined, which, not only when choosing molecules for synthesis, leads to more trial and error than necessary.

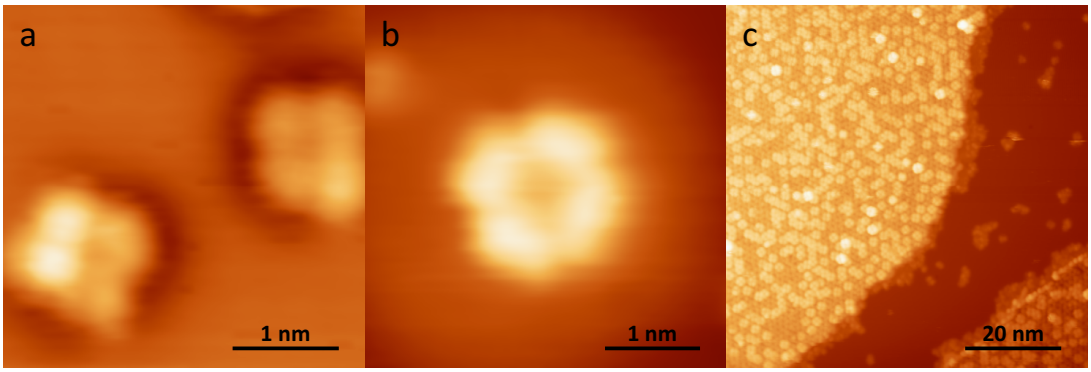

Figure 3.12: Thermolability observed in preparations of $Tb(OETAP)_2$ on Ag(111). **a** - High resolution image of single OETAP molecules (+0.5 V, 7e-11 A). **b** - High resolution image of an intact $Tb(OETAP)_2$ molecule for comparison (+1.0 V, 8e-11 A). **c** - Overview image of a contaminated preparation (+1.1 V, 1e-10 A).

Thermolability of a molecule does not necessarily imply that it is completely impossible to sublime. If a suitable deposition temperature can be found which is close, but not above the decomposition temperature, a certain ratio of intact vs. cracked species will be deposited. During the course of this thesis thermolability of both kinds was encountered in two different adsorbates, the first of which, $Tb(OETAP)_2$, has already been discussed in section 3.1 and could readily be sublimed and deposited. However, preparations of this sandwich complex almost always include at least some contamination of cracked single OETAP ligands. This becomes exceptionally apparent when dosing the molecules onto a Cu(111) surface, where they prefer to stick to open terraces and can be clearly observed while scanning (see figure 3.3e). On Ag(111) surfaces only solitary individuals or at most groups of three to four are ever observed isolated on terraces (see figure 3.12a). Luckily, these can easily be distinguished from intact double-deckers by their shape and apparent height (cf. figures 3.12a and b) or tip-induced rotation of the upper ligand (see figure 3.2). The small amount of single OETAP observed on Ag(111) suggests either preferred decoration of step edges or, more likely, segregation and self-assembly into islands which has been observed for dedicated preparations of OETAP on Au(111) [201]. Presumably, in our experiments these self-assemblies were never found during imaging as only a negligibly small percentage of the whole crystal is ever imaged even during very extended scanning probe measurements. Even if 1000 images of $1\mu m^2$ size were obtained from a single sample during an experiment, with both of these numbers being gross overestimations of standard procedures, still only $1 \cdot 10^{-5}$ parts of the surface area of a sample with a 10 mm diameter would have been

imaged. This can make finding, and reproducibly investigating, segregating and/or self-assembling cracked species, which amount to just a few percent of the overall deposited molecules, very tedious. In turn, this is both bane as well as boon of the technique as some contaminations do not jeopardize experimental findings because they may simply seldom be encountered. Of course, this may or may not be true for other techniques used in conjunction with OMBE. Especially spectroscopic methods often produce data averaged over the whole sample surface or a significant part of it, thus easily running afoul of such adulterating contaminations.

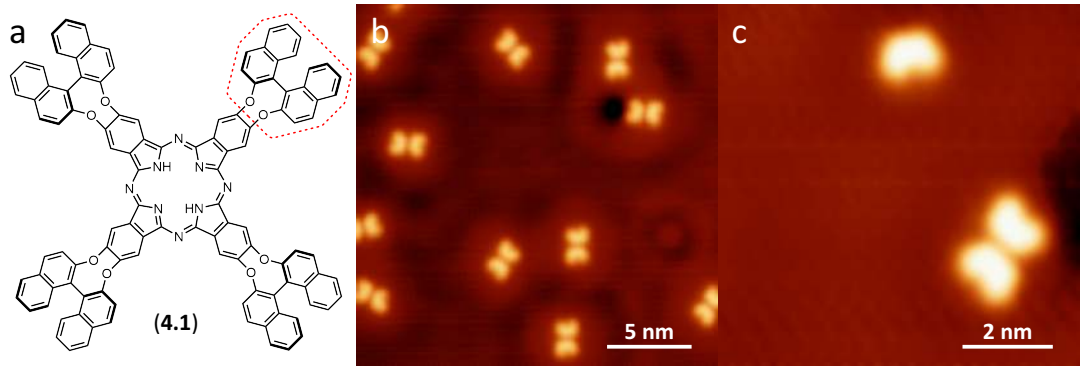

Figure 3.13: Thermolability in a chiral extended phthalocyanine. **a** - Chemical formula of (**4.1**) with binaphthoxy moiety outlined in red. **b** - Butterfly-like, presumably dimerized cracking product of (**4.1**) on Ag(111) (+0.05 V, 6e-11 A). **c** - Single dimer and a monomer produced via tip-sample interaction (-0.05 V, 6e-11 A) [252].

The second example of thermolability directly encountered during this thesis was the case of a chiral phthalocyanine functionalized with binaphthoxy moieties shown in figure 3.13a. Its investigation was intended a first step towards a potential chiral single molecule magnet sandwich complex with said phthalocyanine as the ligand. Upon adsorption on Ag(111) however, no intact molecules have so far been found. At moderately low deposition temperatures either no adsorbate or conglomerations of contamination can be found. Increasing the deposition temperature leads to more contamination and eventually butterfly-like, isolated structures can be observed (see figure 3.13b). These are too small to be attributable to the chiral phthalocyanines, as they are only marginally bigger than unfunctionalized phthalocyanines ($\sim$ 20 Å vs. $\sim$ 15 Å)[253], do not exhibit a characteristic cross-shape, which should be expected for such a rigid molecule, and can furthermore be split into two mirror-symmetric parts very easily by surprisingly mild tip-sample interactions like lateral or vertical manipulation, or nearby tip forming procedures (figure 3.13c), a structural frailty, which would be utterly impossible to observe if there was an intact phthalocyanine backbone. Presumably, these structures can be attributed to be dimers of the binaphthoxy functional groups split off

of the phthalocyanine at elevated temperatures, but as to their binding motif a sensible model has yet to be developed. Investigation of this molecule is still ongoing, but it is unclear whether a suitable window of deposition temperatures can be found to enable sample preparations with intact species.

3.3.2 Contamination

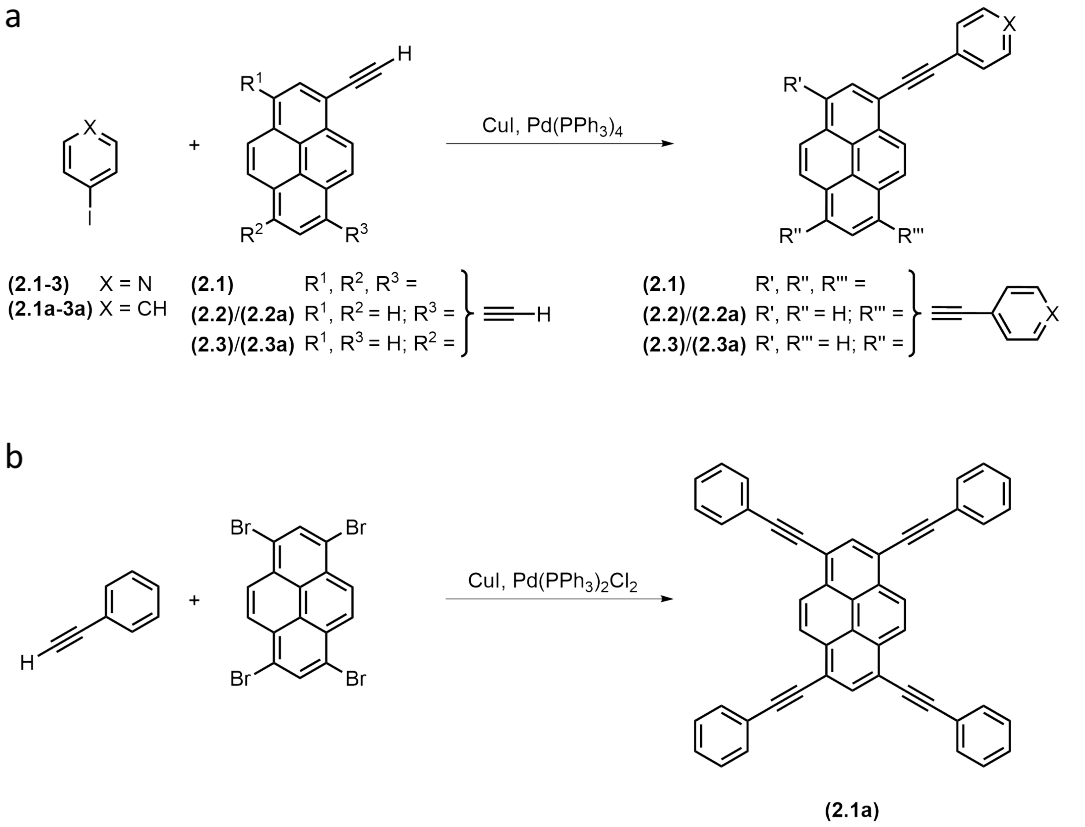

Figure 3.14: Synthesis of the family of alkyne-functionalized pyrenes discussed in section 3.2. **a** - Synthesis of species (**2.1-3**) and (**2.2-3a**). **b** - Synthesis of species (**2.1a**).

Thermolability is, of course, not the only source of observable byproducts or cracked species on a sample by far. Even if molecules are thermally stable and can be nicely deposited in an intact manner additional adsorbates may still be encountered if the feed material is itself contaminated to begin with. Usually, such contaminations can be gotten rid of through a process called degassing, wherein the OMBE crucible containing the feed material is heated for several hours (sometimes even days), but before any actual sample preparation is taking place. Small molecular weight contaminations are thus purged from the feedstock and relatively pure material left over for deposition. Alas, this procedure is not fool-proof. Contaminants of similar weight as the analyte or with a particularly strong affinity to be embedded in the analyte's crystal structure

can only be removed partly and will thus always be co-deposited in every subsequent preparation. If OMBE crucibles are re-used from one investigated molecule to the next, care has to be taken in order to avoid cross-contamination, but a much more common source for such contaminants are byproducts or leftover reactants of the analyte's actual chemical synthesis.

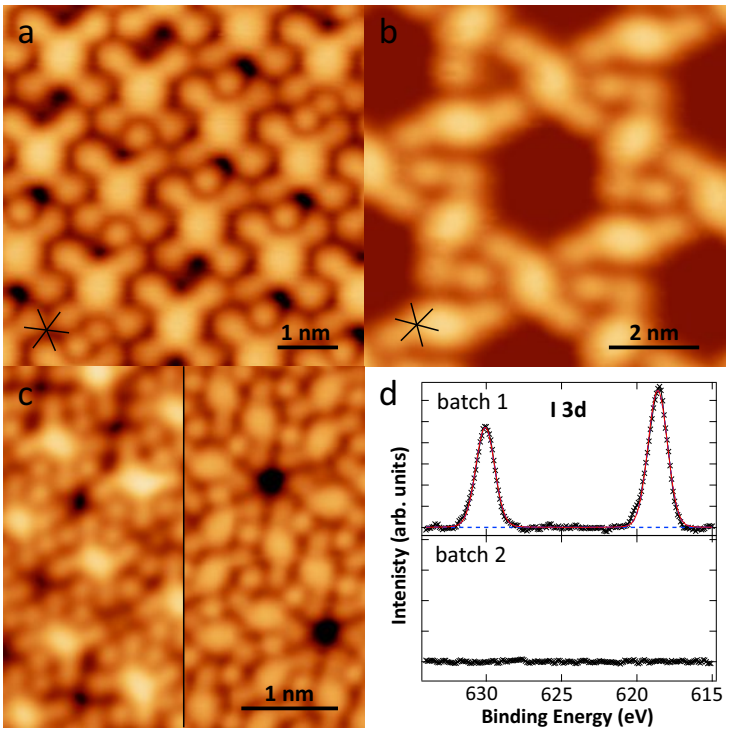

Figure 3.15: Preparations of alkyne-terminated pyrenes showing circular protrusions attributed to iodine contaminants. **a** - Tetra-pyridyl-pyrene (**2.1**) (-1.0 V, 5e-11 A). **b** - Trans-pyridyl-pyrene (**2.3**) (+0.1 V, 9e-11 A). **c** - Phases of (**2.1**) and (**2.3**) with high iodine content (left: +0.1 V, 9e-11 A; right: -0.2 V, 2e-10 A). **d** - XPS comparison of the I3d region for a contaminated (1) and a clean batch (2) of (**2.1**).

A textbook example is given by the family of alkyne-functionalized pyrenes discussed in section 3.2. These molecules were synthesized using a Pd-catalyzed Sonogashira-Hagihara cross-coupling reaction (SI in [234]) of either 4-iodopyridine or iodobenzene with acetylene terminated pyrene cores (see figure 3.14a), which in turn had been synthesized in a similar fashion from brominated or iodated pyrene cores and trimethylsilylacetylene [254–256]. The only exception to this pathway being tetra-phenyl-pyrene (**2.1a**), which had been obtained directly by cross-coupling of tetrabromopyrene with phenylacetylene (see figure 3.14b). From a stoichiometric point of view a large quantity of halogen-containing byproducts (mostly HX) is released during these reactions, as much as eight times the product molarity in the case of tetra-pyridyl-pyrene (**2.1**). It is unclear whether from these byproducts or from the CuI catalyst used, but in some

batches a contamination of iodine atoms was observed during STM measurements after deposition on Ag(111) as small circular protrusions at all utilized bias voltages (see figure 3.15).

Tetra-pyridyl-pyrene (**2.1**) assemblies are able to trap either one or two of these iodine atoms in the pockets mentioned in section 3.2.2 (figure 3.15a). Regarding changes in the assemblies' internal structure due to this additional participant, high resolution images show that most molecules are still oriented parallel to each other with a small minority (5% or less) now being incorporated at a right angle without deteriorating influence on the long-range order of the assembly. As this is not the case for clean tetra-pyridyl-pyrene (**2.1**) assemblies it acts as an indicator as to the widening influence of iodine on the structure's unit cell, which now appears not to be quasi-commensurate, but incommensurate and elongated with respect to assemblies of clean batches with dimensions of $a_1 = 15.3 \pm 0.5$ Å, $a_2 = 18.8 \pm 0.5$ Å, $\alpha_1 = 80 \pm 5°$, and $\alpha_2 = 100 \pm 5°$. Despite this incommensurability no Moiré pattern could ever be observed in long range images. It is worth noting, however, that a tentative model can be constructed where all iodine atoms are adsorbed on identical adsorption sites, which are assumed to be hollow site as these have been long known to be the preferred sites for iodine on Ag(111) [257]. Whether pockets are filled with zero, one or two iodine atoms is thus presumed to be the result of an intricate minimization balance between the assembly's lattice energy and the iodine's adsorption energy. Further on, however, we will show that this balance can be severely tilted in the iodine's favor if enough contaminant is present.

Contaminated assemblies of trans-pyridyl-pyrene (**2.3**) incorporate iodine atoms in the small cavities (see figure 3.15b), which, due to the assembly's commensurate nature, can easily always feature a hollow site (see model in figure 3.11c). Rarely, single iodine atoms are encountered in the big cavities as well, but only ever one and always tucked neatly into one of the corners. In contrast to assemblies of (**2.1**) here the unit cell dimensions, or commensurability for that matter, are not perturbed by this contamination, presumably due to the hollow sites being readily available. However, in both cases new structures may arise if the amount of co-adsorbed iodine is high enough. This was achieved by chance through a double preparation using contaminated batches of both (**2.1**) and (**2.3**), although as to why in this case assemblies with distinctly more iodine content as compared to two single preparations were observed remains an open question. The tetra-species' assemblies are now stretched in both directions with iodine occupying interstitial pockets almost always in pairs (left side of figure 3.15c) while trans-species assemblies show complete restructuring into two much more dense-packed phases (one of which is shown on the right hand side of figure 3.15c). Interestingly, little or no evidence was found for iodine contaminations in preparations of

cis-pyridyl-pyrene (**2.2**) or any of the phenyl-terminated species (**2.1-3a**) other than the odd circular protrusion, which may just as well be attributed to any other contamination (see circles in figure 3.8a). This suggests that either these batches were free from contamination or that no significant attractive interaction actually exists between the functionalized pyrenes and iodine and the contaminant is thus only incorporated into the two aforementioned self-assemblies out of geometrical reasons similar to the lock and key model, which is so often encountered in nanoscience. The clean preparations of (**2.1**) and (**2.3**) shown in section 3.2 were obtained from batches, which had been synthesized at slightly different reaction conditions, but this was not the case for any of the other molecules, so presumably preparations of these were contaminated as well, but due to non-attractive behavior the iodine segregated and was never observed experimentally.

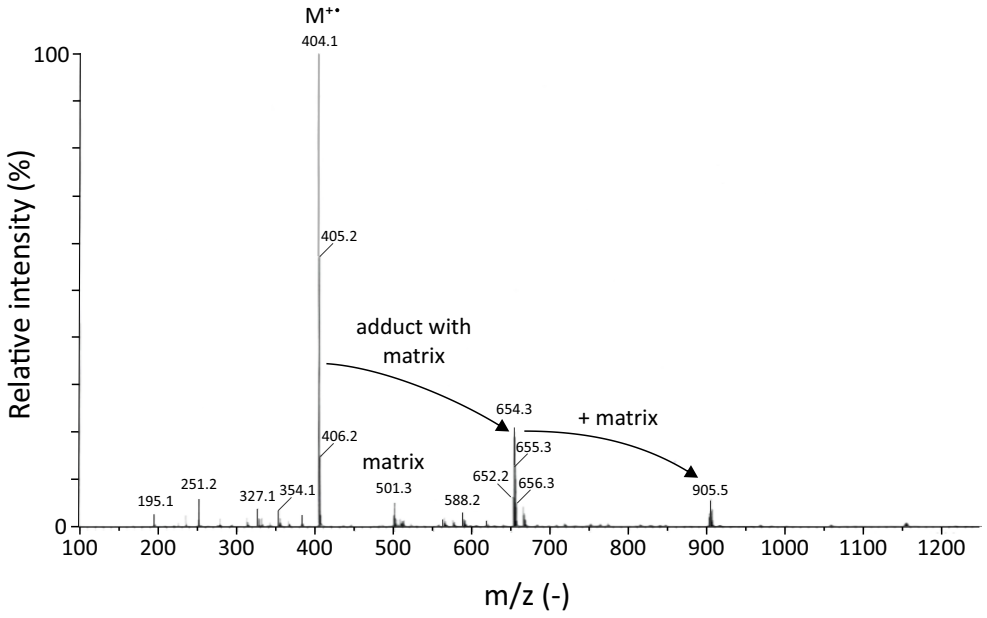

Figure 3.16: MALDI-MS spectrum of a contaminated batch of (**2.3**).

As a last remark it is worth mentioning, that such contaminations can often be very hard to detect prior to the actual STM experiments. The most widely-used analytical instrument in the organic chemist's toolbox is probably NMR spectroscopy, which is great for structural analysis, but suffers from a very low sensitivity [258]. Of course, in the present case of iodine byproduct even an arbitrarily sensitive NMR spectrometer would not have detected the contamination unless an ^{127}I measurement would have been conducted. Even with more sensitive techniques the experimenter can run afoul of adverse conditions. Figure 3.16 shows a mass spectrum of a contaminated batch of (**2.3**) obtained through matrix-assisted laser desorption/ionization mass spectrometry (MALDI-MS) with no visible trace of ^{127}I or significant other contaminations, for that

matter. However, here MALDI was conducted in the positive ion mode, which, of course, iodide I^- is not accessible with. Only XPS measurements of two different batches of molecules could finally and clearly show that the contaminant was indeed iodine (see figure 3.15d).

3.3.3 Deposition Parameters

Apart from such serious limitations and drawbacks as thermolability and contaminations there are a series of minor intricacies, which tend to complicate working with an OMBE apparatus. One example is the need to exchange feedstock powder between experiments, which always makes some maintenance downtime necessary, as has been mentioned in section 2.2. Probably more costly in overall measurement time, however, is the need to find suitable deposition parameters for novel feed material. Even if the sample can be positioned precisely and reliably relative to the OMBE and always the same shutter position is used there are still two parameters left, upon which surface coverage depends, namely deposition time and temperature. The former has a linear influence while the latter's is exponential via Arrhenius' law. This usually makes a tedious process of repeated sample preparation and examination necessary wherein deposition temperature and/or time are increased step-wise from a first educated guess until some molecules can be observed on the surface. In a low temperature setup such as the Createc machine used in this thesis, which necessitates a certain cool-down phase for freshly prepared samples, one such cycle can only be repeated maybe twice or three times in one day. Thus, finding suitable deposition parameters usually takes up a few days right at the start of new projects.

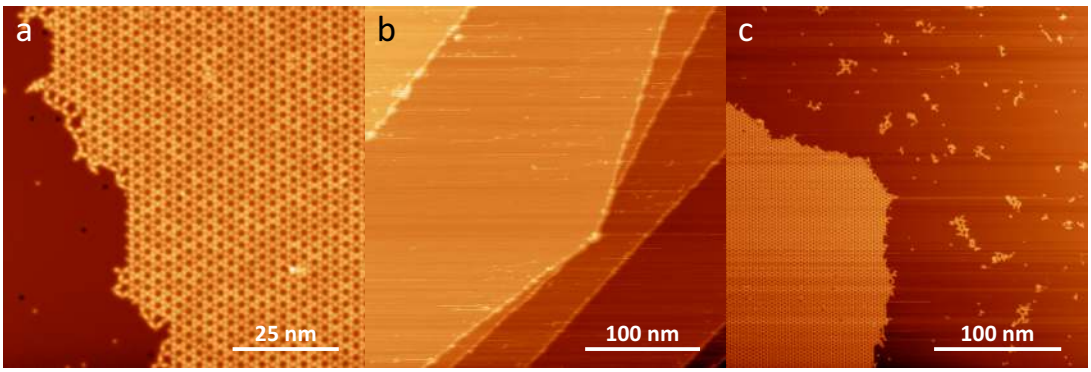

Figure 3.17: Comparison of deposition parameters for two batches of trans-pyridyl-pyrene (**2.3**). **a** - Molecules of batch 1 deposited for a total of 40 minutes at 320-340°C (+0.3 V, 1e-10 A). **b** - Empty preparation after deposition from batch 2 for 30 minutes at 340°C (+2.3 V, 1e-10 A). **c** - Molecules again from batch 2 after 10 minutes deposition at 230°C (+2.0 V, 2e-10 A).

Remarkably, under certain circumstances this tedious procedure might be necessary even for molecules, which had previously already been investigated with suitable deposition times and temperatures. Figure 3.17 shows such a case in which two different batches of trans-pyridyl-pyrene (**2.3**) showed two completely different sublimation behaviors. Batch 1 could usually be deposited in sub-monolayer coverages at ∼340°C within a few tens of minutes, but when the new batch 2, which had been synthesized slightly differently (see previous section), was used for the first time initial preparations yielded only very dirty samples and upon examination of the powder left in the crucible this was found to have undergone some kind of pyrolytic reaction. It was only after filling the crucible with fresh material and a cautious renewed search for parameters that a radical change in deposition temperature became apparent with batch 2 yielding similar surface coverages a full 100°C below that of batch 1. Interestingly, a new batch of tetra-pyridyl-pyrene (**2.1**) had also been synthesized under similarly changed reaction conditions, but this showed no such shift in sublimation temperature. Investigations regarding the nature of this behavior, which is presumably due to a change in the powder's aggregation state, are still being conducted.

Such unusual effects, however, are not the only source for changing deposition parameters. A very common behavior, especially in extended series of experiments, is the need to gradually increase the deposition temperature in order to obtain similar surface coverages. This can be due to unwanted polymerization side reactions making parts of the powder unavailable or simply because the crucible filling is nearing its end. Dual depositions, wherein two different molecules are deposited onto the same sample, are at a double disadvantage due to this and thus tend to be even less reproducible. If at some point one preparation is found to contain an insufficient amount of surface coverage usually a second preparation is made on top of the already "coated" sample. During this thesis this had to be done many times, including during experiments on a molecule, designated as BO-ADPM [259, 260], which was collaboratively investigated together with Alissa Wiengarten to further elucidate its potential as a donor material in organic photovoltaics (see figure 3.18). While most of the experimental results can be found in her PhD thesis [76] some interesting observations regarding deposition behavior are also worth noticing. In order for the reader to better understand what figure 3.18 is showing it should be mentioned that BO-ADPM adsorbs flat-on on Ag(111) and can be observed as an almost quadratic ensemble of four lobes, one of which is always of markedly increased apparent height compared to the others (figure 3.18b:I). This is attributed to the oxyphenyl moieties bending out of the molecular plane in opposite directions, which can be seen in the side-view of an energetically optimized geometry obtained via the

HyperChem software suite. Subsequently, due to this non-planar adsorption geometry attractive interaction between individual molecules arises and oligomers containing mostly two, three or four molecules are formed even at very low surface coverages.

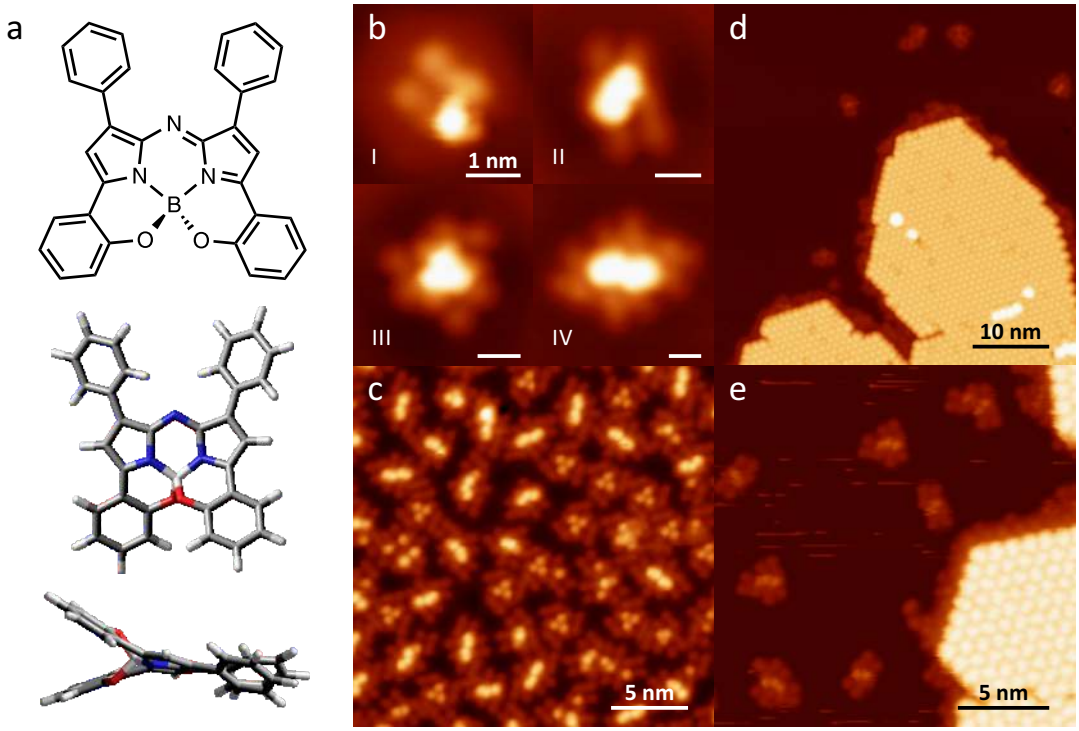

Figure 3.18: Investigation of BO-ADPM on Ag(111). **a** - Skeletal formula of BO-ADPM and top as well as side view of its energetically optimized geometry obtained via HyperChem. **b** - Monomer and oligomers of BO-ADPM on Ag(111) with the number of molecules given in roman numerals (I: -0.3 V, 5e-10 A; II/III: -0.1 V, 2e-10 A; IV: -0.6 V, 1e-10 A). **c** - Preparation intended for slightly below full monolayer coverage (-0.1 V, 1e-10 A). **d** - Double preparation of BO-ADPM and C_{60} on Ag(111) (+0.7 V, 1e-10 A). **e** - Additional dosing of BO-ADPM onto the preparation shown in sub-panel d (+1.0 V, 8e-11 A).

In order to investigate the electronic interplay between BO-ADPM and a potential electron acceptor a series of dual preparations was made with C_{60} as a co-adsorbate. During one experiment a coverage close to one monolayer of BO-ADPM was deposited in order to add C_{60} on top and still have a sufficient amount of free Ag surface for tip formings (see figure 3.18). This worked reasonably well, but it should be noted that obtaining such a coverage is mostly a matter of fortunate circumstances. In an earlier approach first a low coverage of C_{60} was prepared in order to then deposit BO-ADPM on top of the islands formed. From figure 3.18d can be seen that in this case deposition parameters for BO-ADPM were misjudged at first and additional molecules had to be dosed on top, leading to loosely adsorbed contamination being pushed around by the tip, which is visible as horizontal stripes in the images (fig. 3.18e).

In general, the need for secondary preparations tends to increase contamination as the sample is being manipulated around in the chamber and shutters are opened and closed, giving off adsorbed molecules, which can in turn contaminate the sample even further. This can be mitigated by using a quartz microbalance in the chamber to accurately measure the amount of deposited molecules in the first place, but even then finding suitable deposition parameters is necessary to begin with as such a microbalance can of course not distinguish between intact molecules and cracked species or dirt being sublimed out of the crucible.

4

Electrospray Ion Beam Deposition: A Sprayed Solution

Although by now the discerning reader may have probably drawn the preliminary conclusion that this work is but a vituperation on all things OMBE and that electrospray ion beam deposition (ESIBD) is the one and only solution to every experimentalist's last problem, this is, alas, far from the truth. The reasons for this are two-fold: on the one hand, OMBE does have its uses, especially because it enables a fast and straightforward deposition method for a still quite large scope of molecules, which is well understood and easy to maintain. On the other hand, straightforwardness, or rather lack thereof, is exactly ESIBD's greatest weakness, and significantly so. Within the following chapter we will explore its many advantages, especially with regard to OMBE's drawbacks discussed in the last chapter, but also some disadvantages and hurdles, which have to be overcome in order to fully open the limits on deposition of fragile molecules. As the whole process is rather complex, at first the current state of the machine will be discussed to give the reader an overview, which should act as a reference base. From there, its individual parts will be presented and explained in more detail within dedicated sections.

Large parts of the work presented here would have been impossible without the energetic and fruitful help and collaboration of a number of amazing bachelor and master students. Their works have all contributed to the current state of the machine in one way or another and their theses contain further information well worth reading up on [109, 159, 178, 261–265].

4.1 The Setup in its Current State

Figure 4.1 shows an isometric overview of the combined ESIBD and STM setup, which is the focus of this work. The opaque chambers on the left represent the existing STM setup consisting of a preparation chamber (the rear one in blue) and the actual measurement chamber (left most, light green), which have been described in previous works [78, 79]. The ESIBD setup is shown translucent on the right and consists, in ion beam direction, of the ESI source (green), four differentially pumped chambers (purple and yellow), and finally the preparation chamber (rust).

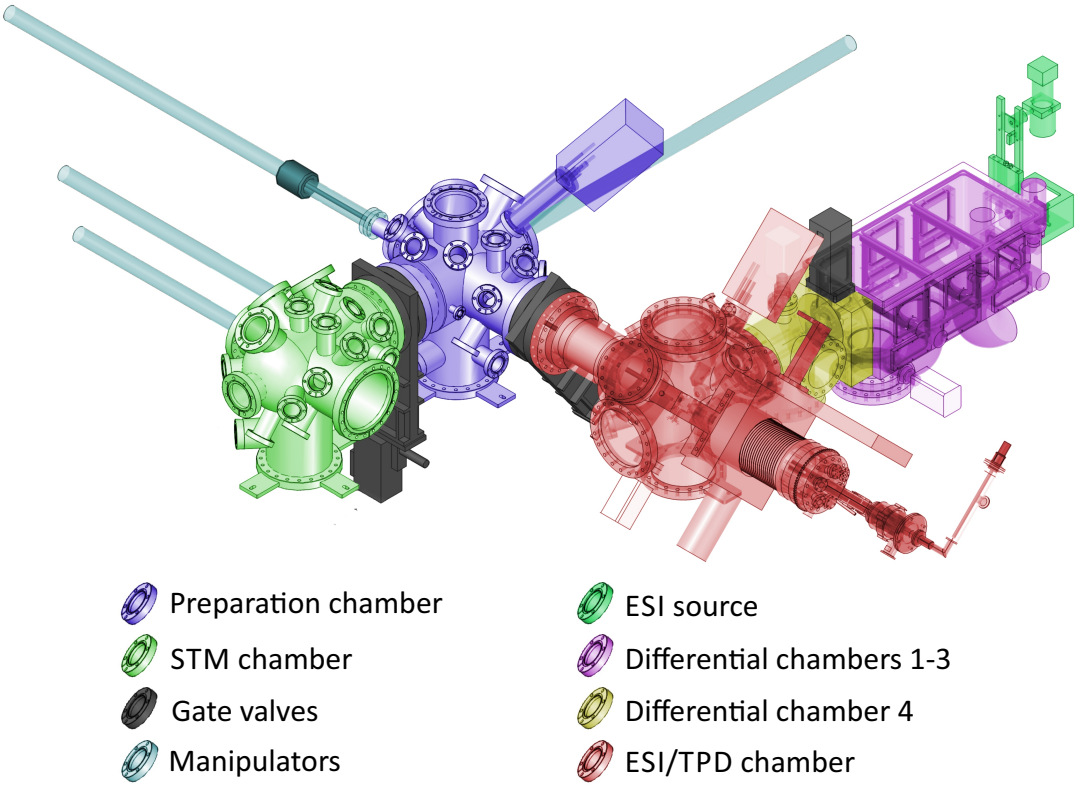

Figure 4.1: Color-coded isometric overview of the combined ESIBD-STM setup developed during this thesis. Pumps, mounting racks and further accessories are not shown.

At the very right of figure 4.1 one can see the actual ESI source (green), which is the only functional part at atmospheric pressure. A camera mounted on top of it allows for observation of the needle during spraying. This is necessary for two purposes, one being simple position control, the other observation of the current spray mode when adjusting the needle voltage. Not shown here is the syringe pump, which supplies the feed material to the needle. Starting from the source, the ions are transferred into the vacuum system through an atmospheric pressure interface (API, see section 4.2). As the API introduces a lot of air into the system a series of differentially pumped chambers is

necessary to reduce the pressure step-wise until ultrahigh vacuum conditions are reached (see section 4.3). The first three vacuum chambers are actually just one aluminum box with dividing walls separating it into three parts (thus only one color in figure 4.1). These dividing walls also act as mounting fixtures for the ion guides and orifices connecting the chambers. The whole box is mounted on its own rack and can, along with pumps and further accessories, be completely detached from the high/ultrahigh vacuum part, which is affixed to another rack. This modularity makes relatively straightforward maintenance and restructuring possible. Flexibility is further increased by the fact that the aforementioned aluminum box containing the first three chambers actually has a lid, which can be easily removed, thus allowing direct access to the ion guides and cabling contained therein. Each compartment has a flange at the bottom for pump connection as well as several side flanges for electronic feedthroughs, pressure gauges or other accessories. The front most flange holds the ESI source while at the very back connection to chamber 4 is implemented. Furthermore, the dividing walls are removable as well and can be customized to suit the needs of special experiments. All flanges and the lid are made gas-tight through the use of custom O-rings while vacuum grade silicon sealant is used for the dividing walls as these are not removed very often.

Differential chamber 4 serves, just as all prior differential chambers, the only purpose of further reducing the pressure. It is needed because the aluminum box could not be connected directly to the preparation chamber due to too high pressure differences. Finally, after passing chamber 4 the ion beam reaches the preparation chamber where the sample can be placed on a small manipulation and heating/cooling mounting stage. The interface between ESIBD and STM parts is implemented through a very flexible DN100 bellow, which allows for a certain difference in chamber levels between ESIBD and STM. This is necessary as the latter can be floated on pneumatic legs to reduce vibrational noise while the former is at a constant level. In order to prevent complete compression of the evacuated bellow by atmospheric pressure a set of strong compression springs is installed in parallel (not shown). This still allows for more flexibility than a rigid spacer while at the same time reducing vibrational coupling of ESIBD and STM to a manageable minimum. Convenient sample manipulation is facilitated through a series of manipulators, the longest of which can be used to transfer samples from one of the two setups to the other, thus functionally connecting ESIBD and STM.

At crucial points gate valves can be used to separate parts of the combined setup from the rest. This can be done between STM measurement and preparation chamber, between STM and ESIBD setup, and finally also between differential chambers 3 and 4 of the ESIBD setup. It is thus easily possible to completely separate ESIBD from STM with, for example, either one evacuated while the other can be vented for maintenance.

The gate valve between differential chambers 3 and 4, which is fully integrated into chamber 4, is necessary, because the ESI preparation chamber and chamber 4 already represent an ultrahigh and high vacuum environment, respectively. These chambers thus have to be pumped at all times as otherwise frequent bakeouts would be necessary to reach the respective base pressures again. This is not the case for the first three differentially pumped chambers, however, where chamber 3 reaches a base pressure only in the 10^{-6} mbar regime, perfectly reachable without a bakeout procedure. Furthermore, gas loads and therefore necessary pumping power are highest in this part of the system, thus relatively big and noisy pumps are used, which can severely impair STM sensitivity. For these reasons the first three differential chambers are only pumped if and when an ESIBD preparation is actually taking place, and vented otherwise.

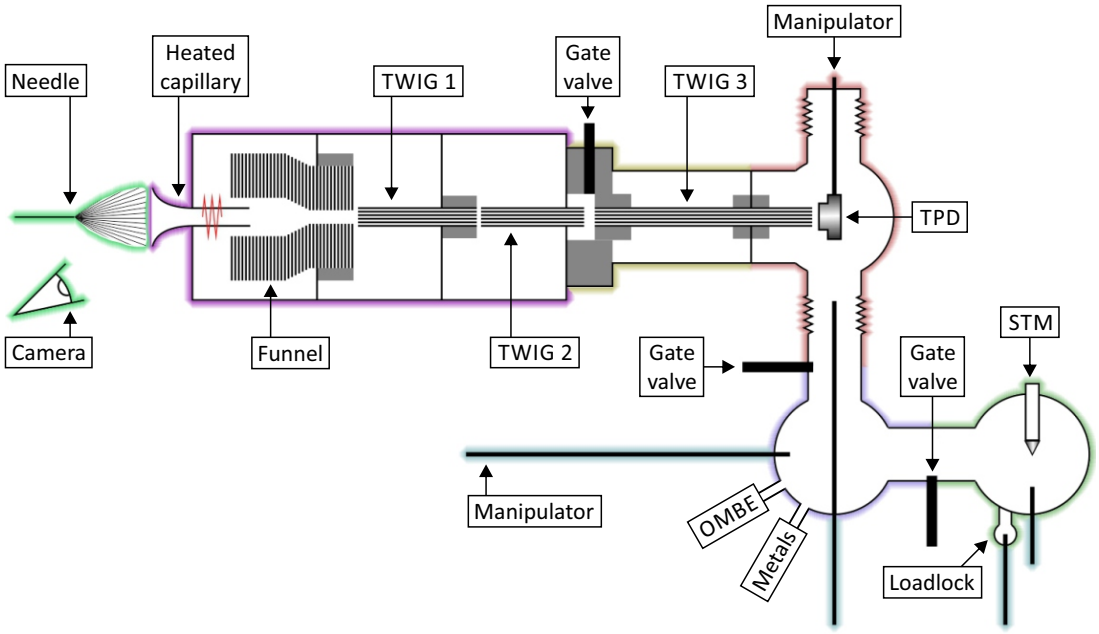

Figure 4.2: Schematic top view inside the combined ESIBD and STM setup, color coded similar to figure 4.1.

A schematic look inside the setup can be taken with figure 4.2, which is color-coded in a similar way to figure 4.1. It shows a top view with the beam traveling from left to right. Thus, the source can be seen on the left edge, followed by the API and aluminum box. The first differential chamber contains an ion funnel to focus the ions exiting the API's heated capillary and transfer them into the second chamber (see section 4.4.2). From there, they are transmitted into the third chamber by a 16-pole thin wire ion guide (TWIG, see section 4.4.3). Both the funnel as well as the first TWIG represent a direct connection between their respective entry and exit chambers such that ion guidance is not broken at any of the orifices. A second TWIG, which is fully located in

chamber 3, then transmits them right up to the gate valve. With a thickness of 4 mm the gate valve represents the largest gap in this ion guidance system where usually great care is taken to position the ion guides as close to each other as possible to minimize losses. Right after the gate valve a third TWIG takes up the ions and, again spanning over two different vacuum stages, directly transmits them to the preparation chamber. There, the sample mounting stage can be moved close to this TWIG's exit for sample preparation.

As mentioned before, after a completed preparation the sample can be transferred to the STM setup for measurement. The ESI preparation chamber does, however, provide the further analytical capability of temperature programmed desorption (TPD) measurements (see section 4.6). This is implemented through temperature-controlled heating of the sample via an electron beam while at the same time measuring partial pressure of molecular fragments in the chamber with a built-in quadrupole mass spectrometer (QMS). If and when the sample is transferred to the STM setup further preparative steps can be conducted in the preparation chamber there, which hosts a metal evaporator and an OMBE. Finally, samples can be removed from and brought into the system via a loadlock directly connected to the STM measurement chamber.

4.2 ESI Source

The first and certainly most crucial part of an ESIBD setup is the electrospray ionization source itself. For its basic working principle see section 2.3. Within the framework of this thesis two different spraying methods were investigated. At first, an attempt was made to place the needle in a low vacuum environment in order to obtain higher ion beam currents, a procedure already known from literature [266, 267]. Now, however, spraying at atmospheric pressure is employed, as this first approach was met by a number of challenges, which, in combination, proved to be insurmountable. Both methods will be discussed in detail within this section. As mentioned in section 2.3.1, ion generation through ESI is possible either in positive or negative spray mode, generating ions charged correspondingly. During this thesis only positive mode ESI was used.

4.2.1 Spraying in Low Vacuum

The advantages of spraying in sub-ambient pressure conditions are manifold making this spray method, at least in theory, vastly superior to spraying at atmospheric pressure. First and foremost, much higher ion currents can be achieved because a setup like this obviously eschews the need for an atmospheric pressure interface. These usually consist

of long, heated capillaries (see next subsection), which incur heavy transmission losses right at the very onset of the ion beam [268]. Ion generation itself is more efficient because droplets shrink more rapidly as they are both generally smaller in size and evaporation is enhanced by the reduced background pressure. Also, a smaller spray plume is formed, which can be sampled more extensively by a subsequent skimmer [269]. In order to test the feasibility of sub-ambient electrospraying a first setup of such a type was investigated in this thesis.

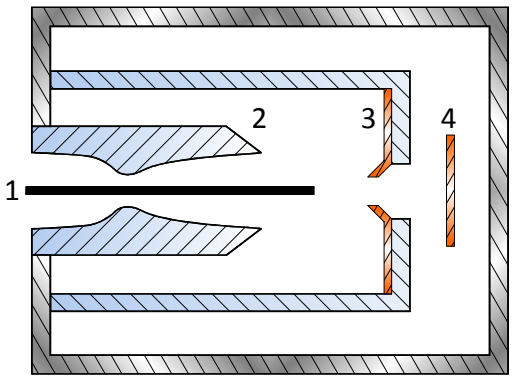

Figure 4.3: Schematic (not to scale) view of the supersonic expansion sheath ESI setup: 1 - needle, 2 - de Laval nozzle, 3 - skimmer, 4 - detector plate.

A sketch of the low vacuum spray setup is shown in figure 4.3 with the metallic outline depicting the first compartment of the aluminum chamber, which is closed using a Plexiglas lid, allowing observation during experiments from outside. Within it, a small Plexiglas box is mounted using one of the side flanges, which contains the actual ESI source. The needle (1) is supplied from the outside with feed material and connected to a HV source through a metallic connector described in the next subsection. Furthermore, it is surrounded by a convergent-divergent nozzle (2, more commonly known as a de Laval nozzle) made from Plexiglas as well such that the needle can be observed during spraying. Through this nozzle surrounding air is sucked into the Plexiglas box forming a coaxial sheath of gas around the needle. Due to the nozzle's shape the gas is accelerated to supersonic speeds in an area starting at the nozzle's neck and ending a few cm downstream, the so-called Mach cone. The idea behind using such a nozzle is that the supersonically expanded sheath gas guides the electrosprayed droplets from the needle through a subsequent skimmer (3), which must be located within the Mach cone, and into the next chamber. The skimmer plays a double role as counter electrode to the needle and is commonly held at a few hundred volts. After the skimmer a metallic plate (4) is located, which, connected to ground or a DC voltage source via an amperemeter, acts as a detector to measure the resulting beam current. Needle and skimmer currents can be measured in a similar fashion.

The only chamber pumped in this setup is the aluminum compartment housing the detector plate and Plexiglas box. A base pressure of $\sim$ 2 mbar is reached here through the use of a 500 m^3/h roots pump supported by a 125 m^3/h scroll pump. The pressure inside the Plexiglas box is simply controlled by a throttle valve reducing the amount of air flowing through the de Laval nozzle and usually kept at $\sim$ 80 mbar. Common problems in the day to day use of this setup arise mainly due to the materials used. The Plexiglas boxes will frequently crack, presumably due to corrosion from sprayed solvents, as this happens even though tempered Plexiglas is used at only $\sim$ 80 mbar of total pressure difference. Threaded holes drilled into the material to mount smaller parts easily induce cracks if screws are not being tightened very carefully. Furthermore, excessive use of plastics in general near ion beams can lead to charging and thus detrimental influences on ion generation and/or beam control (see below as well as subsection 4.4.3). In this case a quick work-around is to use fine grid wire mesh to dissipate charge before it can accumulate. A further source of complications is introduced through the method of feedstock supply utilized in this case. The spray solution can, in theory, be easily supplied to the needle using the setup's inherent pressure difference between outside and Plexiglas box. However, applying the full 900 mbar or so overpressure to the feedstock reservoir would result in a liquid flow much too high for stable spray modes, making pressure reduction through a throttle valve necessary. Both the Plexiglas box pressure as well as the overpressure applied to the feedstock can be directly measured via differential membrane pressure gauges. 80 mbar of box pressure is found to be a lower limit as otherwise feedstock liquid may start to evaporate within the reservoir and feed tube. This will then either lead to contamination within tubes leading to the pressure gauges due to intense boiling in the reservoir or trapping of minute bubbles in the capillary tube connecting the reservoir to the needle. Bubbles transported to the needle will then result in very unstable spraying conditions. Furthermore, prohibitive circumstances can arise from liquid freezing upon exiting from the needle due to the sheath gas being rapidly cooled by the supersonic expansion induced through nozzle and pressure differences. This has even been observed as a continuous icicle forming a connection from the needle all the way downstream to the detector plate. Freezing can be somewhat mitigated by heating the sheath gas upstream of the nozzle using resistively heated copper tubing.

By and large, however, this method's greatest potential pitfall lies in the generation of gas discharge phenomena within the low vacuum environment. This is due to the reduced background pressure, which lowers the breakdown voltage needed to ignite a gas discharge, as correlated via Paschen's law (see figure 4.4a) [270]. A minimum breakdown voltage exists at a certain product of pressure and electrode distance $p \cdot d$,

which for air is in the range of ∼300 V at $p \cdot d \approx 5\,\mathrm{mbar} \cdot \mathrm{mm}$ [271]. As Paschen's curves rise relatively flat from this minimum on towards higher values of $p \cdot d$ and electrode voltages of several hundred volts are common in ESI, discharge phenomena in a setup such as the one described here are a possibility to reckon with. Discharge types observed are, from least to most common: corona discharges at the needle tip (although these do not directly result in breakdown of the voltage), arcing, or glow discharges across the chamber. The latter are usually not visible to the naked eye at these pressures and have to be identified indirectly. Their generation, however, is much facilitated in such a setup, because the breakdown condition $p \cdot d$ can be satisfied by an arbitrary number of possible distances between the high voltage electrode and any grounded surface within the chamber. Arcing is seen more seldom as the currents needed are almost never reached. All types have a potentially detrimental effect in common, which is the fragmentation of molecular ions.

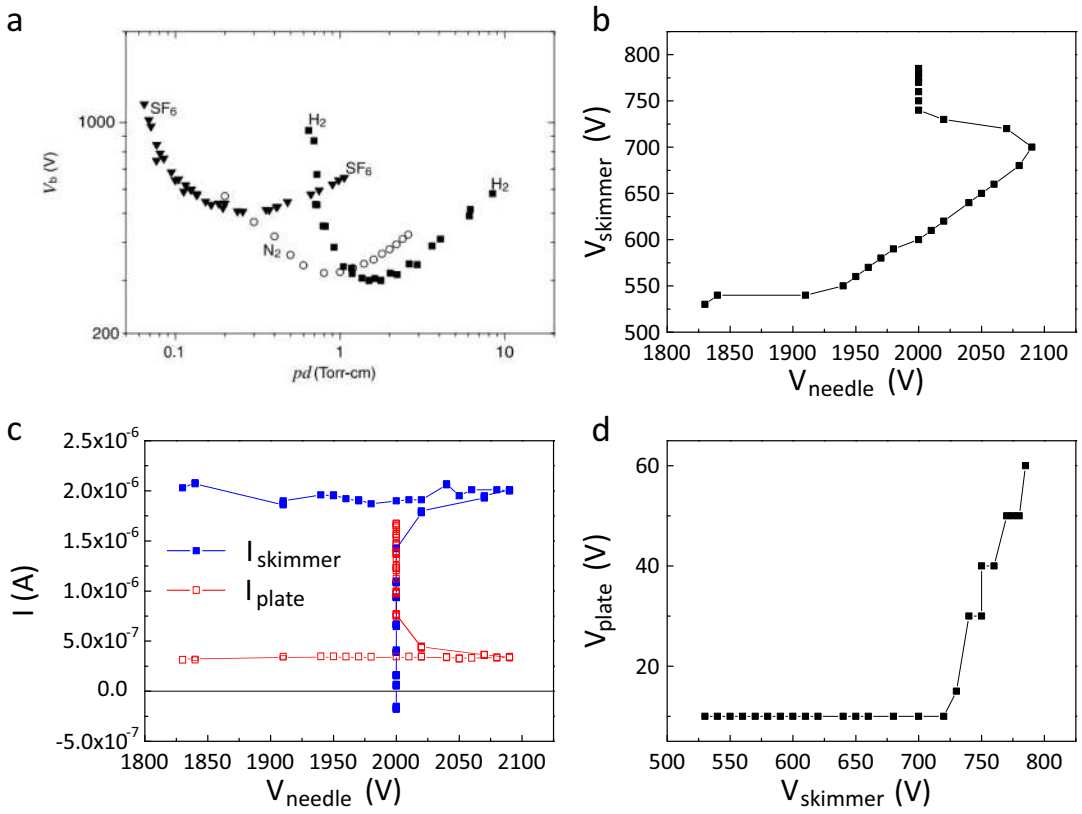

Figure 4.4: Glow discharge in a low vacuum, supersonic expansion sheath ESI setup. **a** - Paschen curves for different molecular gases. From [270]. **b** - Dependence of skimmer voltage on needle voltage showing a characteristic glow discharge behavior. **c** - Skimmer and detector plate current dependence on needle voltage. **d** - Plate voltage rising after glow discharge ignition.

Figures 4.4b through d show the characteristic behavior generated by glow discharge in the described supersonic expansion sheath ESI setup. In this experiment, needle and skimmer voltage were increased in parallel such that the current measured on the detector plate was kept constant. At a certain skimmer potential of ∼700 V breakdown is reached and a glow discharge is ignited. The plate current skyrockets as is typical for such a phenomenon. Interestingly, the skimmer current can be seen plummeting at the same moment. We attribute this effect to the circumstance that the discharge somehow seems to extend over two different pressure regions. This assumption is supported by the fact that it's actually the needle voltage breaking down, not the skimmer voltage. Presumably, the breakdown threshold $p \cdot d$ will initially be reached between skimmer and detector plate, as needle and skimmer are too far apart, even at such high needle voltages, for a glow discharge to occur there. Still, some kind of "spooky action at a distance" is at work, electrically connecting the two. The high ion current flowing from needle to skimmer is, of course, the most probable candidate although the supersonic sheath gas should prohibit any such influence acting against the flow direction. In any case, the measured skimmer current now not only consists of the impinging ions, but is actually the net difference between them and the discharge current flowing to the detector plate. It is thus now more or less an arbitrary number, which also explains how negative values are possible. As an aside: the high voltage power supplies used in this experiment are quite susceptible to high loads such as glow discharge currents, for example. This is manifested in the plate voltage, which was actually kept nominally constant, but can be seen rising after ignition occurs.

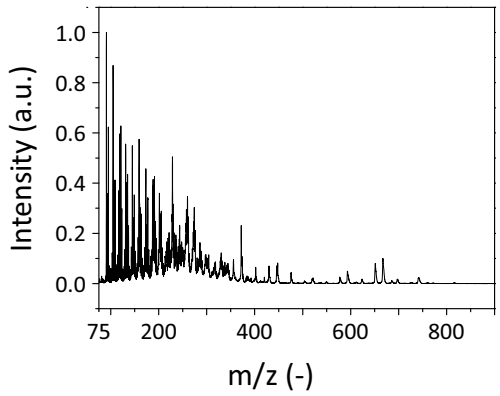

Figure 4.5: Mass spectrum of rhodamine B electrosprayed using the supersonic expansion sheath source in an ESIBD setup at the Max Planck institute for solid state research in Stuttgart [272].

In an early attempt to better characterize the supersonic expansion sheath ESI source it was taken to an existing ESIBD setup in Stuttgart and mounted there. Rho-

damine B was electrosprayed and a mass spectrum of the resulting ion beam taken with an integrated TOF-MS analyzer (see figure 4.5). This shows quite efficient fragmentation of the ion beam with only a very low intensity molecule peak (at m/z = 444) still visible. As much as this may be desired in analytical chemistry it has to be avoided at all cost in a preparative ESIBD setup. Due to the narrow window of discharge-free spraying, as well as all the other minor disadvantages of the system mentioned above, the decision was made to postpone investigations of this avenue in favor of the more controllable ambient pressure mode.

4.2.2 Spraying at Atmospheric Pressure

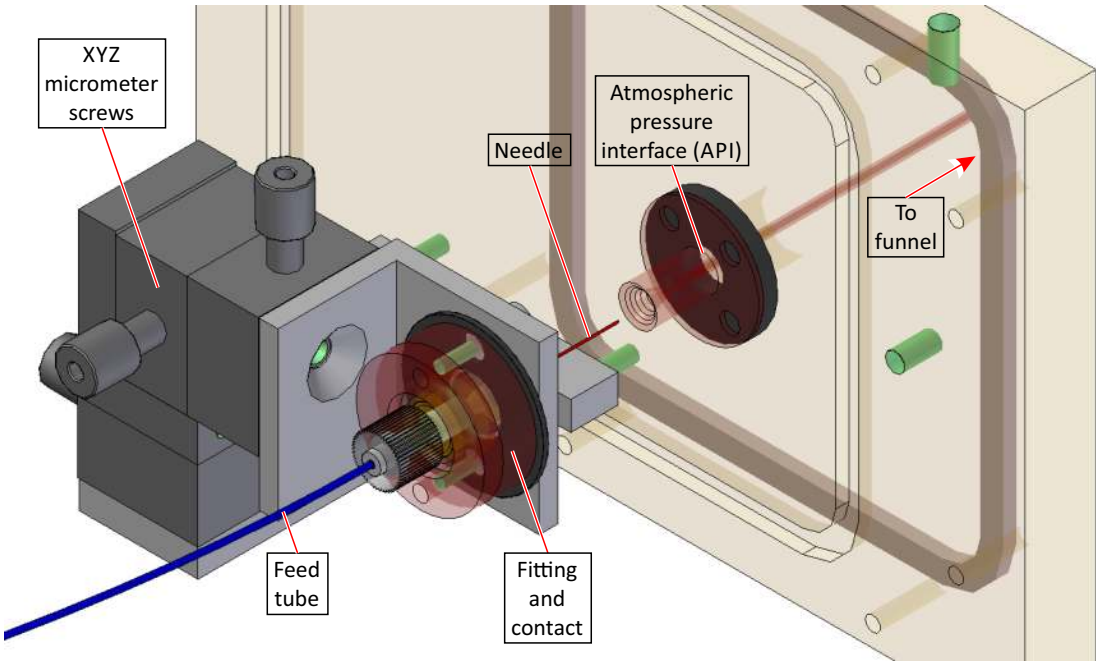

Figure 4.6: Ambient pressure ESI source currently in use in schematic isometric view.

The currently used ESI source can be seen in figure 4.6. Not shown is the syringe pump used to drive a Hamilton micro-syringe, thereby supplying the needle with spraying solution through the feed tube. Typical pumping speeds are in the range of $\sim 20\,\mu$l/h. All liquid containing parts are tightly interlocked using IDEX Health & Science *MicroTight* fittings. For precise positioning of the needle a set of micrometer screws is used as a mounting stage, while the needle position itself can be monitored via a camera. Both metallic as well as glass capillary needles are usable, usually with inner diameters of 10-100 μm. To reduce vibration of the rather flimsy needles plastic sleeves are used to sheathe them, thereby adding some rigidity. Connection of the needle to the high voltage source is implemented through a metallic fitting between feed tube

and needle. Here, electrical contact can be established independently of needle material as the spraying solution is in direct contact with the connector. Due to the solution's limited conductivity, however, this leads to a significant potential drop between connector and glass needle tip. Thus, higher needle potentials have to be used for spraying in this case, which are usually in the range of ∼4 kV for glass and ∼2 kV for metallic needles. Above these values voltage breakdown through arcing to the atmospheric pressure interface (API) or sliding discharge across the anodized micrometer screws occurs. Connector and mounting stage are electrically disconnected by a 5 mm thick PTFE washer.

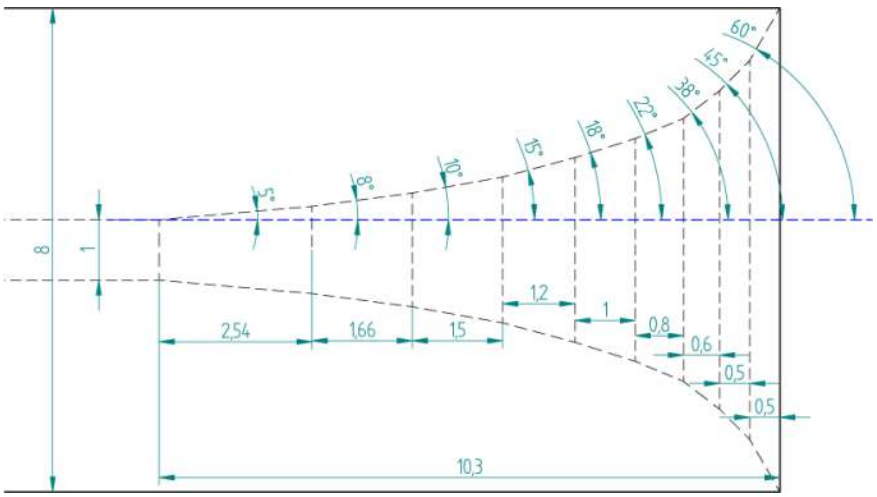

Figure 4.7: Profile of the atmospheric pressure interface showing the curvature approximated by linear segments. From [109] with modifications.

The API is made of brass and custom machined to obtain a gently curved inside (see figure 4.7), as Pauly et al. have found that this greatly increases transmission efficiency compared to a flat inlet [273]. The working hypothesis is, that an unbroken, hydrodynamic flow of background gas along this curved line keeps ions from impinging on the API surface. Pauly et al. achieved some 10 nA transmitted current with their prototype, which could be reproduced with the API described here when using solutions of similar analyte concentration. A straight cylindrical tube of 1 mm inner diameter and 60 mm length directly follows the curved section. This "inlet capillary" reduces gas flow into the first vacuum chamber, although the diameter is somewhat larger than standard API's found in literature [274, 275]. Furthermore, it can be heated from inside the chamber by a series of heating resistors, which are usually regulated such that a temperature of ∼200°C is reached towards the back end of the capillary. This provides additional heat needed for the evaporation of solvent, which is a crucial part in ion generation, and can thus increase transmitted ion currents by a factor of 2 in this setup.

However, due to the large inflow of cold air the API's front end is merely warm to the touch [276].

The final installation is a Faraday cage surrounding both mounting stage and API to protect users from accidental electrocution. Micrometer screws can still be actuated through long plastic extensions. The syringe pump is caged, too, because liquids of very high conductance could potentially lead to electrocution hazards there as well. It has been found that irregular airflow from the nearby located pump motors can negatively influence long-time stability of the spray. The Faraday cage surrounding needle and API is thus usually wrapped in aluminum foil to provide a more controllable spraying environment. Finally, Faraday cage, micrometer screws (and thereby the needle) as well as the API are all mounted on a single flange, custom-made to fit the aluminum chamber. Removal for maintenance or necessary rearrangements is thus facilitated.

4.3 Differential Pumping

One of the main challenges in operating an ESIBD system is to efficiently process the gas load introduced into the system through the API, which naturally represents a kind of controlled leak. This is usually achieved through a series of subsequent chambers, each with its own pump, connected by different interfaces. For experiments conducted under UHV conditions, a pressure reduction of 12 to 13 orders of magnitude is necessary. Designing such a differential pumping system involves careful consideration of a multitude of factors, such as pumping speeds, pump hookup, orifice leak rates and so on. In this section a comparison of theoretically possible pressure levels to the setup developed during this thesis will be made. Due to the range of different pressure regimes involved in differential pumping, theoretical calculations rely both on fluid dynamics and the kinetic theory of gases. Derivations of most of the formulas used here can be found in standard textbooks [277, 278].

4.3.1 Attainable Pressures

Starting at atmospheric pressure and commencing all the way to ultrahigh vacuum, the residual gas flow in ESIBD goes through all regimes, from continuum, via Knudsen (also called transient), to molecular flow. These regimes are characterized by comparing the mean free path λ of a gas to a representative length d of the investigated system, giving the so-called Knudsen number:

$$Kn = \frac{\lambda}{d} \tag{4.1}$$

In gas flow problems d is usually the length of some confinement, which, in all cases during this discourse, will be the diameter of an orifice. Molecular flow is given in systems with Kn greater than unity, continuum flow if $Kn < 10^{-2}$, and Knudsen flow in between those two limits. With orifice diameters in the mm range molecular flow through them is obtained at or below 0.1 mbar, where the mean free path is $\sim 10\mu$m. Likewise, continuum flow is given at pressures above 10 mbar. Of vital importance for the question whether or not a certain chamber pressure can be obtained is the pump throughput Q_{pump}, which is the product of pumping speed S and chamber pressure p.

$$Q_{pump} = p \cdot S \tag{4.2}$$

Another fundamental relationship is that between leak rate C of an orifice and flow rate $Q_{orifice}$ through it:

$$Q_{orifice} = \Delta p \cdot C \tag{4.3}$$

where Δp is the difference in pressure at both sides of the orifice. Both Q-quantities have the dimension of an energy flow and will be calculated in $\frac{\text{mbar}\cdot\text{l}}{\text{s}}$ throughout this thesis. As mass conservation dictates that $Q_{pump} = Q_{orifice}$, the obtainable chamber base pressure depends only on orifice leak rate and possible pumping speed, both of which can, in turn, be dependent on pressure. In principle, gas flow into the subsequent chamber would have to be subtracted from the inflow, but it is usually several orders of magnitude smaller and can thus be neglected.

Pumping speed depending on intake pressure can be calculated for ideal pumps, but several factors complicate calculations for real ones. This is, however, usually measured by the manufacturer during development of a pump and necessary values can thus be obtained from diagrams and tables. Due to both S and C being dependent on chamber pressure, the design of differentially pumped systems is an inherently implicit problem, which can make computational simulations necessary [279]. In our case, we will work with the basic assumption that pumping speeds of ~ 100 l/s are possible in low and medium vacuum stages, whereas several hundred l/s can be reached in high and ultrahigh vacuum stages where turbomolecular pumps can be used. This leaves us with the sole task of calculating orifice leak rates, which utilizes different formulas depending on the flow regime. As all interfaces investigated within this work basically take the form of long tubes, we will only use formulas for this class of orifice. A comparison of leak rates of the presently used tubular interfaces to thin apertures has been given in [109].

At the API (which we will call interface 1, for easier comparison with subsequent interfaces) continuous flow predominates, but the pressure difference between laboratory

environment and first chamber is usually so large that so-called choked flow occurs. This circumstance arises in continuous flow settings if the ratio of pressures after and before an orifice p_1/p_0 rises above a certain threshold. As per equation (4.3), the flow rate and thus gas speed initially rise with pressure difference, but at the aforementioned threshold the gas will be accelerated to sonic speeds at which point a further increase of gas flow is impossible. For dry air, this threshold ratio is ~ 0.48, thus choked flow in interface 1 already arises at chamber pressures of 480 mbar and below, which is still a very high value. Due to the gas traveling at sonic speed (Mach 1) the pressure at the interface's low pressure side will be equal to exactly this value. Only after expansion into the surrounding chamber will the actual base pressure be reached. In low vacuum environments this attenuation is usually accomplished within a few cm [280]. On the other hand, this makes calculating the orifice gas flow easier, as the chamber pressure does not have to be known. Reasonably correct calculations are, however, complicated by the fact that flows at the speed of sound through such small orifices are usually turbulent in nature. This is characterized in fluid mechanics by the so-called Reynolds number:

$$Re = \frac{v \cdot d}{\nu} \tag{4.4}$$

which compares a characteristic dimension d (here the orifice diameter) to the flow speed v and kinematic viscosity ν of the fluid. Above a critical value of $Re \approx 2300$ turbulent flow becomes increasingly likely. As Reynolds numbers of several tens of thousands can easily be reached in APIs ($\sim$26000 for a 1 mm diameter API) one has to make use of the following formula to calculate C [278]:

$$C_{turbulent} = 1.015 \cdot d^{19/7} \left(\frac{\bar{c}^6}{\eta}\right)^{1/7} \cdot \left(\frac{p_0 + p_1}{l}\right)^{4/7} \cdot (p_0 - p_1)^{-3/7} \tag{4.5}$$

where d and l are the interface's diameter and length, respectively, $\bar{c}$ is the gas's mean thermal velocity (463 m/s for dry air at 20°C) and η its dynamic viscosity ($18.2{\cdot}10^{-6}$ Pas).

For an API of 1 mm in diameter and 60 mm in length, such as the one used in this thesis, equation (4.5) yields leak rates of $\sim$ 0.3 l/s. Combined with a maximum pressure difference of 520 mbar limited by choked flow this leads to a flow rate of around 150 $\frac{\text{mbar}\cdot\text{l}}{\text{s}}$. Compared to the aforementioned pumping speeds of $\sim$100 l/s we arrive at obtainable pressures in the single digit mbar regime for the first vacuum chamber, thus already gaining three of the 13 orders of magnitude needed. It is also worth noting that continuum dynamics allows us to calculate the Mach number M_i at the interface inlet via [281]:

$$f \cdot \frac{l}{2d} = 1/2 \left(\frac{1}{M_i^2} - 1\right) + \ln(M_i) \tag{4.6}$$

wherein f is a friction factor depending on Reynolds number and surface roughness of the interface, calculated to be 0.04 in this case (equation (5) in [282]). This gives an inlet speed of $M_i \approx 0.5$, which underlines and corroborates the flow field effect mentioned in section 4.2.2.

A chamber pressure in the low mbar range still puts interface 2 (between chambers 1 and 2) well into the continuous flow regime. Here, the actual orifice consists of a series of stacked ring electrodes of an ion funnel (see section 4.4.2) such that a channel of 1.7 mm in diameter and of $\sim$ 10 mm length is formed. As the flow is again choked, we can still use equation (4.5) to calculate the leak rate, which is now around 1.3 l/s. This increase by a factor of $\sim$4 with regard to the first interface would theoretically in turn also lead to a reduction of the pressure gradient by a similar factor. However, this interface is much rougher than the API's smooth capillary, which increases the orifice's flow resistance. Thus, equation (4.5) has a limited accuracy in this case and we will see in the following subsection that in reality better leak rates are achieved. A pressure gradient on the order of $\sim 10^{-2}$ should be obtainable with such an interface in any case. This leads to base pressures around 10^{-2} mbar in the second chamber, thus very conveniently bypassing the Knudsen flow regime, which would necessitate more complicated mathematics to calculate C. Even within interface 2 no Knudsen flow is present, because the choked flow leads to exit pressures of the same magnitude as the intake pressure. One is thus able to gain another two orders of magnitude at this stage.

From chamber 2 on we can thus use the following, much easier formula to calculate leak rates in the molecular flow regime [278]:

$$C_{molecular} = 12.1 \cdot 10^4 \cdot \frac{d^3}{l} \tag{4.7}$$

Wires used to construct the TWIGs connecting these chambers have to fit through these orifices alongside the ion beam, however. This makes an inner diameter of at least 3 mm necessary (see section 4.4.3). The interfaces have typical lengths of 50 to 100 mm. This yields theoretical leak rates in the range of 0.01 l/s, which would result in pressure gradients of $\sim 10^{-4}$ or even lower using turbomolecular pumps with pumping speeds of several 100 l/s. Only two further interfaces and pumps operating in the molecular flow regime are thus necessary to reach UHV conditions.

It is worth mentioning, however, that no matter the speed of the installed pumps a small fraction of the residual gas exiting interface 2 will be transmitted all the way to the last UHV chamber of the system as a molecular beam, since the molecular flow regime is given from chamber 2 on. This fraction is proportional to $\Delta\Omega/\pi$, where $\Delta\Omega$ is the solid angle of the last chamber interface as seen by the molecules exiting interface 2

[283]. Thus, the further away the two interfaces, the smaller the fraction of residual gas transmitted as a beam will be. This results in a minimum length L_{min} of the system from this point on:

$$L_{min} \geq \frac{d_x}{2} \cdot \sqrt{\frac{C_2}{S_x}\frac{p_2}{p_x}} \tag{4.8}$$

with the last interface diameter d_x, interface leak rate C_2 and base pressure p_2 of chamber 2, and pumping speed S_x and base pressure p_x of the UHV chamber. Considering the parameters of chamber 2 discussed above, a pumping speed of 400 l/s in the last UHV chamber, a desired base pressure of 10^{-10} mbar there, and an orifice of 7 mm in diameter (see next subsection) we arrive at a necessary length of $\sim$ 1600 mm. Fortunately, this can be avoided by controlled misalignment of the ion guides such that no direct path is given for a molecular beam to traverse the whole length. Exit and inlet of subsequent ion guides are thus slightly tilted with respect to each other, a fact, which apparently does not significantly reduce ion transmission (see section 4.4).

4.3.2 The Current Solution

Figure 4.8 shows a schematic layout of the differential pumping system in its latest state. Differential chambers 1 and 2 are pumped by Pfeiffer WKP roots pumps with nominal pumping speeds of 500 and 250 m^3/h ($\sim$ 140 and 70 l/s), respectively. Both are backed by two Edwards XDS35i scroll pumps, one of which also acts as the forepump for the 600 l/s Oerlikon Mag W turbomolecular pump installed below differential chamber 3. Finally, the last differential as well as the ESIBD preparation chamber are pumped by two turbomolecular pumps of the same design, but with 400 l/s pumping speed, both of which are connected to the extensive UHV forepump system. This also provides roughing pressure for the STM preparation chamber turbo and consists of two parallel, small turbomolecular pumps (an Oerlikon Mag W with 80 l/s closer to the ESIBD side and a Pfeiffer 50 l/s at the STM side) with separate Edwards rotary vane forepumps ($\sim$ 1.4 and 2.2 l/s, respectively). The redundancy here once again enables quick and easy separation of the two systems for maintenance and modifications. Several valves in addition to the ones necessary for just this separation procedure (mentioned in section 4.1) are installed. The manually operated bypass connecting differential chambers 1 to 3 acts as a pressure relief during the initial start-up procedure while pumping down from atmospheric pressure. Here, large absolute pressure differences can occur, which can lead to damaging of fragile ion funnel and TWIG parts as well as degradation, over time, of the sealant used at the separating walls. Once chamber pressures are in the mbar range, this bypass is closed. Vice versa, it has to be opened again during the

venting procedure. Several valves connected to atmosphere facilitate a faster venting process. All pneumatically and magnetically operated valves, except the one used to separate differential chambers 3 and 4, are hooked up to separate safety switches, which are wired to shut in case of an electrical blackout. The UHV forepump system also provides pre- and bakeout vacuum for all functional parts connected to the STM such as the loadlock, OMBE, metal evaporators and so on.

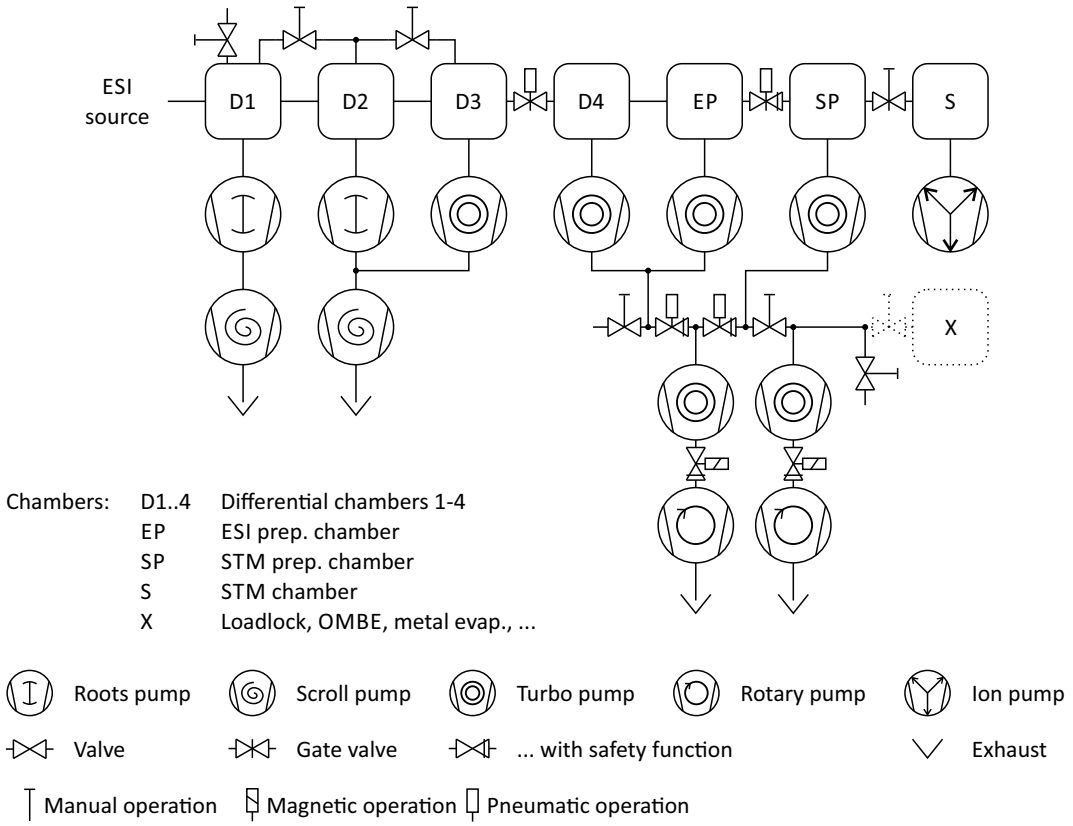

Figure 4.8: Schematic overview of the differential pumping system developed during this thesis. Dotted outlines mark multiples of possible further parts.

Chamber pressures in the ESIBD system are measured using two different types of gauges. For differential chambers 1 and 2 Oerlikon Leybold CERAVAC CTR 100 capacitive membrane gauges are used. Data from these are collected via RS232 and processed by the control system (see section 4.5). At all other stages Oerlikon Leybold IONIVAC ITR 90 combination gauges are in operation. These feature a Pirani cell for pressures above $2.4 \cdot 10^{-2}$ mbar and a Bayard Alpert hot cathode cell for lower pressures down to a limit of $5 \cdot 10^{-10}$ mbar. They are hooked up to a PROFIBUS field bus which also connects to all Mag W turbomolecular pumps via Mag.Drive iS control units and is likewise read and processed by the control system.

Pressures obtained with this system are summarized in table 4.1, along with the corresponding actual and theoretically reachable inflow leak rates C and C_{theo}, respectively. Reasonable agreement with output of the theoretical formulas discussed in the previous section is found for the first three differentially pumped chambers. The API's upward deviation from the theoretical value may well be due to the fact that the first chamber's roots pump is hooked up to it via a ∼300 mm long section of vacuum tubing. The chamber pressure is thus presumably higher than the pump intake pressure, which in turn would decrease the pump throughput compared to the nominal one calculated by using the chamber pressure. Correspondingly, this would mean a lower leak rate than the one given in table 4.1. The same is true for chamber 2, although here the obtained leak rate is actually lower than the theoretically calculated one. We attribute this to the significant surface roughness of the ion funnel interface, which leads to a profound increase in flow resistance. This offsets the aforementioned effect of nominal pump throughput even below the theoretical value.

Table 4.1: Chamber pressures, pumping speeds, and corresponding leak rates.

Chamber	Pressure (mbar)	S (l/s)	C (l/s)	C_{theo} (l/s)
Diff. 1	1.7	140	0.5	0.3
Diff. 2	$2.5{\cdot}10^{-2}$	70	1	1.3
Diff. 3	$2{\cdot}10^{-6}$	600	0.05	0.065
Diff. 4	$1{\cdot}10^{-8}$	400	2	0.3
ESIBD prep.	$<5{\cdot}10^{-10}$	400	-	0.6

For chamber 3, which is separated from chamber 2 by a 80x3.5 mm tube, we find a remarkable agreement between theory and reality. However, chamber 4 seems, at first glance, to exhibit a flaw in either system setup or calculation. The value obtained for C_{theo} assumes a tubular orifice of 6.5 mm in diameter and 110 mm in length. As mentioned, this large inner diameter becomes necessary due to the TWIG wires (see also section 4.4.3). However, equation (4.8) now comes into play as the length from chamber 2 to the end of this orifice approaches L_{min}. A precise calculation of this length is complicated, as its exact starting point depends on the length of the gas expansion zone behind the ion funnel, from which on truly molecular flow is given. It is presumed, however, that the pressure in chamber 4 could be much improved (and thus maybe chamber 4 even omitted) by implementing a bend in the optical axis before the UHV chambers of the system (as mentioned in the previous section). Finally, the ESIBD preparation chamber's leak rate can not be compared to its theoretical value as the pressure gauge installed there bottoms out at $5{\cdot}10^{-10}$ mbar. However, with the

theoretical leak rate (for a 70x7 mm tube) and the given pumping speed a base pressure of $1.5{\cdot}10^{-11}$ mbar should be obtainable. This, of course, is a pressure range which is only reachable under ideal bakeout and operating conditions and presumably not given with this relatively new setup.

4.4 Ion Guidance Systems

At its heart ESIBD is very close to classical separation techniques insofar as the ion beam has to be efficiently separated from the neutral background gas flow. The problem is being complicated by the fact that ion beams will tend to diverge because of internal Coulomb repulsion. Just a set of subsequent, differentially pumped chambers separated by skimmers or other orifices is thus not a sufficient solution, as this would result in immense ion losses and only a minute amount would actually be deposited onto a sample, if any. Furthermore, such a setup would make removal of contaminants from the beam impossible, which would then be co-deposited, thus further decreasing the actual analyte coverage. Hence, differentially pumped chambers have to be functionalized with ion guidance systems, which focus the beam and transmit it from chamber to chamber, and allow for a certain refinement of the beam. Two such systems, the ion funnel and the thin wire ion guide, have been investigated and improved upon during this thesis. Some prior studies on the devices discussed in this section can be found in [109, 159, 178, 261].

4.4.1 Relations derived from Simulations

As mentioned in section 2.4 the movement of ions through RF-driven ion guides can be a complex matter, depending on a multitude of different parameters and dimensions. In order to better gauge design restrictions it is thus convenient to simulate this behavior before actually building a new ion guidance system. So far, in every RF-driven ion guide a resonant behavior has been found, due to which at a certain RF frequency a maximum amount of ion beam current can be transmitted. We will show here that understanding this phenomenon and developing a model to describe it are key steps for deriving estimates of crucial design parameters.

Figure 4.9 shows snapshots taken during SIMION simulations of ion trajectories in a 16-pole thin wire ion guide. Even at a quick glance it becomes apparent that ions accumulate close to the electrodes rather than being randomly dispersed all over the ion guide's internal area. This is a clear indication of space charge induced Coulomb repulsion, which, together with the electrodes' repulsive potential, leads to this ring-like charge distribution. Furthermore, a frequency dependent oscillation behavior of the

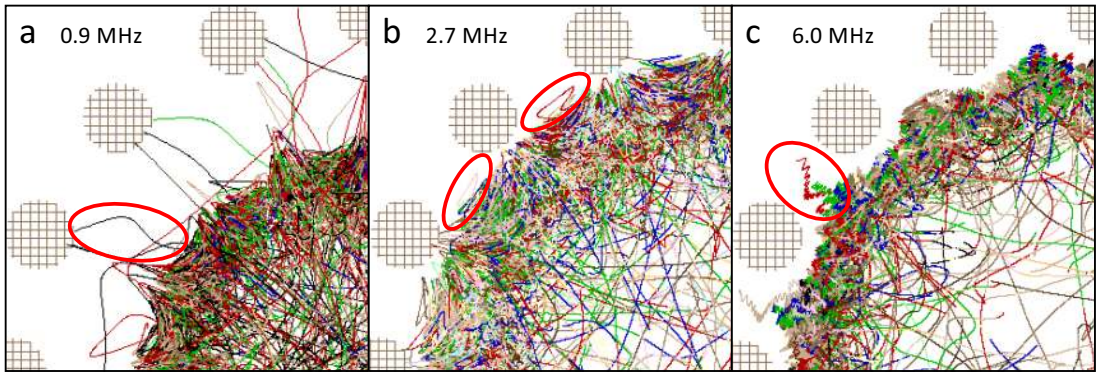

Figure 4.9: SIMION simulations highlighting resonance behavior in a 16-pole thin wire ion guide. Parameters: $R = 1.5$ mm, $d = 0.32$ mm, $V_{RF} = 50$ V, $p = 0.1$ mbar, $m = 5000$ amu, $q = +5$ e, $t = 1000$ µs. Values for Ω are given in the subfigures.

ions can be observed (marked by red ellipses). At low frequencies (panel a), the RF potential's attractive half period is so long that some ions are accelerated too far and impinge on the electrodes. At the resonance frequency (2.7 MHz, panel b) a perfect oscillation between electrodes is possible without impinging. Thus, the ion cloud ring can exhibit its maximum radius. Further increasing the frequency (panel c), however, leads to very small oscillations which enable ions to be pushed out the ion guide through the gap between two electrodes by the repulsive potential.

We can model this behavior by assuming a free particle oscillation driven by an external potential. Neglecting dampening, this has a characteristic amplitude of:

$$A(\Omega) = \frac{F_0}{m \cdot \Omega^2} \tag{4.9}$$

with the maximum force F_0 of the external potential and its frequency Ω, and the particle's mass m. Close to the shortest virtual line connecting two adjacent electrodes one can approximate F_0 by comparing this region to the space within a parallel-plate capacitor:

$$F_0 = \frac{U_0 \cdot z}{d_e} \tag{4.10}$$

where U_0 is the capacitor's voltage, z the particle's charge, and d_e the inter-electrode distance. Substituting the RF-potential's amplitude V_{RF} for U_0 we can thus easily derive a dependence of the resonance frequency on some important parameters, if we assume optimal operation whenever $A(\Omega) \approx d_e$ is given (see figure 4.9b):

$$\Omega_{max} \propto \frac{1}{d_e}\sqrt{V_{RF}\frac{z}{m}} \tag{4.11}$$

In general, more charge will fit into ion guides of larger inner diameter d_i, because a larger repulsive Coulomb potential can be accommodated. Another important message

of figure 4.9 is that due to the charge's ring-like distribution this increase is linearly dependent on d_i. However, if the number of electrode pairs N is kept constant with increasing d_i also d_e will increase, leading to a shift of Ω_{max}, but more importantly also to a decrease of repulsive force at all distances from the electrodes. N should thus be increased proportionally to d_i in order to keep d_e small and constant. Furthermore, an ion guide's repulsive potential, and thereby its capability to constrain a high amount of charge, is proportional to V_{RF}^2 (equations (2.14) and (2.16)). We thus arrive at a tentative proportional relation for the maximum retainable charge of:

$$Q_{max} \propto \frac{d_i}{d_e} \cdot V_{RF}^2 \tag{4.12}$$

with $\frac{1}{d_e} \propto N$. Larger inner diameters and more electrodes are thus beneficial to the amount of charge which can be retained and transmitted by the ion guide. This, however, is in conflict with both the background gas leak rate of such a device and its constructability, respectively. Hence, a good compromise between these factors has to be reached.

4.4.2 Ion Funnel

The interface between differential chambers 1 and 2 is formed by a custom-built ion funnel which has been described in [109] and is based on an earlier prototype [159]. It represents a novel design insofar as, compared to earlier ion funnels in literature [156, 157], it not only features a gas tight section to reduce background gas leak rate, but also unbroken application of repulsive RF and cascading DC potential over its whole length (see figure 4.10).

A first section consisting of electrodes with 30 mm inner diameter facilitates trapping of ions ejected from the expansion zone at the API exit. After 96 electrodes of constant diameter this is then gradually tapered down to eventually reach an inner diameter of 1.7 mm. To accommodate for the increased trapping potential (see section 2.4.3) at these small diameters the whole device features two different spacings between the generally 0.2 mm thick electrodes. 0.4 mm spacing is used until an inner diameter of 12 mm is reached, and 0.2 mm from then on. As this results in a shift of the device's resonance condition two RF potentials of differing frequencies have to be used to drive the ion funnel. Both this RF as well as a DC potential (see below) are applied to the electrodes via connections facilitated through the use of printed circuit boards (PCBs). A series of capacitors for capacitive coupling of the RF potential as well as resistors to gradually change the DC potential are mounted on these PCBs (schematically shown on the bottom of figure 4.10).

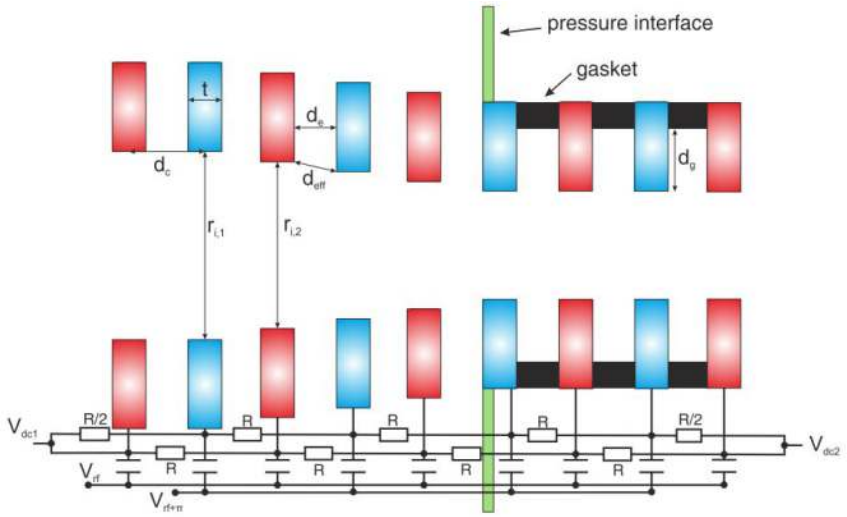

Figure 4.10: Schematic representation of the ion funnel developed during this thesis and others. From [109]

Starting at the 3 mm i.d. electrode 0.2 mm thick PE gaskets are used to make the space between electrodes gas-tight. This forms a tight channel similar to a tube, which increases flow resistance for the residual background gas and hence optimizes the leak rate into the next chamber. Due to the relatively high surface roughness of this tube induced by the stacked electrodes flow resistance is increased even further compared to a smooth tube. The 3 mm i.d. electrode is also used as the actual base plate of the device and hence features the largest outer diameter. This facilitates mounting of insulated rods to stack the electrodes on, as well as mounting of this 0.2 mm base plate to a mechanically more stable one for fixation to the chamber wall. In this way, the RF potential is not broken by the use of a thick base plate to which at best a DC potential could be applied. This is usually the case in ion funnels reported in literature. Downsides of this design are the relative mechanical frailty of this plate and the large capacity it represents compared to all other electrodes, which may deteriorate the RF signal's shape.

Two factors can decrease ion transmission at this stage. One is the trapping potential arising between electrodes, while the other is given by the relatively high background gas pressure. Short mean free paths result from this, leading to a constant redistribution of ion momenta. A pulling DC potential gradient is thus applied to the device in order to facilitate hopping transport of ions from one potential well to the next. Presumably, the gas-tight section plays a somewhat assisting role in this effort. As it already starts at an inner diameter of 3 mm it features a short funnel-like section comparable to the one exhibited by the API. Due to choked flow arising within the gas-tight section the

inflow gas speed is also increased. This should, in theory, facilitate ion transmission as it represents an additional directional effect on top of the DC potential. Further experiments with funnels of differently designed gas-tight sections have to be conducted to reach definitive conclusions about this assumption.

4.4.3 Thin Wire Ion Guides

So far, all calculations and theoretical considerations have shown that, in order to maximize the amount of charge transmitted through a multipole ion guide, its inner diameter and/or number of electrode pairs should be as big or high as possible. A large inner diameter, however, would lead to very broad ion beams, which would in turn be hard to focus for transmission into a subsequent chamber. To circumvent this problem, the so-called thin wire ion guide (TWIG) has been developed, which is a multipole ion guide consisting of wire electrodes. This facilitates increase of the number of electrodes, while keeping the inner diameter to a manageable size. Furthermore, it enables construction in such a way that wires are taut from one chamber into the next, thus featuring an unbroken restraining potential on the ion beam at the chamber interface. This class of devices has been investigated in several prior works [109, 159, 178, 262].

The current setup features a total of three 16-wire TWIGs (see also figure 4.2), the first of which is mounted directly behind the ion funnel's exit and transports the ion beam all the way into the third differential chamber. To reduce the background gas leak rate a 80x3.5 mm tube comprises the chamber interface between differential chambers 2 and 3, through which the wires are taut. These have a diameter of 0.235 mm and are mounted such that the ion guide's outer diameter amounts to 3 mm. An insulating gap of 0.25 mm between the wires and the interfacial tube is thus provided for. A second TWIG of similar design takes up the ion beam in chamber 3 and transports it right up to the gate valve separating chambers 3 and 4. It does not feature any gas-tight sections as it is mounted fully within chamber 3. Both these first two TWIGs use PCBs as mechanical fixtures to solder the wires on. These are also used for electrical connection of the two RF potentials used to drive the ion guides. The third TWIG is mounted directly behind the aforementioned gate valve and transmits the ion beam from there through chamber 4 and another interface all the way to the sample in the ESIBD preparation chamber. Its first section is a gas-tight tube of 110x6.5 mm in dimension, to decrease gas leak between chambers 3 and 4. The significantly larger inner diameter is necessary, because the beam suffers from some widening over the gap arising due to the gate valve, and the diverged beam could otherwise not be sampled

sufficiently. Still, some 50% loss occurs at this stage. Correspondingly, wires of 0.5 mm diameter have to be used to remain at a relatively constant inter-electrode distance d_e. Another gas-tight section (70x7 mm) makes up the interface between chamber 4 and the preparation chamber. As the third TWIG resides completely within the setup's UHV part the use of PCBs as mounting fixtures becomes impossible due to their high vapor pressure and increased degassing during bakeout. Only stainless steel, aluminum, and PEEK are thus used in the construction of this device and wires are held taut by screws rather than soldering [109]. Ion beam currents transmitted through these ion guides as well as the ion funnel can be measured on the subsequent device by applying a pulling DC potential to its wires and measuring the resulting current.

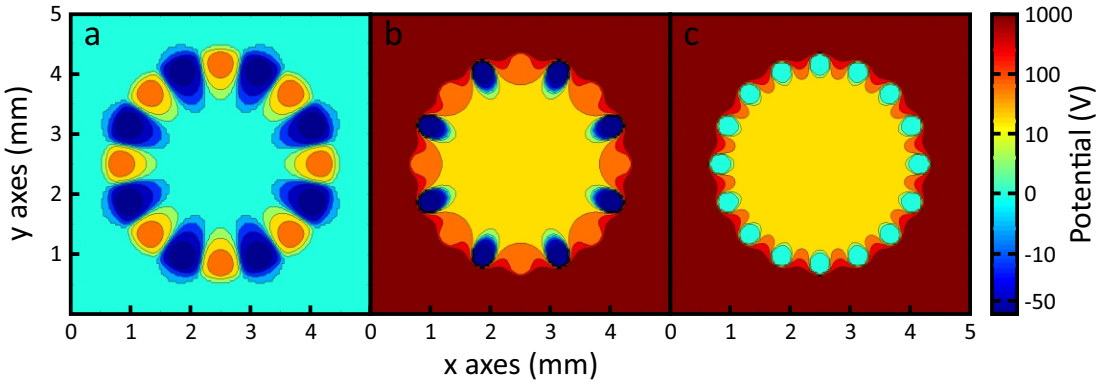

Figure 4.11: SIMION simulation results highlighting the effect of an external charge on a TWIG's internal potential landscape. **a** - No external charge applied, TWIG electrodes at opposite potential of ±50 V. **b** - +1 kV of external charge, TWIG electrodes again at opposite potential of ±50 V. **c** - +1 kV of external charge, TWIG electrodes at 0 V.

Due to the relatively short distances between the ion-beam-confining inner area of such ion guides to the vacuum chamber environment this design is prone to detrimental influences from involuntary charging. Great care thus has to be taken to remove any non-conductive surfaces from the vicinity of the wires, as can already be seen from simulation results shown in figure 4.11 (see also figure 2.13). Therein, a chargeable surface was placed around a 16-pole TWIG and the influence of the surface charge on the TWIG's internal potential landscape investigated. A charge sufficient to reach an external potential of 1 kV raises the internal potential to some 20 V, which is already more than the ions' kinetic energy, regardless of the applied electrode potential. If a transported ion beam of some nA suffers from losses on the order of a few percent (a quite reasonable amount), which impinge on such a surface, this amount of charge can easily be accumulated within just a few tens of seconds. Surfaces close to the TWIG wires are thus usually metallic. Wherever wires have to be mounted or guided, fixtures made of silicon carbide (SiC) are used. These exhibit a small conductivity on the order

of 10^{-7} S/m, such that both charging as well as parasitic currents flowing between oppositely charged wires can be effectively prevented. Furthermore, SiC exhibits a very low vapor pressure, thus making it suitable for use in the UHV chambers as well.

The resonance behavior mentioned in section 4.4.1 can be confirmed experimentally in these devices (see figure 4.12). It is shown here for beams of two different molecules, namely Rhodamine B and 2H-TPP (see also section 4.6). For an RF amplitude of 40 V_{PP} a plateau instead of a peak is observable, which means the TWIG's transmission capacity is not maxed out. This makes determination of the resonance frequency somewhat hard in this case. Both molecules, however, feature this plateau at roughly the same frequency, which is to be expected as their molecular masses don't differ much. Only at smaller values for V_{PP} can an actual resonance frequency be observed, as the TWIG's capacity is reduced and limits the amount of transmittable charge. A clear shift of the resonance towards smaller frequencies is observed, which is in good agreement with the considerations mentioned in section 4.4.1, although these measurements represent only preliminary data. Further experiments have to be conducted in order to fully quantify all relations obtained from theory.

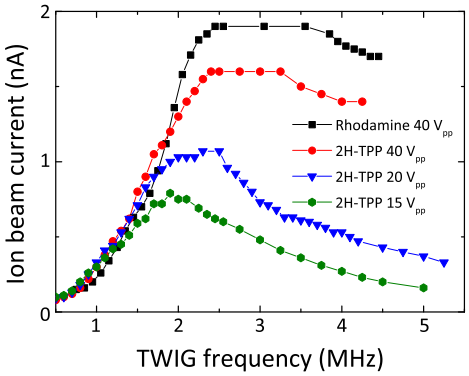

Figure 4.12: Resonance measured in a 16-pole TWIG for two different substances (Rhodamine B and 2H-TPP), and at different RF amplitudes V_{PP}.

4.5 Supply and Control

So far, a lot of the system's functionality has been discussed, but without proper power supply and control of the individual parts no actual operation can commence. Off the rack solutions to this problem are out of the question due to the setup's inherent intricacies as well as the need for flexibility during experimentation. A series of tailor-made supply and control devices have thus been developed and built during construction of the ESIBD setup, which will be discussed in the following section.

4.5.1 Radio Frequency Boosters

Every ion guidance system necessitates at least as many radio frequency power supplies (each generating two signals phase-shifted by 180°) as there are ion guides installed if complete control over their respective transmission resonances is to be achieved. In the particular case of this work's ESIBD system one more supply is needed as the ion funnel connecting chambers 1 and 2 operates at two different frequencies. From the AC point of view it can thus actually be seen as two separate devices placed at the closest possible distance to each other. To generate this many high power radio frequency signals a special type of RF amplifier or booster has been developed and several devices of its kind built. In contrast to the resonant oscillator approach introduced in section 2.4.5 here a different kind of concept was chosen. Its working principles are partly based on digital processes, which are easy to implement and control. The fact that square wave signals are amplified allows utilization of a broad frequency band through the use of TTL signal generators discussed in the following subsection. At its very core the amplified RF signal is generated by two series of MOSFETs, one n- the other p-channel, which are both connected to the outgoing line through their respective drain contacts. The n-channel MOSFET source contacts are connected to ground (VGND), while the p-channel sources are connected to a variable DC voltage (VP) generated outside the booster, which defines the resulting RF signal's amplitude. Alternately switching n- and p-channel MOSFETs on and off thus generates a square wave signal with a low state equal to VGND and a high state equal to VP. Furthermore, a DC offset can be capacitively coupled to the signal in order to raise or lower it with respect to VGND.

A schematic sketch of the booster's work flow from the incoming TTL signal all the way to the outgoing, amplified, high power square wave signal is shown in figure 4.13. Running through it from left to right the incoming TTL signal is first noise-reduced and, more importantly, shaped by a Schmitt trigger, after which it is fed into a complex programmable logic device (CPLD) as its clock signal. Very basically, a CPLD represents an array of logic circuitry (so-called macrocells) who's wiring and thereby functionality can be changed programmatically. It can thus "mimic" the behavior of an arbitrary logic circuit. In the CPLD, two working signals of halve the initial frequency are generated by a logic circuit equivalent to a synchronous T flip-flop. These two signals will, in the analog part of the booster, control the MOSFET switching and have to be further modified beforehand to fulfill some necessary qualities. The most crucial prerequisite is that both series of MOSFETs never be switched on at the same time as this would result in a short-circuit between VP and VGND. Due to unavoidable, finite rise and fall times a duty cycle of the control signals of below 50% is thus necessary.

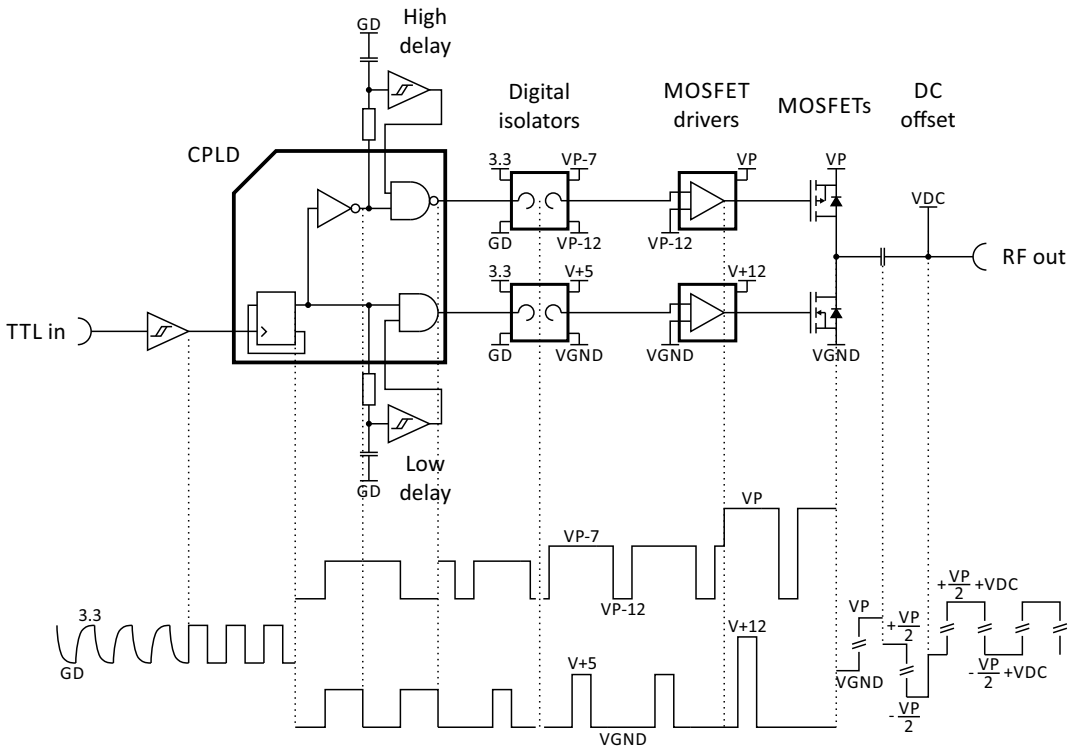

Figure 4.13: Sketch of the inner workings of a digital high frequency voltage booster for square wave signals.

In other words, a short dead time where neither series of MOSFETs is active between switching has to be provided, which can be accomplished by artificially shortening the control signals' active states. This is implemented by feeding both control signals into separate RC-circuits outside the CPLD, which results in a sawtooth signal. In turn, this signal is squared up again by a Schmitt trigger, which, due to the trigger's threshold switching behavior, leads to a small time delay relative to the original signal, independent of its frequency. Logically ANDing this delayed signal with the original one thus leads to reduction of the duty cycle. If one of the two initial signals is inverted before this process (as can be seen for the high side signal) a phase-shift of 180° can be provided. Because the high side p-channel MOSFETs are active low another inversion of this signal has to be carried out by the CPLD.

Up until this point all involved signals are at a TTL level of +3.3 V relative to the logic ground GD. The MOSFET gate signal drivers however, operate at +5 V. Furthermore, the high side driver ground can not be below VP-12 V and the output signal ground VGND should not be the same as the digital ground to minimize noise in the digital part. Decoupling of the TTL signals generated in the CPLD into the actual driving signals is thus necessary. This is accomplished by two digital isolators, one transforming the low side signal to an amplitude of 5 V relative to VGND while the

other transforms the high side signal to a working range of VP-12 to VP-7 V. Finally, the MOSFET drivers transform these inputs to gate driving signals with an amplitude of +12 V, relative to VGND and VP-12, respectively. For simplicity only one MOSFET of each type is shown in figure 4.13, but actually several are used in parallel on each side to allow for higher load currents. The so produced signal thus oscillates between VGND and VP. To establish a symmetric oscillation between +VP/2 and -VP/2 decoupling via a high-end capacitor is implemented before the signal is emitted. Furthermore, the same capacitor allows for the signal to be offset by a DC voltage VDC. This is usually done to implement a small pulling potential between adjacent ion guides.

In principle, all voltages and signals needed could be generated in one integrated system, but this is not done for two major reasons. On the one hand, the schematic process shown produces only one oscillating signal while two are needed for just one ion guide. Devices for two signals phase-shifted by 180° (easily implemented by logical negation) have thus to be supplied by one booster. As the MOSFETs generate quite a lot of heat it is advantageous to combine boosters for two ion guides (or one ion funnel with two stages) into one 19" subrack with one shared heat sink. This, however, usually only leaves enough room to generate static supply voltages (such as the +3.3, +5, and +12 V used) through switching power supplies. On the other hand, dedicated embedded system for generation and measurement of a series of different voltages and currents has been designed to control the whole setup anyway. This can be easily used to supply all needed non-static signals and voltages (TTL in, VP, VDC) and will be discussed in the following section. More information on the RF booster containing a PCB layout and wiring schematics can be found in appendix B.2.

As is the case in all high frequency applications impedance matching of this system's individual parts to each other is crucially important to obtain consistently good signal quality [284]. First and foremost, this includes all supply cables connecting the booster to the ion guides and oscilloscope. If cable and instrument impedances are not matched, signals will be reflected at the connections and these reflections will be superimposed onto the original signal, severely decreasing its quality. Due to the use of square waves 93 Ω impedance cables have been chosen for two reasons, the first being minimum capacitance per unit length. This is important, as high cable capacitance, such as in the more commonly used 50 Ω cables, generally leads to broadening of the edge transitions, which again means decrease of signal quality. For this reason, a termination circuit is connected at the cable end closest to the supplied ion guide. It consists of two 50 Ω high power thermal resistors and a 2.2 pF capacitance, all in series, connected to ground. The second advantage of 93 Ω impedance cables becomes apparent here, because the use of larger termination resistors leads to lower AC idle currents and thus

power dissipation. The combined resistance of 100 Ω is close enough to the cable value to make for good termination, while the capacitance blocks low frequency currents, which need not be dissipated as they don't affect signal quality. The capacitance also blocks the aforementioned DC offset, which would again result in useless power dissipation.

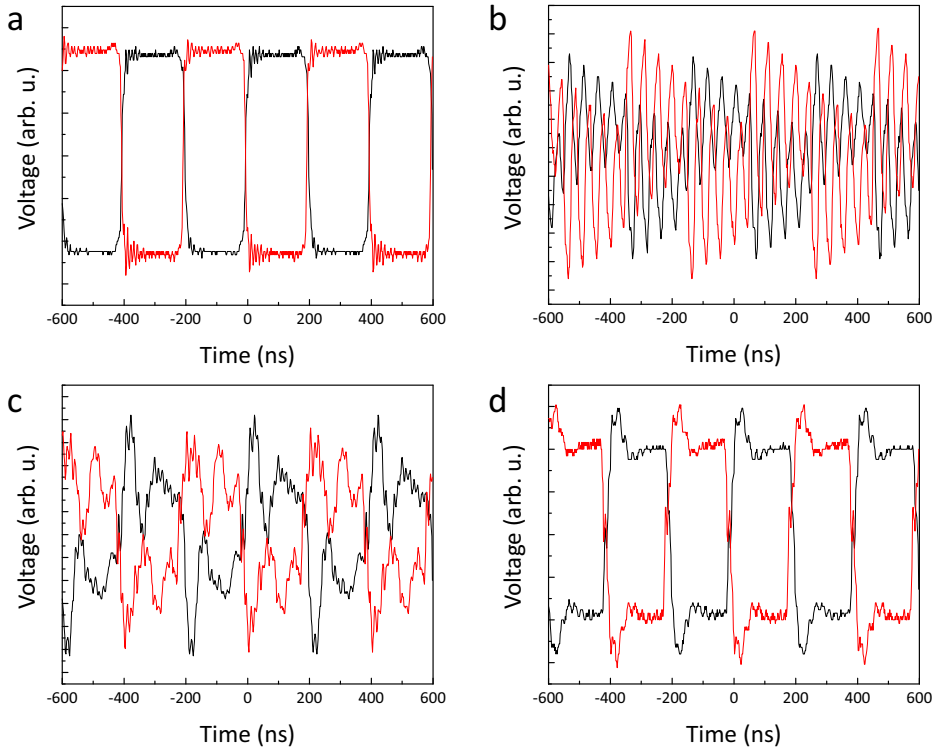

Figure 4.14: Impedance matching of the RF booster signal to the supply cable. Input during the measurement: 5 MHz, thus 2.5 MHz output measured here. **a** - Output directly at the booster. **b** - Signal at the end of the supply cable without termination. **c** - Un-terminated signal when applied to a TWIG. **d** - Properly terminated signal during operation.

Figure 4.14 shows the termination circuit's influence on the signal transmitted to the ion guides. Sub-panel **a** is a direct measurement of the booster output with a 50 Ω termination resistor attached to compensate for the booster's internal impedance mismatch (a short section of cable is used inside the booster to connect the PCBs to the actual output pin). It shows a steady and clear square wave of 2.5 MHz frequency, hence 5 MHz were applied to the booster input. Sub-panel **b** shows how the signal would look at the cable end close to an ion guide without termination circuit. Severe reflections are superimposed onto the original signal and it is barely recognizable anymore. Connecting to a TWIG in this configuration (sub-panel **c**) mitigates this somewhat due to the TWIG's inherent, but very small, load. However, a signal of this form is still much too compromised to be of practical use. Furthermore, such cable reflections can lead

to energy dissipation at the MOSFET outputs, leading to unnecessary and possibly detrimental heating of these parts. Only after connection of the termination circuit (sub-panel **d**) can one consider it to be close enough to the original output, although some small overshoot can still be observed due to the remaining mismatch of 93 Ω cable impedance and 100 Ω termination resistance.

An unavoidable drawback of this solution is the significant amount of heat, which is dissipated by the thermal resistors. A group of termination circuits sufficient for three ion guides is thus usually mounted together on one aluminum board with internal water cooling to remove this excess heat. Furthermore, impedance matching of the ion guides themselves is not implemented in this scheme. This would necessitate a significantly larger effort as either ion guide impedances would have to be measured and individually matched LC-circuits constructed or an actively self-adjusting circuit would have to be designed and built. The second option is preferable as impedances vary with applied frequency, which is certainly important here. However, as figure 4.14d shows, a TWIG's impedance influence on signal reflections is not significant to begin with. For the ion funnel, which exhibits a much larger capacitance, the effect is much more pronounced. This capacitance, however, also leads to resonance behavior of the funnel in a certain frequency range. There, the signal takes sinusoidal shape, an effect which could not be mitigated by impedance matching anyway.

4.5.2 Supply and Measurement Electronics

All supply voltages and signals needed to operate the aforementioned RF boosters as well as all other parts of the ESIBD setup are generated by a single embedded control system. This has, for the most part, been discussed in great detail in [265], but for the sake of completeness a brief overview will be given here. Some additional features developed within the scope of the present thesis will also be explained.

Overall, the supply electronics consist of a series of eurocard format PCB boards, each with a unique functionality, all of which are mounted inside a single 19" subrack. Connection and signal transfer between individual boards is implemented through a modified, full-duplex serial peripheral bus (designated *BBus*, see figure 4.15) transmitted on a flexible ribbon cable. A central microcontroller (on the CPU board) controls all transmissions as well as user interface in- and output via a TFT touch display. Alternatively, control via a lab computer is also possible through an FTDI-facilitated USB connection. The system is thus able to operate in a fully standalone mode or be controlled remotely with both features possible at the same time. Especially in a laboratory environment crowded with bulky instrumentation this represents a significant

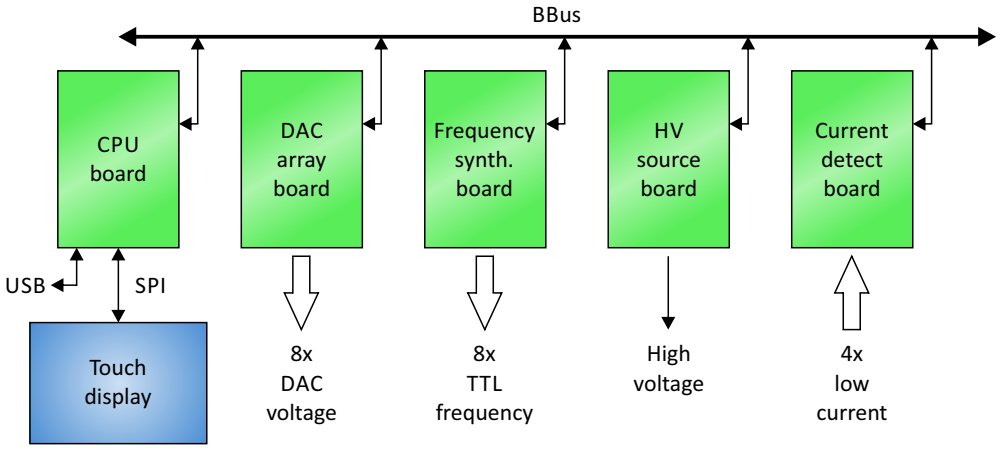

Figure 4.15: Schematic overview of the embedded ESIBD control and supply system. From [265] with modifications.

advantage over a single control mode. The main reason to build an embedded system with central microcontroller, however, is the need for precise timing of operations (see description of current detect board below). Long-range remote control capability, such as from a home or office PC, via Ethernet or Wi-Fi is in principle already possible with the currently used components, but still has to be fully implemented.

All boards except the CPU board have a single, individual purpose of either generating or measuring signals. For example, as much as eight completely independent DC voltages in variable ranges from -10 to +10 V are generated by the DAC array board. These are either used directly as small offset voltages for RF boosters (VDC, see previous section) or as control voltages for devices with analog input capability. Two power supplies fall into the latter category. One is a variable +6 kV module used to generate the ESI needle potential. The other is a variable high-power supply, which will be used in the future to generate the RF booster's amplitude voltage VP in a range of 0-100 V at 500 W maximum power. It will be described in future publications. Until now, variable benchtop laboratory power supplies have been used to generate VP in a range from 0 to 80 V. The TTL input signals for the RF boosters are generated by a dedicated frequency synthesizer board capable of generating eight individual signals in a range of 0.1 Hz to 70 MHz in steps of 0.1 Hz. The HV and current detect boards will be discussed in more detail below.

The connecting element between all boards is, as already mentioned, the peripheral bus called BBus. During a dedicated send/receive phase exchange of 16 bits of data is carried out serially between the CPU board as master and one of the other boards as slave. The transfer protocol itself has been discussed more thoroughly in [265], but one detail is worth mentioning here. The control signals sent via BBus have to be received

and interpreted by some kind of logic circuitry. Thus, every board features at least one CPLD, similar to the one mentioned in the previous section, albeit with a more sophisticated programming. There, a state machine implements the serial data transfer by clocked writing to (and reading from) an internal shift register realized through a series of T type flip-flops. It also interprets the received data to some degree and acts accordingly, thus either switching certain board devices on and off or relaying parts of the data to them. In order to completely control the number of macrocells used in this manner programs for these CPLDs were written in ABEL. Although logic programming is nowadays usually conducted using more high-level languages like VHDL or Verilog this older language is much closer to the hardware. This allows for a more direct control of macrocell use, whereas higher level languages tend to require a certain amount of overhead. As the CPLDs on some of the boards should be as small as possible in order to minimize power consumption the more time-consuming, but macrocell-wise more efficient programming in ABEL was chosen.

High Voltage Board

Figure 4.16 shows the work flow of a high voltage board. The CPLD is supplied with command information via the BBus and shifts it into its internal shift register. The command word contains control data for the DAC (digital to analog converter), which is passed on by the CPLD. This results in a variable control voltage put out by the DAC with 16 bit resolution. The board can produce high voltage in a range from -1.1 to +1.1 kV at a maximum current of a few mA. This is basically done by two HV sources on the board, one for positive, the other for negative voltages. The exact level of high voltage generated is proportional to the control voltage supplied by the DAC. As there are two separate sources for positive and negative values the full 16 bit range is available for both polarities.

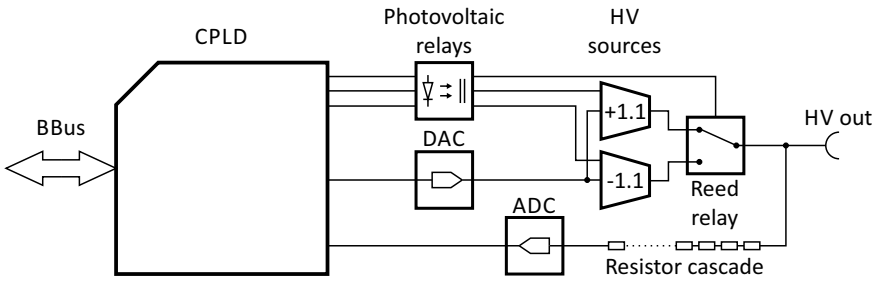

Figure 4.16: Schematic wiring diagram of the high voltage board.

A series of three photovoltaic relays (displayed as one in figure 4.16) controlled by the CPLD act as switches for two major purposes. Two of them turn each individual

HV source's supply voltage on and off such that only one of them ever operates at the same time, while the third controls the state of a reed relay, which connects the correct HV source output to the board output. As an additional, security-related feature the outputs of the two supply voltage controlling photovoltaic relays are also used to drive a bright red warning light on the front of the 19" rack. This clearly indicates danger by high voltage to everyone in the lab. Some care has to be taken programmatically to first switch both HV sources off before changing polarity. This is so the reed relay won't stay stuck in a particular configuration due to high currents flowing when either of the HV sources is on and the relay switched. Finally, in order to directly check and measure the high voltage output it is connected to an ADC (analog to digital converter) via a serial resistor cascade. The latter being necessary to reduce the voltage to a level manageable by the ADC, which converts it to a digital signal with 24 bit resolution. This result, in turn, can then be sent by the CPLD via BBus to the CPU board. See appendix B.3 for PCB layout and wiring diagram of the HV board.

Current Detect Board

The current detect board enables continuous, floating measurement of up to four currents in the pA regime. A simplified schematic wiring diagram of its inner workings is shown in figure 4.17. This is the only board which features two CPLDs. The so-called low side CPLD only handles BBus data transfer and relays relevant data to the high side CPLD. A series of digital isolators of the same make and model as the ones used in the RF boosters electronically decouple the signals between the two CPLDs. This is necessary because of the prerequisite to measure at a floating potential as many current sources (e.g. the ESI needle) are at high voltage levels. The board's high side, which contains almost all the functionality, thus has to be completely decoupled from the low side, which is connected to all other boards via the BBus. It consists of two 24-bit ADCs (only one shown), each being able to convert two voltages (again, only one is shown) into digital signals. These are generated through conversion of the sense current by an operational amplifier circuit. Furthermore, to each thus measured device a small bias voltage (± 10 V) can be applied through the use of 16-bit DACs. Their output is connected to the ADC preamplifier's non-inverting ($+$) input. Due to the amplifier's feedback loop the inverting ($-$) input will be driven towards the DAC potential, thus applying it to the sense input as well. Quick and easy variation of some pulling or retarding potential during measurement is thus facilitated.

The ADCs used in this design are of the delta-sigma modulating type. Rather than constantly and instantaneously converting voltages to digital signals they work in a

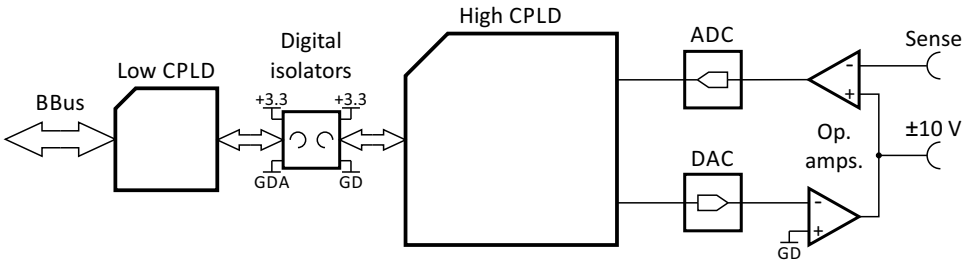

Figure 4.17: Schematic wiring diagram of the current detect board. A more detailed version along with a PCB layout can be found in appendix B.4.

burst-like manner. This is characterized by a finite, integrating conversion time after which the result can be sent to the CPLD. A crucial factor in the operation of such a current detection mechanism is the need to ensure a constant time interval of 20 ms between starting conversions. In this manner, 50 Hz noise produced by other laboratory equipment can be effectively suppressed by always converting for a complete noise period. Due to the very small currents measured by these boards even relatively minor 50 Hz contamination would otherwise prove to be quite detrimental. Conveniently, the ADCs used in this design already feature built-in oscillators, which supply them with a working clock perfectly synced to a 20 ms conversion time. However, a new conversion will only be started if and when data generated by the last one has been collected by the CPLD. A separate state machine is thus implemented there, which constantly waits for an interrupt sent by the ADC and immediately upon receiving it starts the data transfer. In turn, this is also one of the main reasons why an embedded system was chosen over a more easily implementable control solution via a lab PC. The CPU board's microcontroller is, in contrast to software running on a PC, quite capable of ensuring precisely timed collection of peripherally generated ADC conversion results. Data loss as well as 50 Hz noise interference can thus both be kept to a minimum.

Solar Power Board

The electronic decoupling mentioned above, in turn, necessitates some sort of electronically decoupled power supply chain for all high side devices, which is implemented on a separate PCB called the solar power board. In contrast to all other boards mentioned thus far it is static in the sense that its functionality can not be controlled programmatically. It thus features no connection to the BBus and no logic devices such as a CPLD. At its heart is an array of LEDs powered by buck (step-down) regulators with an initial supply voltage of +48 V generated elsewhere in the subrack by a switching power supply. Mounted close and opposite to these LEDs is a similar array of photovoltaic (PV) cells. Light emitted from the LED array is again converted into electrical

current there, thus a photovoltaic isolator is formed. Power consumption of the current detect boards has to be optimized to some degree, as one such solar power board is only capable of supplying ∼70 mA of load current. Due to the power being transferred solely via photons the PV cells' output is completely decoupled from the input ground. Contrary to a magnetic power transfer with a coupling capacity of some 10 to 100 pF such a photonic power transfer has a capacity in the single digit pF range. Furthermore, there is no inherent AC current superimposed. This +15 V output is then modulated by a further series of buck regulators and voltage converters such that all supply voltages needed by one current detect board (+3.3 V, +5 V, ±12 V) can be generated. It is thus possible for the current detect board's high side to float and match the electronic potential of any device at which currents are to be measured. The solar power board is able to supply between 0.5 and 1 W at a floating potential of some kV with an overall efficiency of 5% and a leakage current below 10 pA_{PP}. Care has to be taken to remove as much noise from these supply voltages as possible to ensure optimum working conditions for the current detect board's ADC. Otherwise, conversion results may be severely deteriorated. See appendix B.5 for a detailed wiring diagram and PCB layout of such a board.

4.5.3 Control Software

Although, as it was already mentioned, the ESIBD supply and measurement electronics system presents standalone capabilities it does so only for generation and measurement of voltages and currents, respectively. Pump and pressure data obtained by the peripheral electronics mentioned in section 4.3, however, still have to be collected and interpreted by a dedicated laboratory PC. In principle, the control electronics system would be able to read out the RS232 pressure gauges and pumps, but for the PROFIBUS devices no such capability is possible. An integral control program was thus developed using the National Instruments LabVIEW software suite. It is capable of communication with all peripheral devices as well as the control electronics. The latter is implemented through COM-port emulation via USB, while the PROFIBUS periphery is controlled via a PCI master card. Another PCI card is used to augment the number of available RS232 ports. Through this extended peripheral communication all chamber pressures and pump status data (rotor speed, high load or temperature status etc.) can be displayed and logged. Furthermore, all electronics output signals can be controlled, while measured currents can likewise be displayed and logged.

Almost by definition this scope of control and logging abilities necessitates a robust software architecture, particularly because communication with multiple RS232 devices

can very easily lead to data mix-up or loss of communication. For this reason, a queued message handler has been implemented (see figure 4.18). It utilizes a number of message and data queues for a sophisticated, but very robust and fail-safe internal communication structure. Therein, several while loops run in parallel and fulfill different purposes. The UI event handler, for example, waits for basic input from the user interface. If such an event is detected, an appropriate message is generated and enqueued into the UI message queue (blue). This, in turn, is fed into the main message handler, which interprets message by message and either acts accordingly (by opening a new window, for example) or relays a message to another loop. Messages dequeued and processed by a loop are permanently erased. It is thus a fundamental requirement for such a system to ensure that only one loop acts as a consumer for a particular queue. In contrast however, there may be an arbitrary number of message producers as new messages are always simply added to a queue. In this way, no race conditions can occur as loops only act when specifically called upon by a message. Thus, fail-safe parallel operation of different while loops is possible.

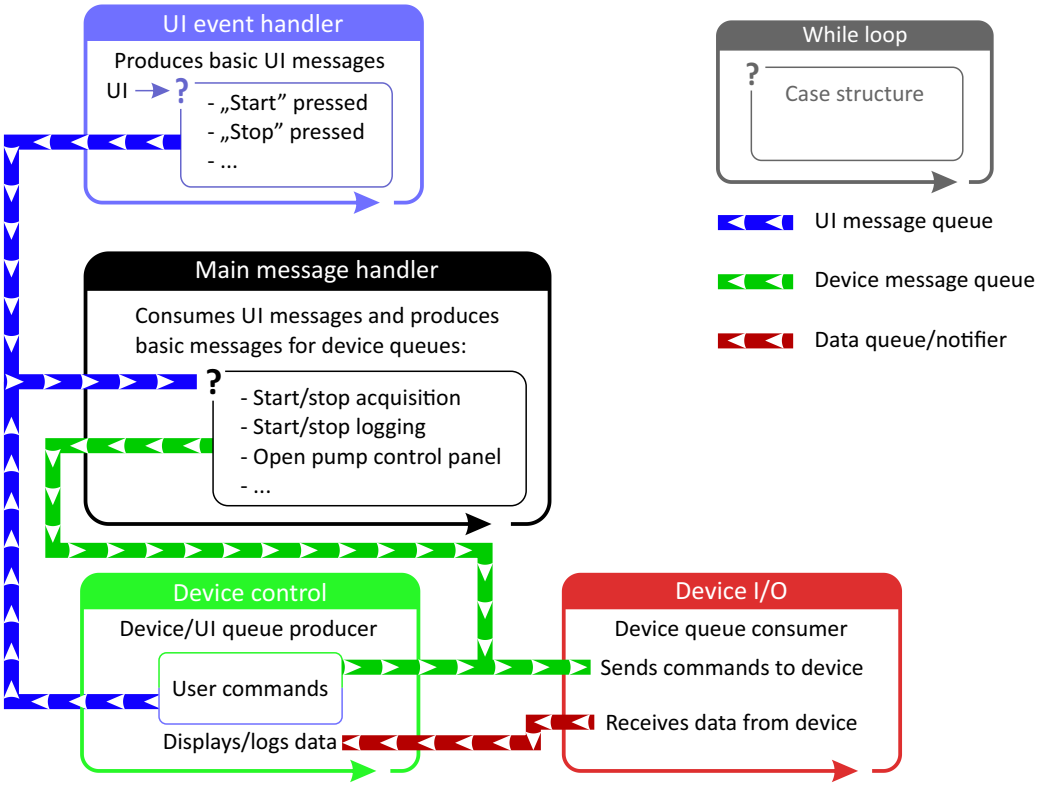

Figure 4.18: Flow diagram of the LabVIEW program used to remote-control the ESIBD peripheral electronics.

Actual peripheral device input and output operations are performed by a series of device I/O loops, one for each method of communication. These loops consume

corresponding device message queues (green) and accordingly transmit commands to the periphery. In turn, data received from devices is enqueued into a special data queue (red). This is then dequeued by dedicated device control loops, which display and log it while at the same time allowing the user to make adjustments, thus again adding to the device message queue and so on and so forth. Separating these two crucial functionalities (device I/O and user interface) allows for a smooth operation as neither process has to halt while the other runs its course.

4.6 Sample Preparation and Analysis

The ESIBD preparation chamber has already been featured in two prior works [109, 264], but some additional modifications have been undertaken in the meantime. First and foremost, the ion beam now has an unbroken connection from the source all the way to the sample. This has been implemented by omitting the quadrupole mass selector (QMS) discussed in [109] and its chamber in favor of a long UHV-compatible TWIG, to facilitate a first proof of principle ESIBD-STM experiment (see following subsection). This UHV-TWIG transmits the beam from the gate valve between chambers 3 and 4 right up to the sample. The gate valve itself, however, still incurs the single greatest loss in ion beam intensity after the atmospheric pressure interface. A solution for this problem is in its early stages and will be discussed in future works. The current solution has been implemented to facilitate a proof of concept ESIBD preparation and following STM measurement (see next subsection).

Figure 4.19 shows side and top views shot through the chamber windows during operation. The new UHV-compatible TWIG is mounted at a slight tilt off of the central axis. This ensures that a molecular beam of residual gas atoms with traveling direction parallel to the ion beam must hit a chamber wall at some point as no unbroken optical axis is given (see section 4.3). In order to measure ion beam intensity and necessary retarding potential for soft-landing without contaminating the sample a test pad was installed behind it. This is connected to the sample's bias voltage feedthrough and can be positioned close to the TWIG exit for preparatory measurements. As the ESIBD setup is now completely connected to the STM chambers sample transfer between the two is facilitated via a long manipulator (see section 4.1), which can be seen in the top view. Other than that, the sample mounting stage is identical to the one presented in [109, 264] with a pneumatic bellow for tight gripping of the sample and a filament for electron beam heating.

Some significant modifications have been made to the so-called Feulner cap [285, 286] as compared to its predecessor discussed in a previous work [109]. Its main advantage is a

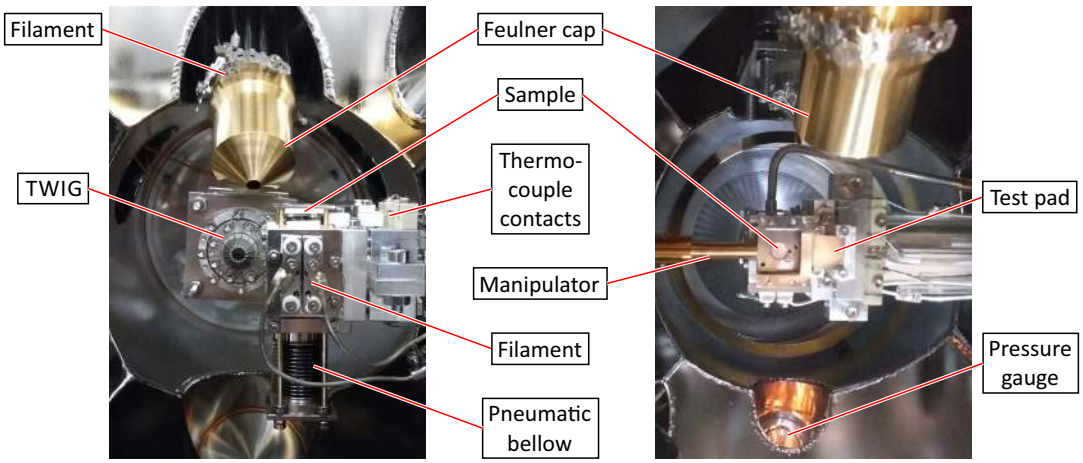

Figure 4.19: Side and top view photographies of the preparation chamber in operation. In the right image the long manipulator connecting the ESIBD and STM chambers can be seen attached to the sample. The operating pressure gauge's glowing filament can be observed as well.

significant boost of the signal-to-noise ratio during temperature programmed desorption (TPD) measurements, where the sample is brought close to its inlet and heated, such that adsorbed molecules are desorbed in a controlled manner. These are then ionized by electrons emitted from a filament located inside the cap (see figure 4.20) and accelerated towards a quadrupole mass selector with subsequent detector. Without such a cap the partial pressure of molecules available for ionization would be greatly reduced, amongst other disadvantages. In order to further increase the performance compared to the older design (figure 4.20a) its opening angle was increased to allow for more direct flight paths from the sample to the ion source region around the filament and grid. This should decrease re-adsorption and thereby increase the number of ionized molecules, leading to even higher signal-to-noise ratios. Also, its length was reduced to further decrease areas available for re-adsorption. As the metal cap is mounted to a relatively big ceramic part of the QMS its back end was extended to facilitate a more stable mounting procedure utilizing set screws. The bulk material used is aluminum, galvanized with a layer of gold to decrease the sticking coefficient. The whole cap can be heated by electron beam heating from the outside using a filament fixed to its back end (visible in the left image of figure 4.19). Unfortunately, it was installed rather recently and initial measurements comparing it to its predecessor still have to be conducted and can thus not be included in this thesis.

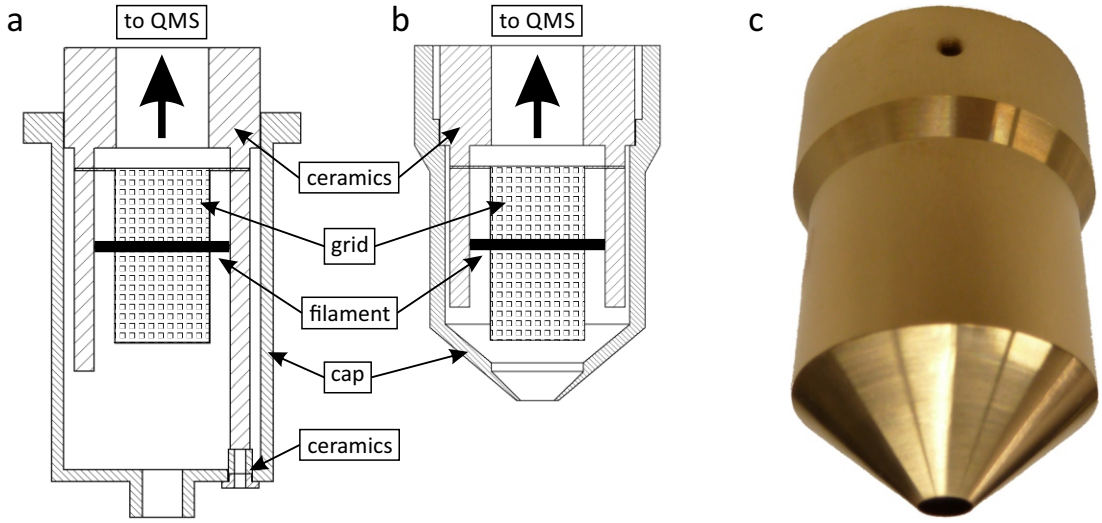

Figure 4.20: Feulner caps used for TPD experiments in the ESIBD preparation chamber. **a, b** - Schematic views of the old and new design, respectively. **c** - Photo of a prototype built according to the new design.

4.6.1 2H-TPP on Au(111) and Ag(111)

In a preliminary proof of principle experiment to test the fundamental usability of this setup a solution of 2H-TPP was electrosprayed (see appendix A.3 for information on chemicals and experimental parameters) and the resulting ion beam subsequently deposited onto two different metal samples, namely Au(111) and Ag(111). 2H-TPP (figure 4.21a) adsorbs in a deformed, but mostly flat-on fashion on noble metal surfaces, well known from literature [287], which is the main reason this molecule was chosen in favor of a more thermolabile one. Rhodamine B had been considered, as its spray characteristics were well known from prior experiments, but to our knowledge there are no STM data for comparison in the literature. One preliminary test was carried out, but this yielded only agglomerated adsorbate which proved impossible to analyze using STM.

Figure 4.21 shows that ESIBD has been achieved with 2H-TPP, but that some additional refinements on the setup have to be implemented to improve its performance. During two initial preparations, the first on Au(111), the second on Ag(111), ion beam currents of 100 pA and 50 pA could be reached on the sample, respectively. On the Au sample this was held for 30 minutes, yielding a total deposition charge of 50 pAh, while on Ag a significantly longer deposition was chosen in order to reach 125 pAh. Only a small decelerating voltage of $\sim$+1-2 V had to be applied to reduce the current to zero, which indicates a rather low ion kinetic energy, at least in z-direction. During deposition the sample was thus held at ground potential, as a few eV of energy upon impact are

not sufficient to break molecules of this size. The samples were then transferred into the STM, cooled using liquid nitrogen, and subsequently investigated. However, surface coverages achieved in both preparations were so low that no single molecules could be found adsorbed on open terraces of the crystal. On Au(111) step edges were sparsely decorated (red circles in figure 4.21b), while on Ag(111), presumably due to the larger deposited charge, a regular step edge decoration was achieved (panel c). It is, however, unclear if this is truly 2H-TPP as sub-molecular resolution proved to be elusive due to vibrational noise during STM measurement.

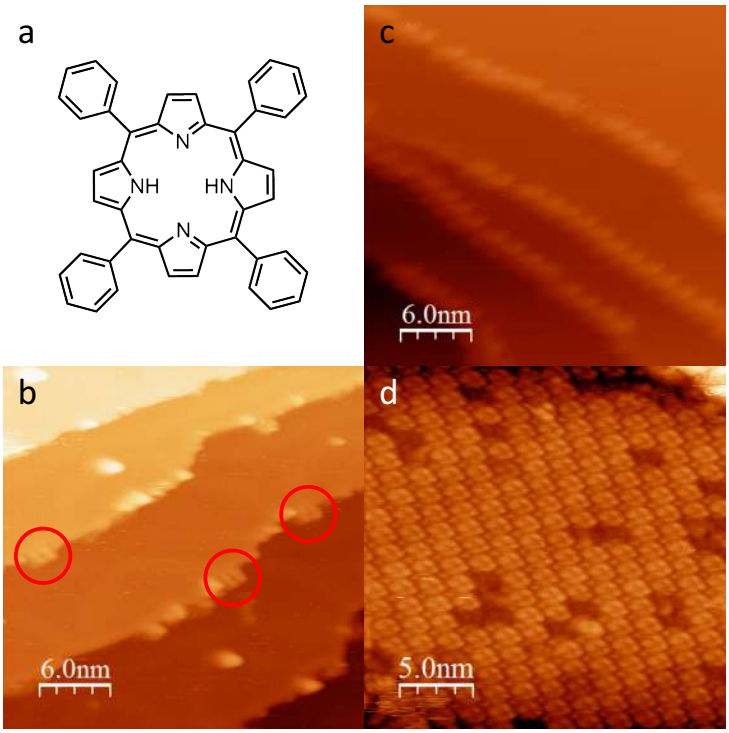

Figure 4.21: 2H-TPP investigated on Au(111) and Ag(111) samples using ESIBD-STM. **a** - Chemical formula of 2H-TPP. **b** - First preparation of 2H-TPP on Au(111) (+1.28 V, 7e-11 A). **c** - 2H-TPP on Ag(111) (+1.36 V, 1.1e-10 A). **d** - Second preparation on Au(111) (+1.25 V, 1e-10 A). [288]

Nominally, the deposition currents and times mentioned above should be sufficient to deposit a much higher coverage onto a surface, if each molecule is assumed to be singly charged. Even if higher charge states are achieved, which is not likely due to the molecule's small size, this could not explain these unexpectedly low coverages. A significant portion of the ion beam thus has to consist of unwanted contaminations, which are then co-deposited. Indeed, especially the outer parts of the Au(111) sample exhibited many contaminated spots. This, at least, fits very well to the ring-like ion distribution in a TWIG mentioned in section 4.4.1. To achieve a more even distribution

on Ag(111), and desorb some of the more volatile contaminants, the sample was lightly annealed to 100°C for 10 minutes before cooling down and measuring. Annealing at these parameters is not expected to decrease 2H-TPP coverage in any case, as even the unfunctionalized porphine backbone does not significantly desorb at this temperature [289]. This procedure led to a much cleaner surface, suggesting that most of the contamination consists of very light and volatile molecules. A distinction between solvent or molecule feedstock contamination has yet to be made, possibly using the system's built-in TPD capability.

In order to further increase the deposition charge a special dummy sample holder with a 1 mm pin was built to find the optimum manipulator position with respect to the third TWIG's exit aperture. It was thus possible to both increase the deposition current to 180 pA, while also depositing more closely to the sample center, which is easier to access due to the STM's limited measurement area. After a third deposition, again on Au(111), with this current for 2 h and a total of 360 pAh, finally self-assembled islands of 2H-TPP could be observed (figure 4.21d). Similar to the two initial preparations a significant amount of co-deposited contaminants were observed in this case, although fortunately with no detrimental influence on the molecule's attractive interaction.

In any case, the need for a mass-selecting filter in the beam path has become apparent through this preliminary set of experiments. The resonance behavior of higher order multipoles, such as the TWIGs used in this setup, is simply too little selective regarding m/z ratios of molecules to be of efficient use in cleaning the beam from unwanted contaminants. Even more important, however, is a significant increase in beam current to reach higher coverages more quickly. In the following chapter, we will discuss some possible reconstructions which have to be made in order to reach this goal.

5

Conclusion and Outlook

Over the last 100 pages or so the necessary steps and requirements for building a functional ESIBD setup have been laid out. It has been shown that ESIBD used as a sample preparation technique for scanning probe microscopy setups is a powerful alternative to the more traditional method of OMBE, but significantly more complicated to implement. Here, the most important conclusions derived from investigations and construction efforts conducted throughout this thesis will be summarized. Since the setup's current state leaves ample room for augmentations and refurbishment an extensive outlook on potential future improvements will be given at the end.

First, a series of STM experiments utilizing OMBE as the predominant sample preparation procedure was discussed (chapter 3). Molecules investigated during these experiments had been chosen specifically to be close to the limit of OMBE's capabilities with regard to thermolability. Rare earth sandwich complexes designated as $Tb(OETAP)_2$ which are promising candidates due to their single molecule magnetic properties and had not been investigated with STM before, exhibited self-assembling behavior on noble metal surfaces. This has been found to be markedly similar to another such molecule ($Dy(OETAP)_2$) investigated by others, and almost independent of the type of noble metal chosen. In all cases a highly intriguing distribution of apparent molecule heights in self-assembled islands could be observed, with bright species being susceptible to irreversible switching into darker ones by tip-sample interactions. Whether this behavior stems from conformational changes or rather the metal atom's charge state or indeed some as yet unknown source is still a matter of debate and leaves ample room for further studies. Pertaining to the limits of OMBE in this case were findings of cracked single OETAP molecules during preparations, which hinted at the molecule's thermolability.

In another such set of experiments a family of alkyne-functionalized pyrenes, a molecule well known for its fluorescent properties, was investigated. They exhibited

a spectrum of different self-assembling behaviors upon adsorption on Ag(111) and Cu(111), depending on whether phenyl or pyridyl termination moieties had been used and where. While the test group using phenyl moieties consistently showed non-interacting random distributions of molecules at sub-monolayer coverages all pyridyl terminated species exhibited some form of attractive self-assembling or at least agglomerating behavior. These species thus formed a wide range of markedly differing supramolecular architectures, giving valuable insight into intramolecular interactions using such moieties. Furthermore, in some batches of feedstock material a contamination of iodine had been present, originating from the molecules' chemical synthesis route. This was, in turn, co-deposited onto the samples prepared using OMBE, because it had remained in the crucible even after thorough degassing. The adsorbed iodine had, in at least two cases, a profound influence on the molecules' self-assembling behavior and resulting supramolecular architectures. This highlights both the need for ultra-clean preparations in surface science as well as the possibilities arising from co-deposition of halogens with such molecules.

In principle, ESIBD is able to overcome the limits of OMBE highlighted by the two systems summarized above, as well as a few others mentioned in chapter 3 as well. First and foremost, it is, in contrast to OMBE, not limited by a molecule's thermolability due to the soft ionization procedure from feedstock solutions. Furthermore, the resulting ion beam can, in principle, be purified using mass selecting ion guidance systems, thus opening the gateway to truly ultra-clean sample preparations. This option has been omitted in favor of a proof-of-principle experiment, however, but will be implemented at a later stage (see below). As a sort of bonus, simply measuring the ion beam current allows for precise control of the amount of material deposited per unit time, which greatly increases preparation reproducibility compared to OMBE. This again requires a largely contamination-free ion beam, however, as well as information about the analyte ion's charge state, which can in turn be gained using a quadrupole mass selector.

A series of experimental challenges accompanies the design, construction, and operation of an ESIBD setup, however. In chapter 4, the setup and its development process during this thesis was presented as a series of separate, but intricately interacting parts. At first, a comparison of two different approaches to ESI was given, depending on whether spraying occurs at atmospheric pressure or in a low vacuum environment. The latter option had been investigated first and exhibited some, at the time, insurmountable challenges due to material failure and electrical gas discharge phenomena. This led us to postponing further experiments and switching to atmospheric spraying instead, which is now very much controllable and utilizes a relatively novel and little investigated type of atmospheric pressure interface.

Some considerations have been taken regarding the crucially important differential pumping system and it has been shown that residual gas leak rates of chamber interfaces are nicely comparable to theoretically calculated values. In principle, the system could operate just as well with one chamber less, but this requires some modifications (see below). Of course, the differential pumping system by itself is almost useless without proper guiding of the ion beam from one chamber to the next. This has been accomplished through the use of an ion funnel and three thin wire ion guides (TWIGs), which still represent a relatively novel solution to this class of transport problem. All ion guides connecting adjacent chambers are constructed using long gas-tight tube sections to further reduce the residual gas flow and thereby increase the pressure gradient. Most importantly, ion guidance at chamber interfaces remains unbroken in most cases due to special construction provisions, thus leading to very high ion transmission coefficients at all interfaces but one (see below). For all TWIGs this necessitates the use of slightly conductive SiC fixtures to give the wires mechanical stability without running the risk of charging or shorting phenomena. Overall, this combined differential-pumping/ion-guiding system represents a novel and ingenious solution incorporating a series of advancements compared to similar systems. This allows for an unprecedented small size, while at the same time increasing flexibility and versatility.

An electronic system used for control and supply of almost all vital parts of this system has been introduced as an almost necessary alternative to off the rack solutions. Radio frequency (RF) signals are amplified by a custom-designed, digital RF booster, which in turn supplies the ion guides with some care taken to prevent supply line impedance mismatch. Its input as well as several other signals and/or voltages are supplied by an embedded control system, which also features the possibility for high resolution current measurements on a floating potential. The latter functionality is implemented through the use of a photovoltaically decoupling DC power supply board. In addition to complete standalone capabilities it is also possible to control all relevant register values remotely from a laboratory PC via USB. To facilitate stable control of the embedded system alongside the PC-controlled turbomolecular pumps and vacuum gauges a robust queued event handling structure has been implemented using LabVIEW.

With this ESIBD setup attached to an existing STM system a series of proof-of-principle preparations and subsequent STM measurements has been conducted using 2H-TPP as the analyte molecule. After some initial impediments a coverage sufficient for the formation of extended, self-assembled islands on Au(111) could be obtained. This validates the setup's principal working condition and represents, to the best of our knowledge, the first attempt of exclusively using higher order multipoles to successfully

guide an ion beam in an ESIBD setup all the way to the sample, and through all UHV stages.

Although the setup is thus in principle working as intended, there is still ample room for improvements. First and foremost, a filtering quadrupole mass selector (QMS) should be included in the ion beam to remove unwanted contamination and enable ultra-clean preparations. This will, however, presumably necessitate the use of focusing electrostatic lenses due to the QMS's poor acceptance and exit behavior, as otherwise losses in addition to those induced by the QMS's low transmission will occur. Some of these losses can be mitigated by improving the transmission at the entrance to the system's UHV part. Possibilities here include the construction of a new, much thinner valve, the use of electrostatic lenses, or the construction of a novel ion guide capable of extending into the UHV part whenever the valve is open. Another source for additional ions would be given by reverting to the low vacuum spray source. This, of course, would necessitate investigation and circumvention of all challenges encountered with this approach so far, which in itself represents an interesting and promising experimental avenue.

Less experimentally challenging, but still necessitating quite extensive changes, would be the reduction of the system size by one chamber, which has been shown to be theoretically possible. This would in turn also imply reduction of the number of pumps and thereby increase stability of the system against vibrational noise. Some precautions regarding the formation of a residual gas molecular beam have then to be taken, however, as the system size would shrink well below the critical length L_{min} discussed in section 4.3. More importantly, room for the QMS (and an ample working pressure below 10^{-7} mbar) would have to be supplied before the entrance into the UHV part. These prerequisites would make a significant reconstruction of the current solution necessary. Plans already exist for some of these modifications, which would also improve the flexibility of the system's non-UHV part, compared to the more rigid aluminum box, which is employed now.

Last, but not least, a multitude of possible preparation and measurement experiments will represent the actual fruit of all this labor. The new Feulner cap design as well as a precise temperature ramp control for TPD experiments remain yet to be tested. Finally, in order to make full use of the ESIBD setup's mobility the preparation chamber and its sample manipulation system should be adapted such that connection to any other in-house setup can be facilitated and all sample holders used for preparations. Apart from several scanning probe machines this would also allow connection to a number of XPS setups, one of which is frequently used at synchrotron beam lines, thus greatly enhancing the scope of usability for the ESIBD setup presented in this thesis.

Appendix A

Materials & Methods

A.1 STM: Samples and Procedures

SPS-CreaTec Setup

All STM images in chapter 3 were obtained close to the boiling point of liquid helium (∼5-6 K) at base pressures below $5 \cdot 10^{-10}$ mbar. Images were recorded in constant current mode, unless noted otherwise, with an electrochemically etched and subsequently sputtered tungsten tip. Image analysis was conducted with the WSxM software [290]. Feedstock molecules used in this part of the thesis were custom synthesized with purities above 90%. They were thoroughly degassed at temperatures close to the deposition temperature for extended periods of time before deposition. All crystal samples used (Ag(111) and Cu(111)) were obtained from Surface Preparation Laboratory. These were cleaned by repeated cycles of sputtering with Ar^+ (at 800 eV and $2.5{\cdot}10^{-5}$ mbar pressure) and subsequent annealing to 450°C, and their surface quality routinely checked by STM before deposition. Preparations were conducted with the sample at room temperature, unless cold preparations are noted, which were facilitated through flow cooling with liquid helium to reach sample temperatures anywhere between -170°C and room temperature.

SPECS Setup

STM images in chapter 4 were obtained at 90 K, using liquid nitrogen cooling, and at base pressures below $2 \cdot 10^{-10}$ mbar. As above, images were recorded using the constant current mode and a similarly prepared tungsten tip. Image analysis was likewise conducted using the WSxM software [290]. 2H-TPP from Sigma-Aldrich (⩾99%) was used as feedstock material, but see apendix A.3. Crystals used (Ag(111) and Au(111)) were likewise obtained from Surface Preparation Laboratory and cleaned similarly by

sputtering (1 keV) and annealing (between 570 and 670 K), with surface quality again checked for atomically flat areas using STM. Preparations were conducted with the sample at room temperature.

A.2 SIMION: Simulation Parameters

All ion trajectory simulations were conducted using SIMION 8.1 modified with custom coded user program sections to allow for hard sphere collisions with a buffer gas obeying a Maxwell-Boltzmann distribution. Additional gas kinetic parameters needed for collisions are pressure, collision cross section and mass, the last being calculated by assuming ions to have the same density as nitrogen and correcting for the larger volume. Simulation time steps were defined as the minimum of either a predefined fraction of one RF cycle or the timespan between two collisions. Overall simulation time was chosen long enough to ensure equilibrium conditions were reached. This was usually the case within 1000 µs, but sometimes longer runs were needed.

Space charge repulsion was simulated using SIMION's built-in factor repulsion approach where simulated ions are point charges actually consisting of bunches of ions (a super-particle approximation) and each point charge's effective charge is the product of a single ion's charge times a given repulsion factor. Single ions were assumed to be spherical which allowed calculation of ion charge q via the Rayleigh limit for a given radius. Electrode geometries and pseudopotential field extents were specified directly in SIMION workbench. Ions were then started cold and randomly distributed over a specifiable part of the simulation space. A so-called "soft start" approach was used, where over the course of an adjustable initial alignment phase the ion charge q is logarithmically expanded from 1 to 100%, thus slowly "turning on" space charge and allowing the ions to gradually relax into a more stable distribution. This greatly reduces risk of simulation blow-up.

In order to emulate ion guides and pseudopotentials extending infinitely in z-direction ions "leaving" simulation space in z-direction were reinserted into the volume at a z-position given by a certain distribution while conserving both momentum and position in x-y. This reinsertion mechanism, if not handled properly, may very easily lead to an artificial energy transfer into the system and skewing of temperature and charge density distributions. On the upside, this approach allows one to neglect possible buffer gas drift speeds in real ion guides by directly simulating an equilibrium charge capacity. Ion beam currents can then be calculated by multiplying the resulting linear charge density with an arbitrary buffer gas speed. Ions impinging on electrode surfaces or crossing

the gap between two electrodes were considered neutralized and not accounted for any further.

Super-ion positions and energies were usually recorded from around 500 µs until the end of simulation to ensure cut-off of data strongly influenced by starting conditions. From these recorded data mean values for charge density distributions and ion temperatures as well as kinetic results such as lifetime and mean time between collisions were extracted. Furthermore, time evolutions of ion count and mean ion temperature were obtained to check if and when equilibrium conditions had been reached.

A.3 ESIBD: Solutions and Procedures

Chemicals and Solutions

Table A.1: Chemicals used to mix ESIBD spray solutions, their minimum purities and suppliers.

Chemical	Purity (%)	Supplier
Methanol CHROMASOLV	99.9	Sigma-Aldrich
Ethanol abs. puriss. p.a.	99.8	Sigma-Aldrich
2-Propanol ROTISOLV	99.95	Roth
Toluene	99.85	ThermoFisher
H_2O CHROMASOLV	99.9	Sigma-Aldrich
Acetic Acid puriss. p.a.	99.8	Fluka
Rhodamine B	95	Sigma-Aldrich
2H-TPP	99	Sigma-Aldrich

From the chemicals summarized in table A.1, solutions of both analytes (Rhodamine B and 2H-TPP) were mixed. For Rhodamine solutions a variable solvent base mixture of A:B:C 47.5:47.5:5 Vol.-% was prepared, with A = methanol, ethanol, 2-propanol, B = H_2O, C = acetic acid. Rhodamine B was then added such that concentrations between 10^{-3} and 10^{-5} mol/l were obtained, with 10^{-4} mol/l being the one used to obtain the data presented in chapter 4. Solutions of 2H-TPP consisted of A:B:C 57.5:37.5:5 Vol.-%, with A = toluene, B = methanol, C = acetic acid, and a concentration of 10^{-4} mol/l.

Preparation Parameters

Crucial parameters used during ESIBD preparations are given in table A.2 with hyphens indicating where a value is not applicable. E.g. for ESI needle, API, and sample

no RF supply parameters are given, because these devices are only driven using DC voltages. Two values for Ω_{RF} are given for the ion funnel corresponding to the high and low electrode spacing part, respectively. Currents I were obtained by connecting an ammeter in series between the device and its power supply. For ESI needle and sample this can be done continuously, while all RF-driven devices have to be disconnected from their supply and connected to a small pulling potential, again via an ammeter. The current measured then equals the ion beam current transmitted by the previous device. Due to the need for disconnection from the RF-supply this can not be done during deposition, but is rather conducted beforehand to find suitable supply parameters to reach a maximum beam current. No value for I is given for the ion funnel, because its inherent RC time constant leads to very long equilibration times, making current measurements practically useless. Currents mentioned here are approximate values and changed by as much as 20% between experiments, mainly because the needle current itself strongly depends on, as yet uncontrollable, factors such as room temperature and air humidity. Ion beam currents impinging on the sample thus likewise varied from preparation to preparation and are mentioned in section 4.6. Finally, pressures given here are at the entrance side of the corresponding device. The exit pressure of TWIG 2 is the same as its entrance pressure, as it resides fully in chamber 3. TWIG 3 also traverses through a pressure stage of $1{\cdot}10^{-8}$ mbar (see section 4.3).

Table A.2: Supply parameters, obtained currents and chamber pressures during ESIBD preparations.

Device	V_{DC} (V)	Ω_{RF} (MHz)	V_{PP} (V)	I (nA)	p (mbar)
ESI needle	3000	-	-	20-30	1013
API	200	-	-	15-20	1013
Ion funnel	200-0	1.8/0.9	80	-	1.7
TWIG 1	0	2-2.5	40	5	$2.5{\cdot}10^{-2}$
TWIG 2	-2	2-2.5	40	4.5	$2{\cdot}10^{-6}$
TWIG 3	-7	2	40	2	$2{\cdot}10^{-6}$
Sample	0	-	-	see sec. 4.6	$<5{\cdot}10^{-10}$

Appendix B

Electronic Hardware

B.1 OMBE Heating Control Unit

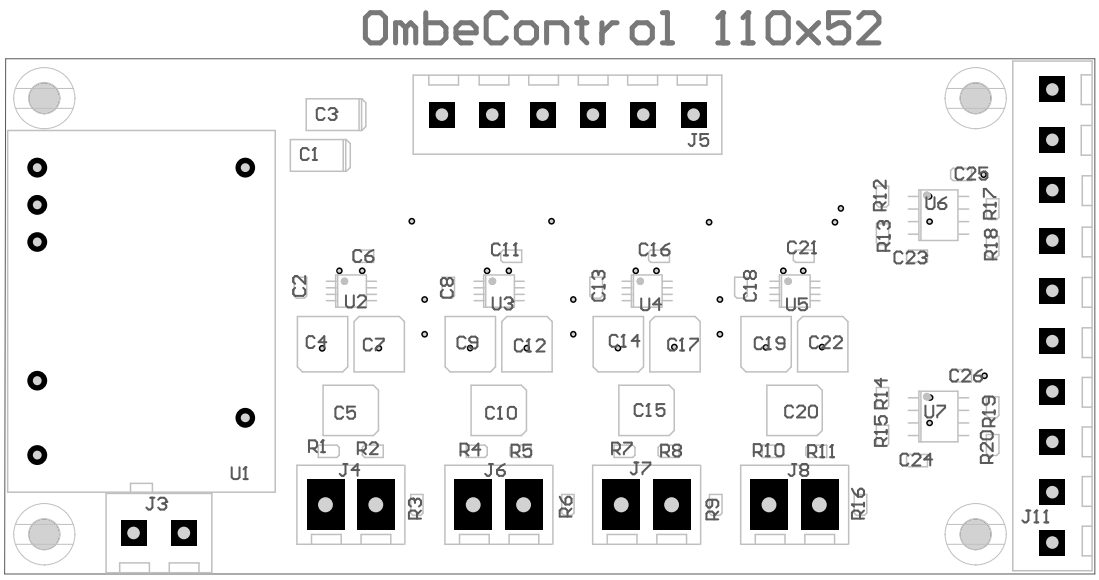

Figure B.1: PCB layout of the OMBE heating control unit.

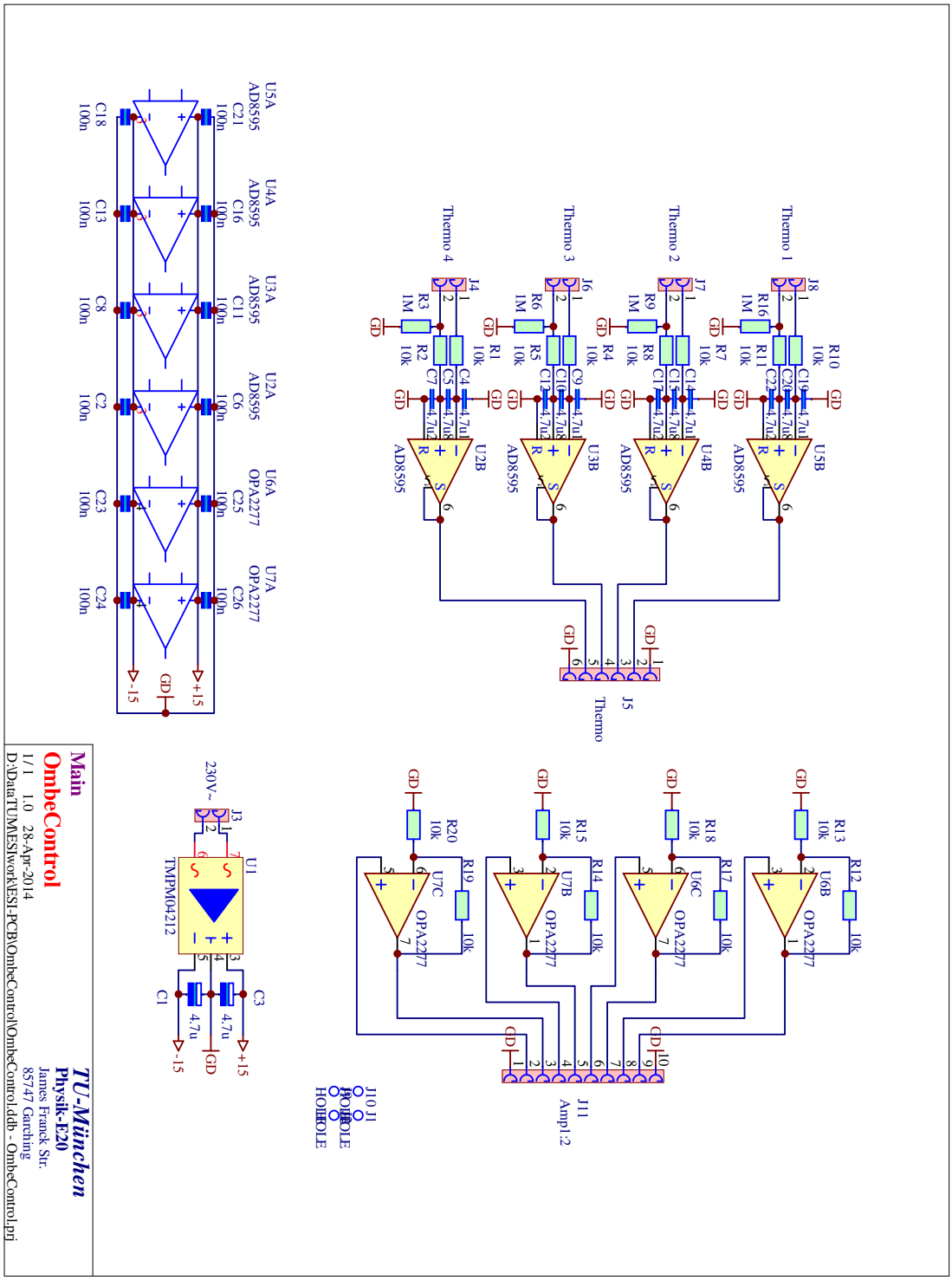

Figure B.2: Wiring diagram of the OMBE heating control unit.

B.2 RF Booster

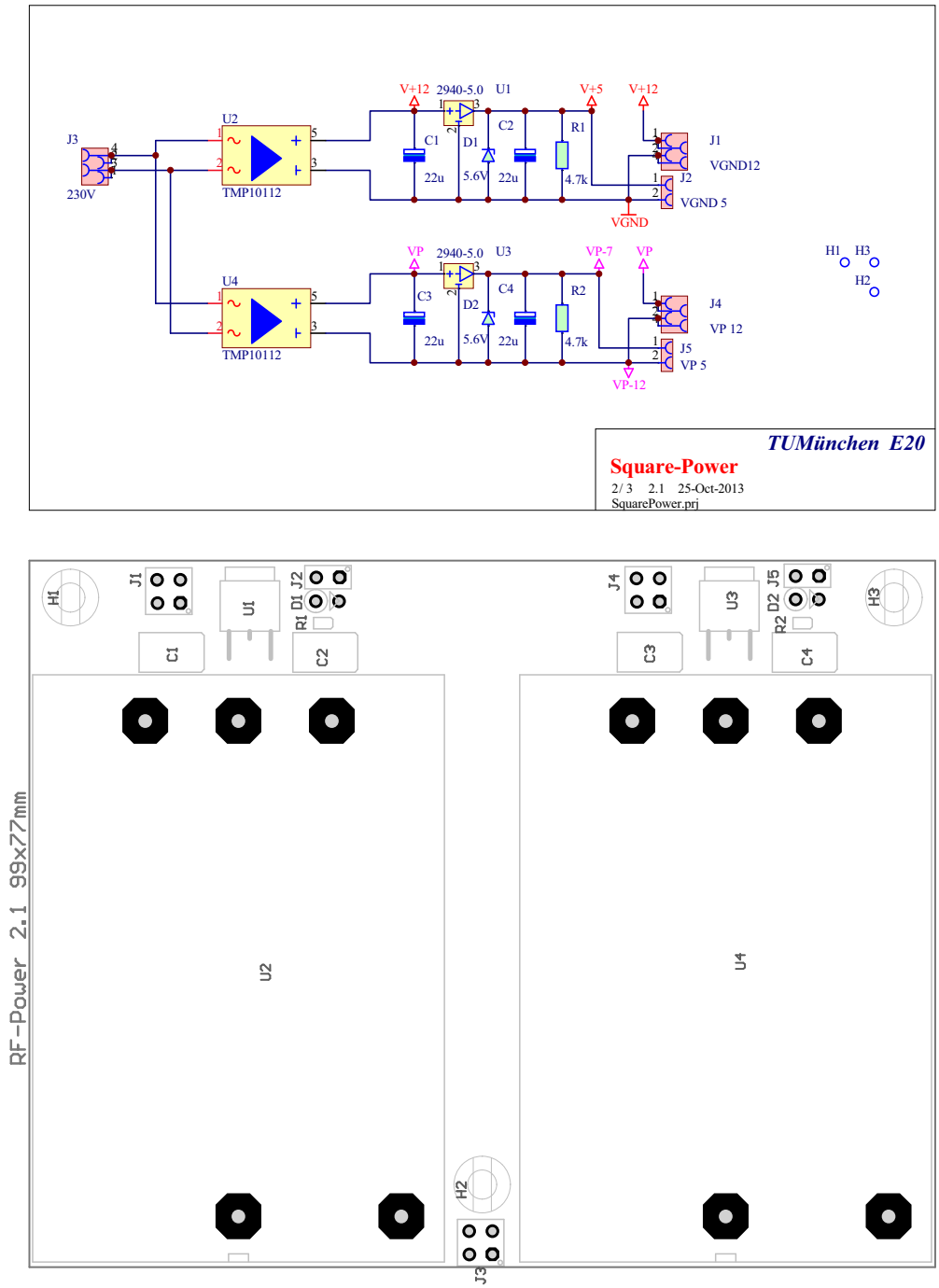

Figure B.3: Wiring diagram and PCB layout of the RF booster's internal DC power supply.

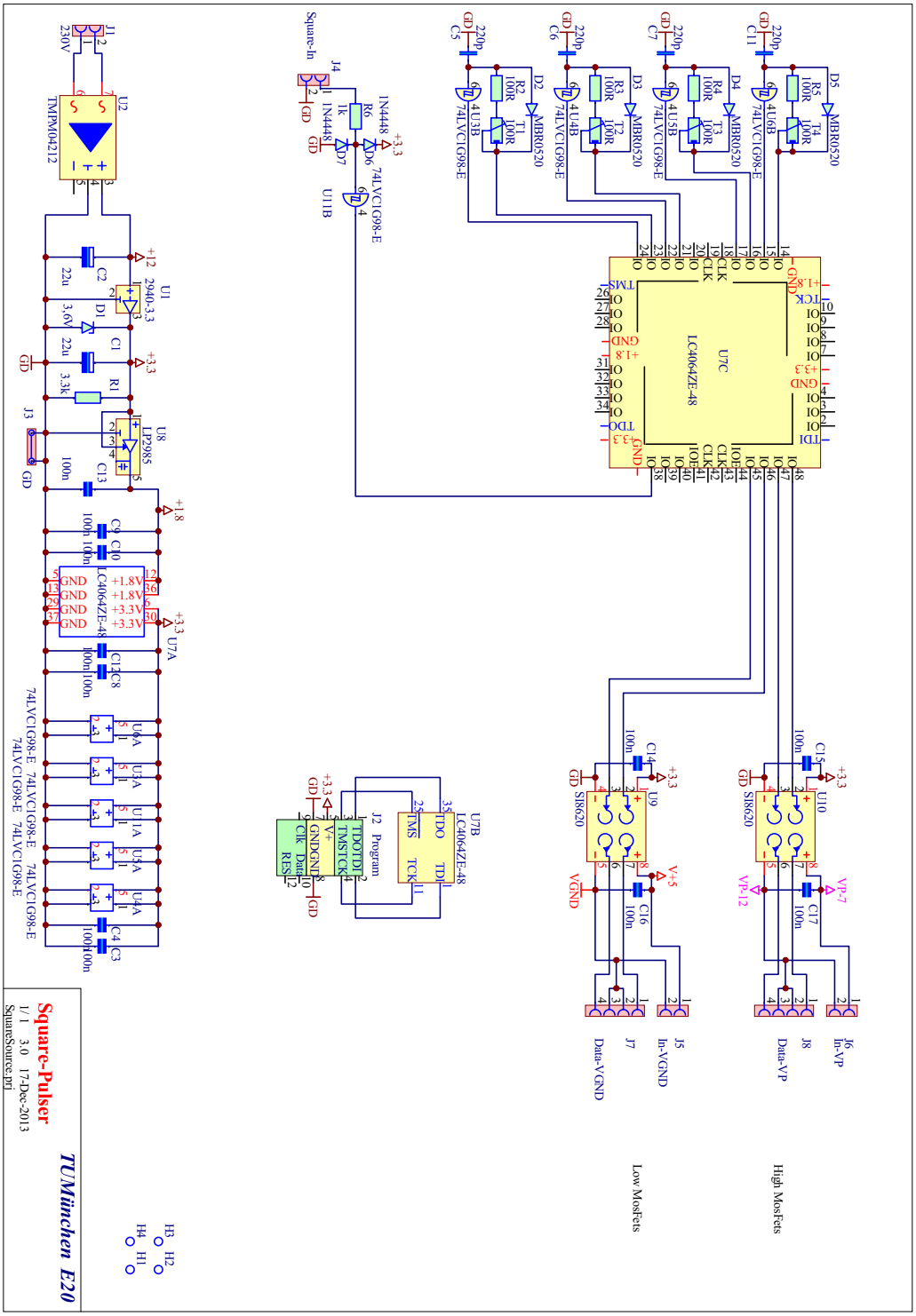

Figure B.4: Wiring diagram of the RF booster's digital signal modifying board.

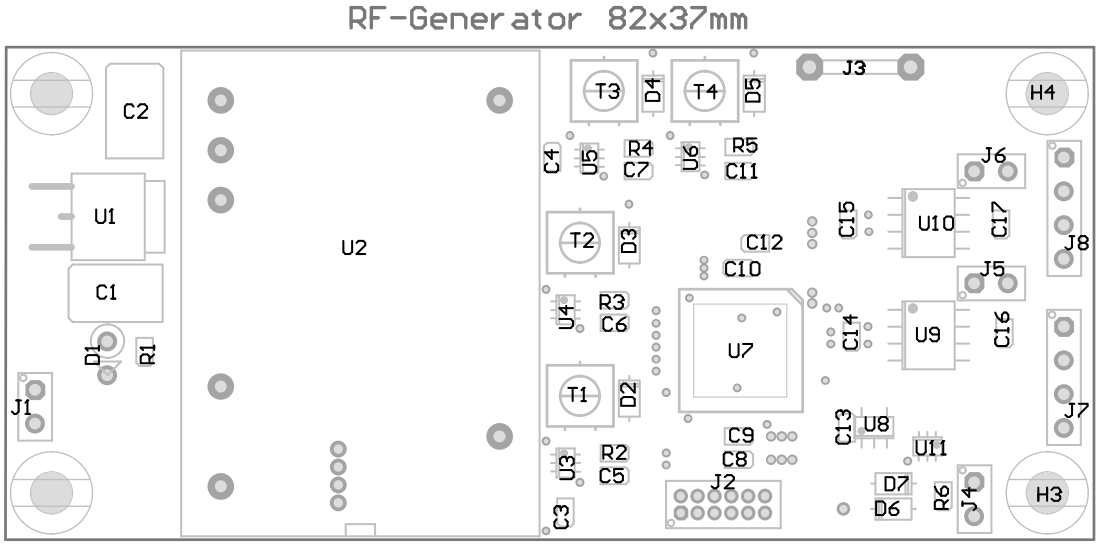

Figure B.5: PCB layout of the RF booster's digital signal modifying board.

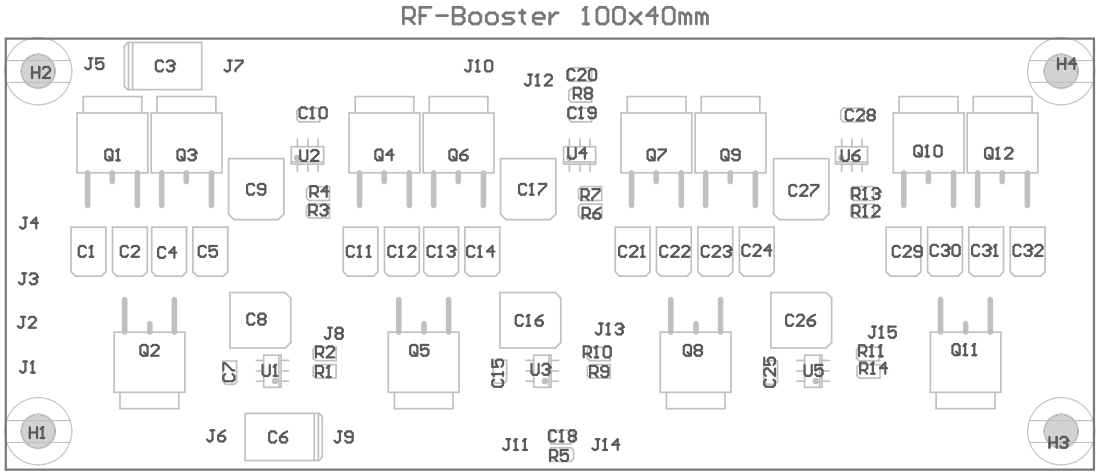

Figure B.6: PCB layout of the RF booster's signal boosting board.

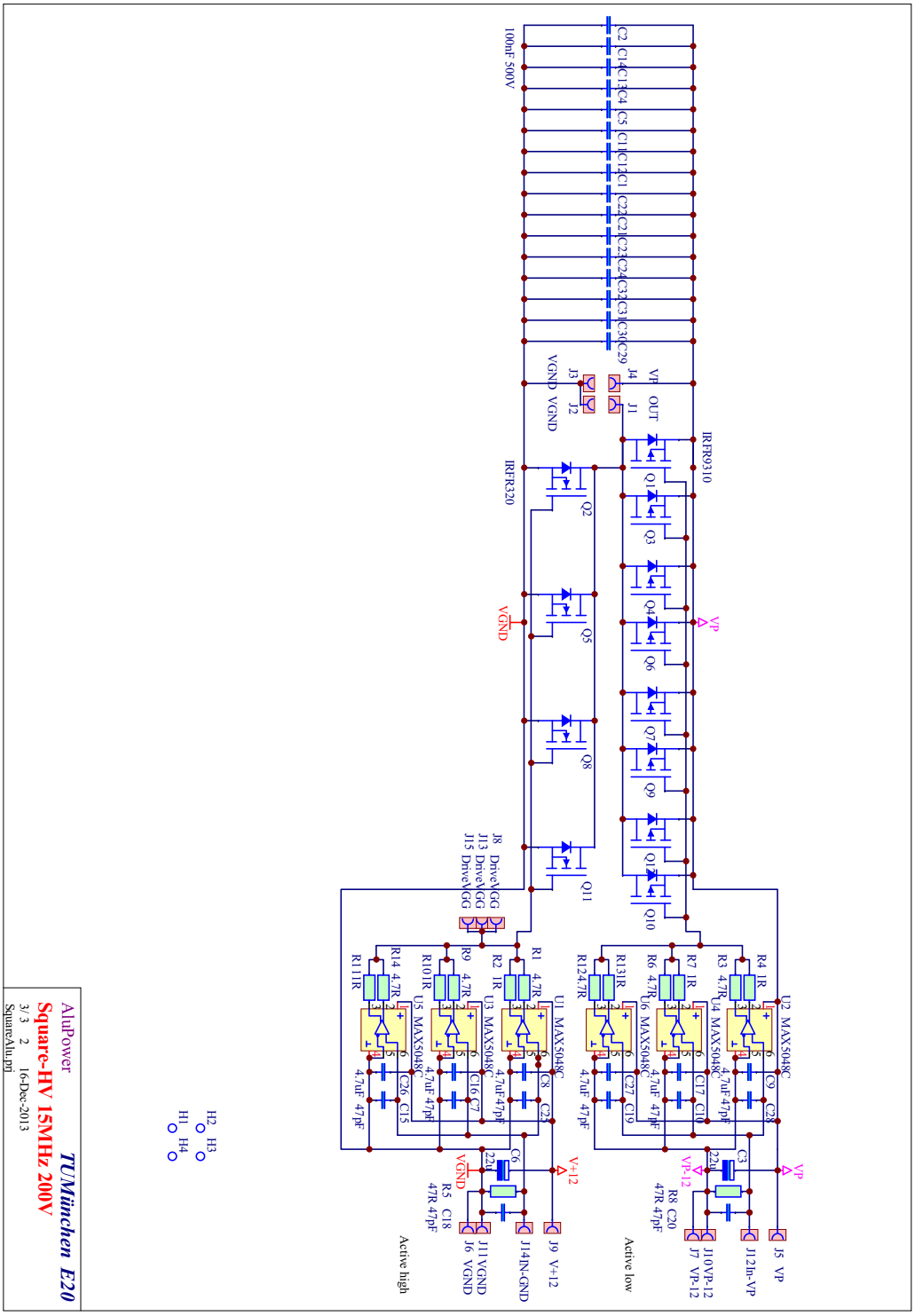

Figure B.7: Wiring diagram of the RF booster's signal boosting board.

B.3 High Voltage Board

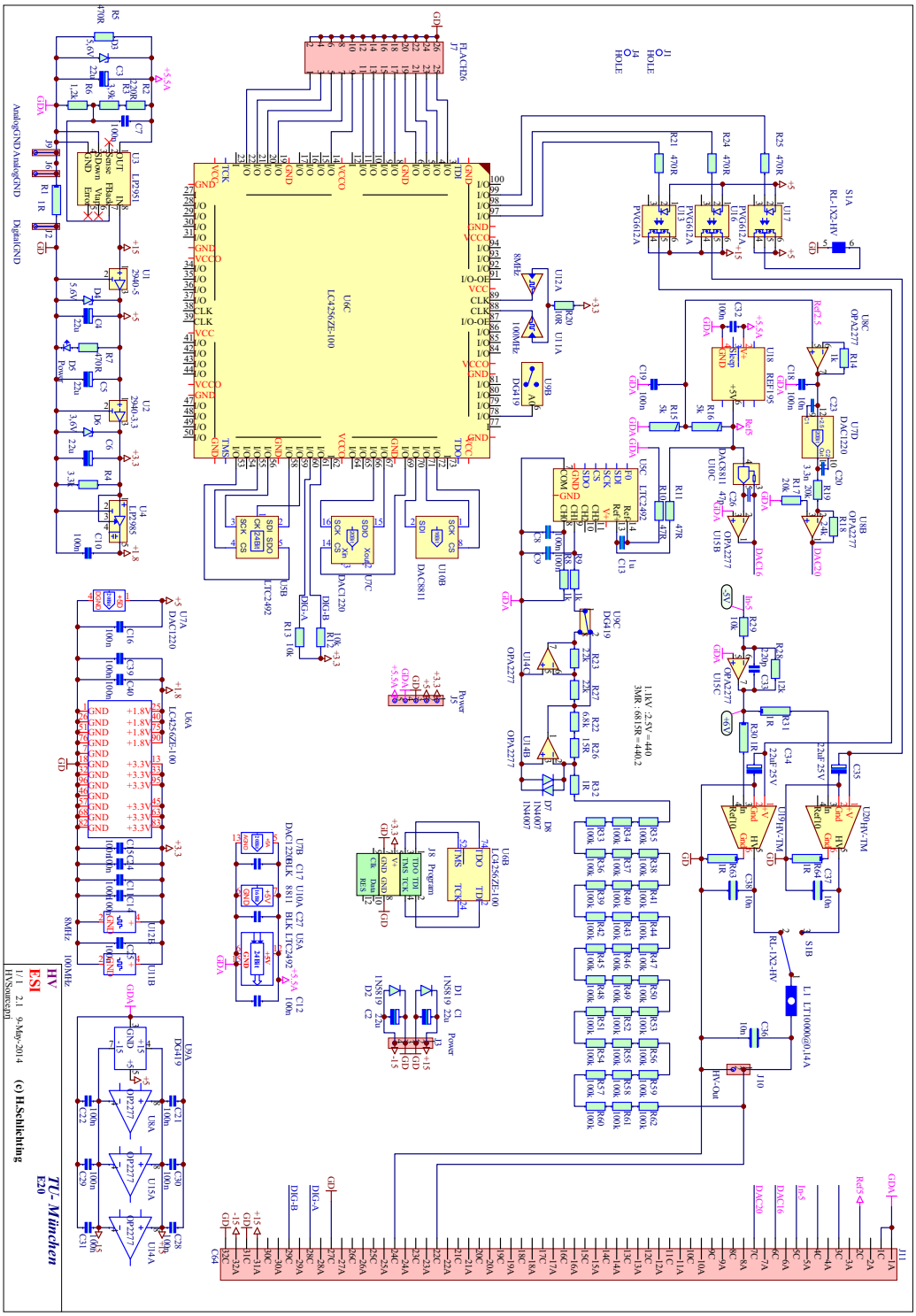

Figure B.8: Wiring diagram of the high voltage board.

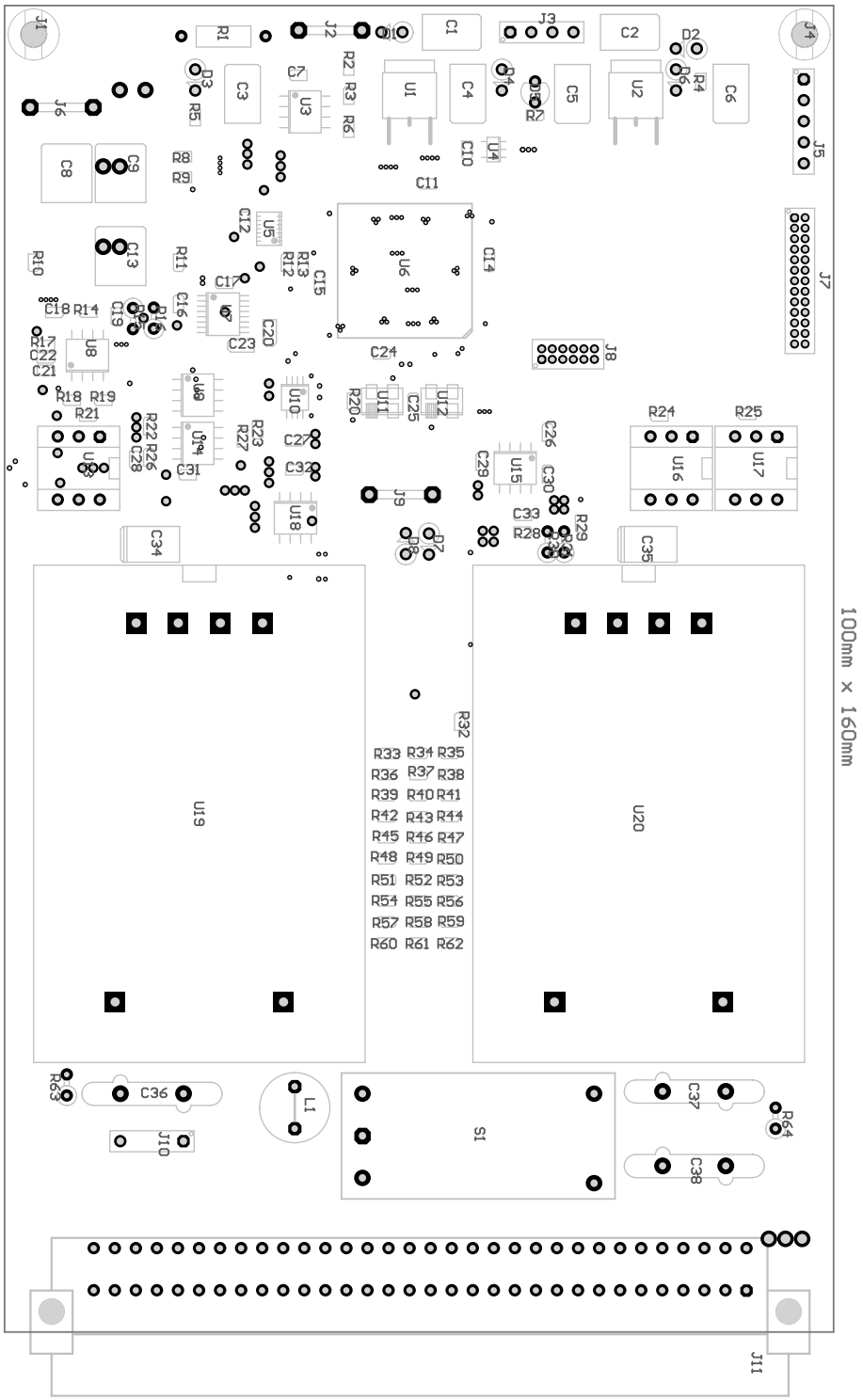

Figure B.9: PCB layout of the high voltage board.

B.4 Current Detect Board

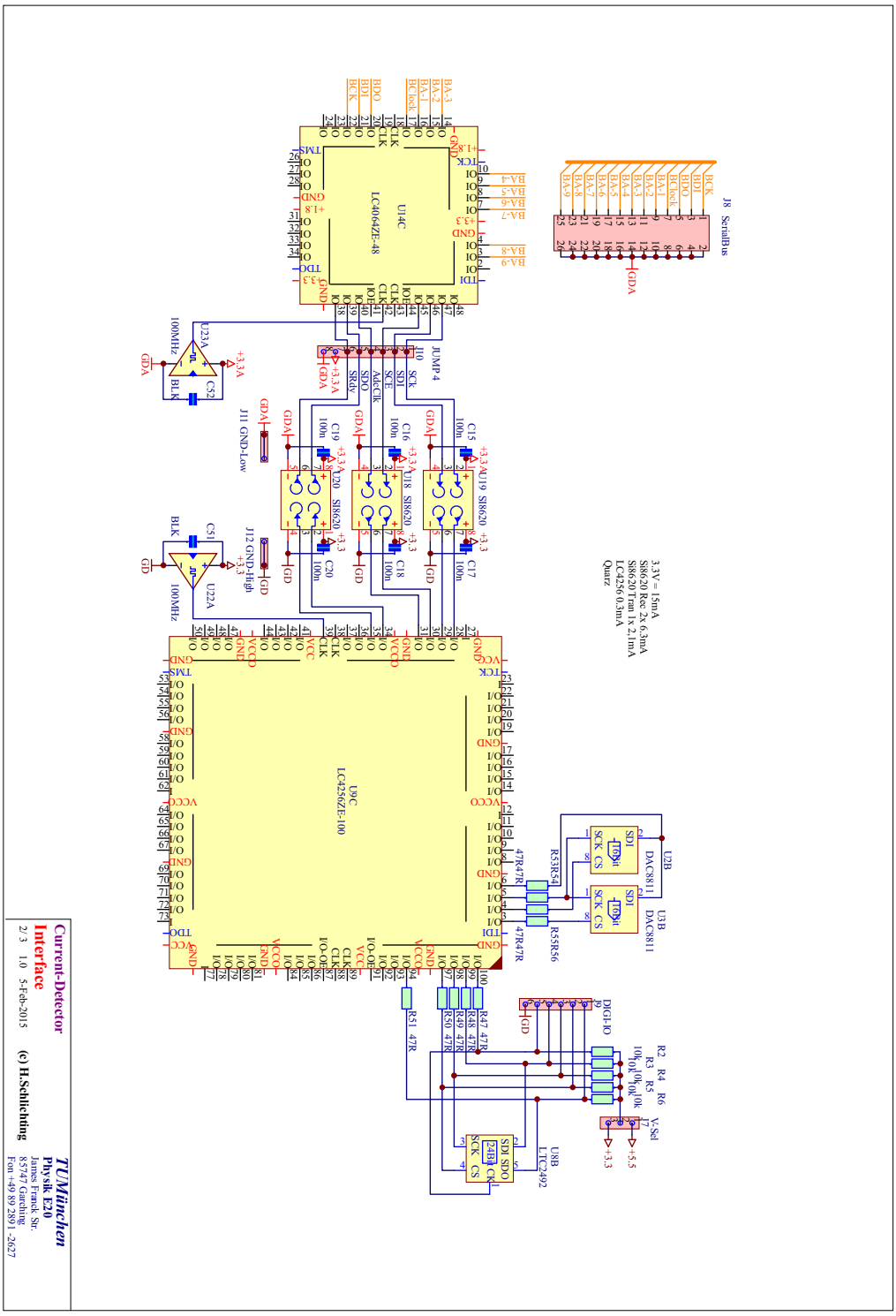

Figure B.10: Digital wiring diagram of the current detect board.

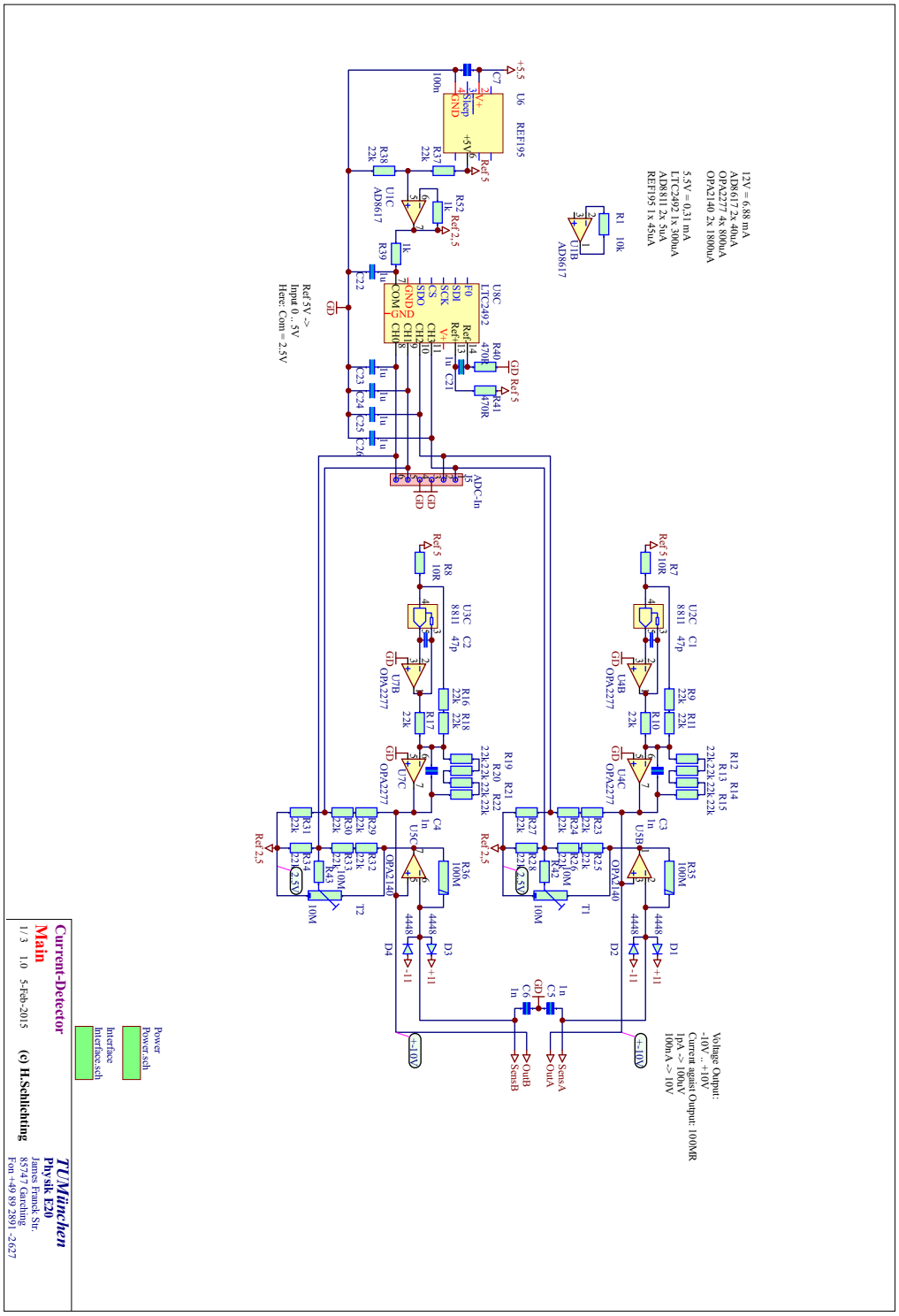

Figure B.11: Analog wiring diagram of the current detect board.

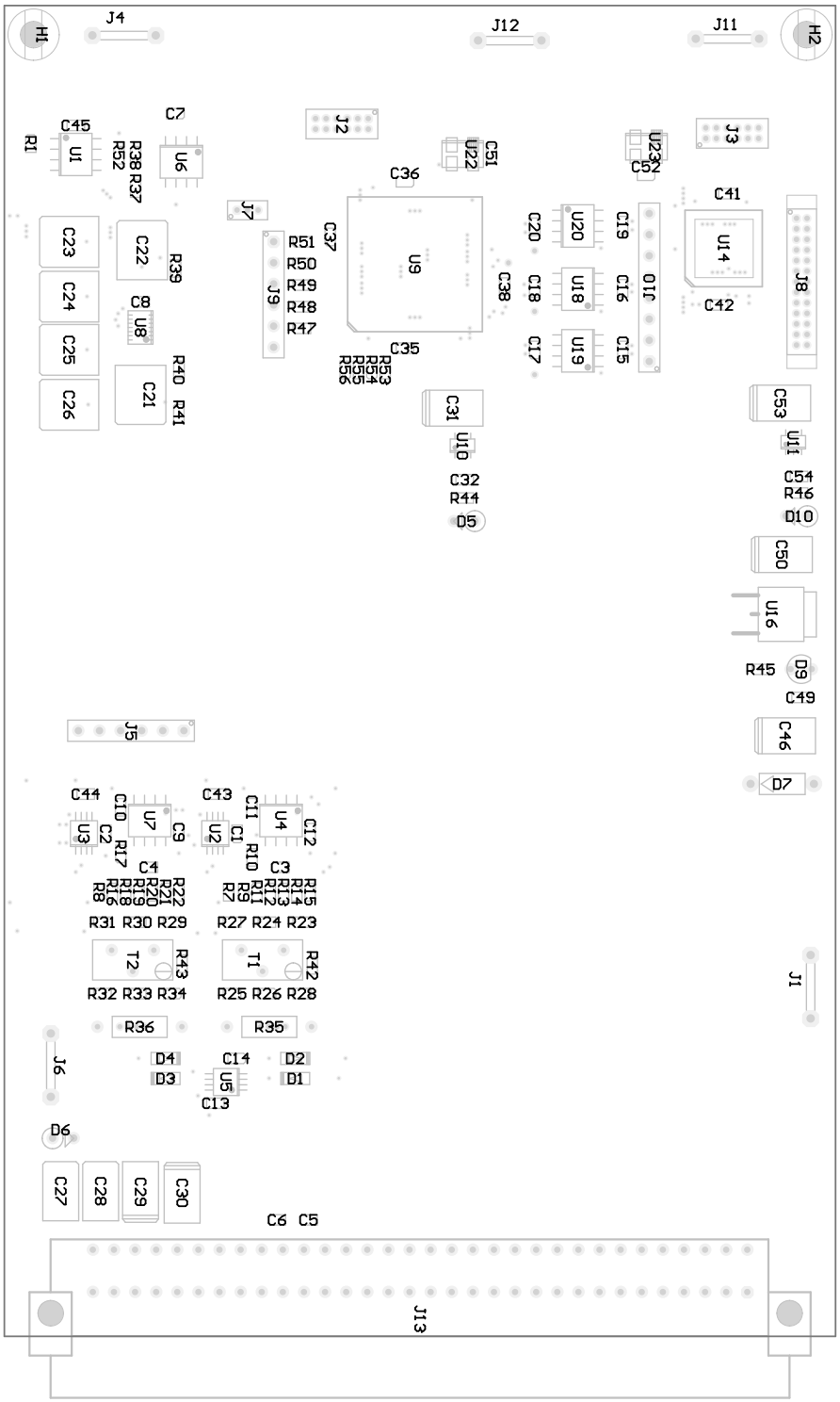

Figure B.12: PCB layout of the current detect board.

B.5 Solar Power Board

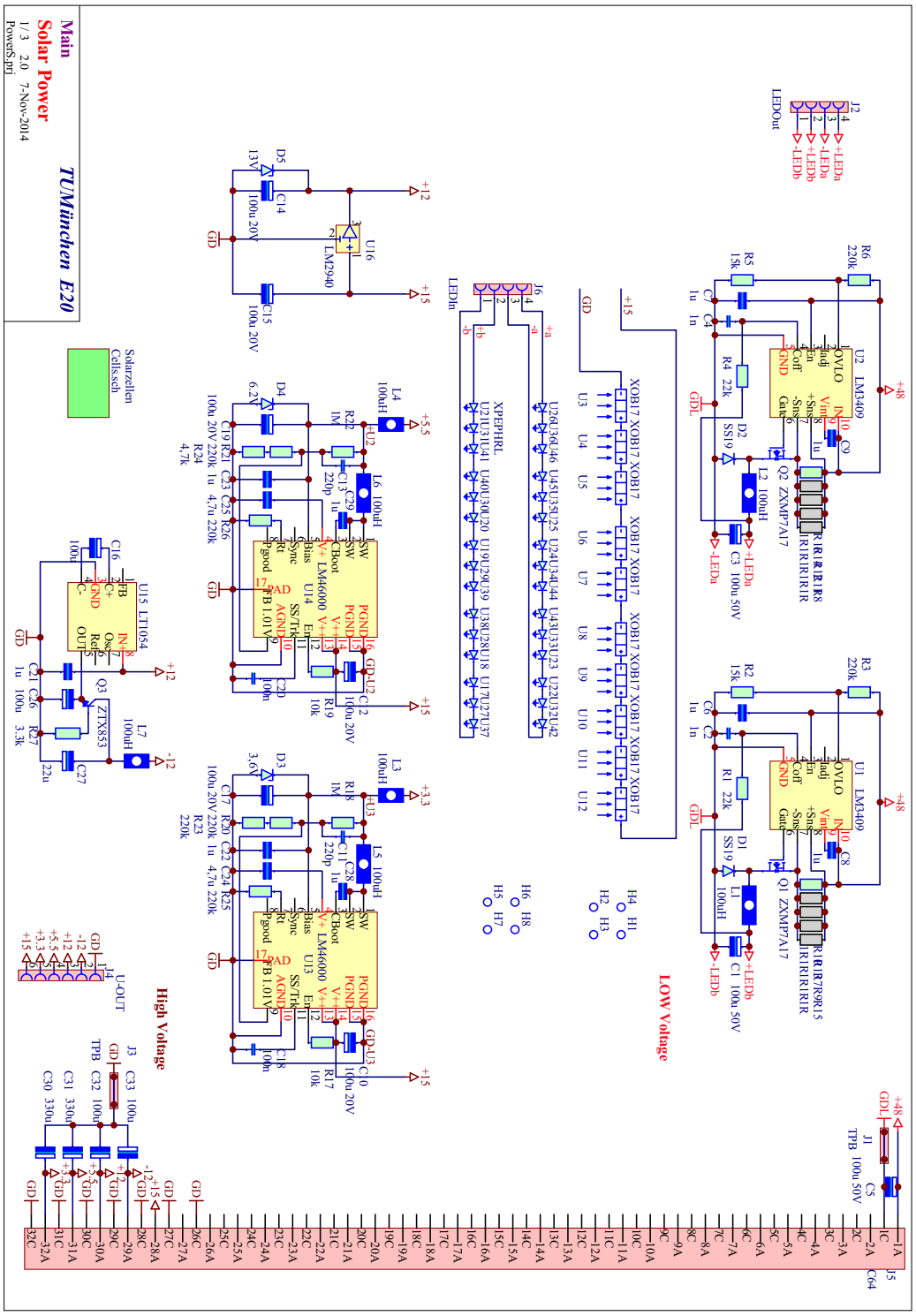

Figure B.13: Wiring diagram of the solar power board.

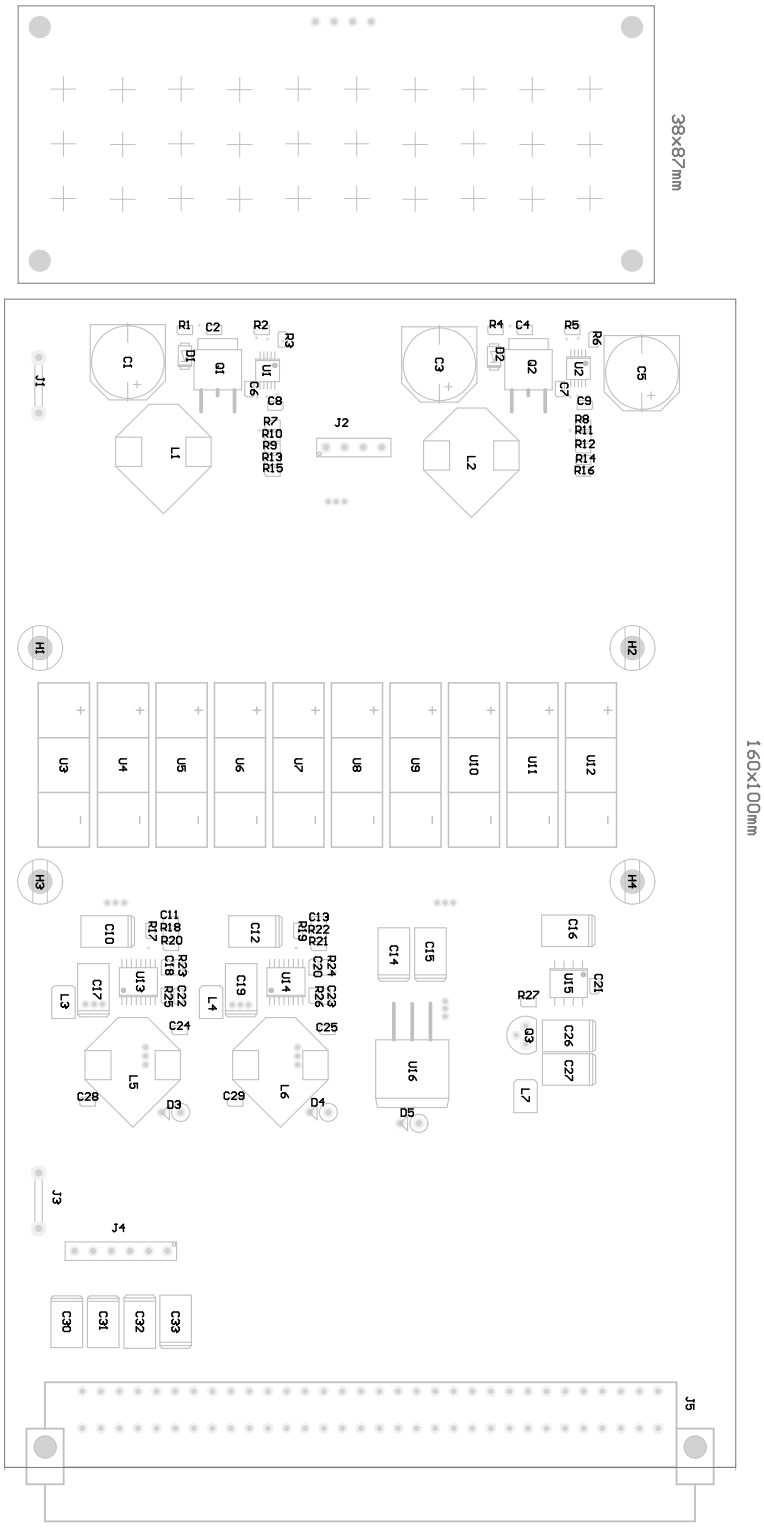

Figure B.14: PCB layout of the solar power board.

References

[1] Binnig, G, et al. Tunneling through a controllable vacuum gap. *Applied Physics Letters*, 40(2):178–180, 1982. doi:10.1063/1.92999 1, 6

[2] Binnig, G, et al. Surface Studies by Scanning Tunneling Microscopy. *Physical Review Letters*, 49(1):57–61, 1982. doi:10.1103/PhysRevLett.49.57 1, 6

[3] Kroto, HW, et al. C 60: buckminsterfullerene. *Nature*, 318(6042):162–163, 1985 1

[4] Moore, GE. Lithography and the future of Moore's law. vol. 2440, pp. 2–17. 1995. doi:10.1117/12.209244 1

[5] Schaller, RR. Moore's law: past, present and future. *IEEE Spectrum*, 34(6):52–59, 1997. doi:10.1109/6.591665 1

[6] Langmuir, I. Forces Near the Surfaces of Molecules. *Chemical Reviews*, 6(4):451–479, 1930. doi:10.1021/cr60024a002 1

[7] Lennard-Jones, J. Processes of adsorption and diffusion on solid surfaces. *Transactions of the Faraday Society*, 28:333–359, 1932 1

[8] Feynman, RP. There's plenty of room at the bottom. *Engineering and science*, 23(5):22–36, 1960 1

[9] Toumey, CP. Reading Feynman into nanotechnology. *Techné: Research in Philosophy and Technology*, 12(3):133–168, 2008 1

[10] James, SL. Metal-organic frameworks. *Chemical Society Reviews*, 32(5):276, 2003. doi:10.1039/b200393g 1

[11] Schlögl, R and Abd Hamid, SB. Nanocatalysis: Mature Science Revisited or Something Really New? *Angewandte Chemie International Edition*, 43(13):1628–1637, 2004. doi:10.1002/anie.200301684 1

[12] Zhou, K and Li, Y. Catalysis Based on Nanocrystals with Well-Defined Facets. *Angewandte Chemie International Edition*, 51(3):602–613, 2012. doi:10.1002/anie.201102619 1

[13] Li, X, et al. An All-Optical Quantum Gate in a Semiconductor Quantum Dot. *Science*, 301(5634):809–811, 2003. doi:10.1126/science.1083800 1

[14] Maune, BM, et al. Coherent singlet-triplet oscillations in a silicon-based double quantum dot. *Nature*, 481(7381):344–347, 2012. doi:10.1038/nature10707 1

[15] Wolf, SA, et al. Spintronics: A Spin-Based Electronics Vision for the Future. *Science*, 294(5546):1488–1495, 2001. doi:10.1126/science.1065389 1

[16] Awschalom, DD and Flatté, ME. Challenges for semiconductor spintronics. *Nature Physics*, 3(3):153–159, 2007. doi:10.1038/nphys551 1

[17] Bogani, L and Wernsdorfer, W. Molecular spintronics using single-molecule magnets. *Nature Materials*, 7(3):179–186, 2008. doi:10.1038/nmat2133 1, 31

[18] Sauvage, J and Amendola, V. *Molecular Machines and Motors*. No. Bd. 99 in Molecular machines and motors. Springer, 2001 1

[19] Shirai, Y, et al. Directional Control in Thermally Driven Single-Molecule Nanocars. *Nano Letters*, 5(11):2330–2334, 2005. doi:10.1021/nl051915k 1

[20] Kudernac, T, et al. Electrically driven directional motion of a four-wheeled molecule on a metal surface. *Nature*, 479(7372):208–211, 2011. doi:10.1038/nature10587 1

[21] Bhushan, B. Nanotribology and nanomechanics. *Wear*, 259(7–12):1507–1531, 2005. doi:10.1016/j.wear.2005.01.010 1

[22] Gebeshuber, IC, Stachelberger, H, and Drack, M. Diatom Bionanotribology - Biological Surfaces in Relative Motion: Their Design, Friction, Adhesion, Lubrication and Wear. *Journal of Nanoscience and Nanotechnology*, 5(1):79–87, 2005. doi:10.1166/jnn.2005.018 1

[23] Yoon, B, et al. Hydrogen-bonded structure and mechanical chiral response of a silver nanoparticle superlattice. *Nature Materials*, 13(8):807–811, 2014. doi:10.1038/nmat3923 2

[24] Barth, JV. Molecular Architectonic on Metal Surfaces. *Annual Review of Physical Chemistry*, 58(1):375–407, 2007. doi:10.1146/annurev.physchem.56.092503.141259 2

[25] Henzie, J, et al. Large-Area Nanoscale Patterning: Chemistry Meets Fabrication. *Accounts of Chemical Research*, 39(4):249–257, 2006. doi:10.1021/ar050013n 2

[26] Kuemmel, M, et al. A Chemical Solution Deposition Route To Nanopatterned Inorganic Material Surfaces. *Chemistry of Materials*, 19(15):3717–3725, 2007. doi:10.1021/cm0706245 2

[27] Ghosh, AW, Rakshit, T, and Datta, S. Gating of a Molecular Transistor: Electrostatic and Conformational. *Nano Letters*, 4(4):565–568, 2004. doi:10.1021/nl035109u 2

[28] Stauth, SA and Parviz, BA. Self-assembled single-crystal silicon circuits on plastic. *Proceedings of the National Academy of Sciences*, 103(38):13922–13927, 2006. doi:10.1073/pnas.0602893103 2

[29] Engel, M, et al. Thin Film Nanotube Transistors Based on Self-Assembled, Aligned, Semiconducting Carbon Nanotube Arrays. *ACS Nano*, 2(12):2445–2452, 2008. doi:10.1021/nn800708w 2

[30] Barlow, SM and Raval, R. Complex organic molecules at metal surfaces: bonding, organisation and chirality. *Surface Science Reports*, 50(6–8):201–341, 2003. doi:10.1016/S0167-5729(03)00015-3 2

[31] Rosei, F, et al. Properties of large organic molecules on metal surfaces. *Progress in Surface Science*, 71(5–8):95–146, 2003. doi:10.1016/S0079-6816(03)00004-2 2

[32] Lindner, R and Kühnle, A. On-Surface Reactions. *ChemPhysChem*, 16(8):1582–1592, 2015. doi:10.1002/cphc.201500161 2

[33] Ariga, K, et al. Challenges and breakthroughs in recent research on self-assembly. *Science and Technology of Advanced Materials*, 9(1):014109, 2008. doi:10.1088/1468-6996/9/1/014109 2

[34] Whitelam, S and Jack, RL. The Statistical Mechanics of Dynamic Pathways to Self-assembly. *Annual Review of Physical Chemistry*, 66(1):143–163, 2015. doi:10.1146/annurev-physchem-040214-121215. ArXiv: 1407.2505 2

[35] Forrest, SR. Ultrathin Organic Films Grown by Organic Molecular Beam Deposition and Related Techniques. *Chemical Reviews*, 97(6):1793–1896, 1997. doi:10.1021/cr941014o 3, 13

[36] Hoenig, M and de Kersabiec, AM. Sample preparation steps for analysis by atomic spectroscopy methods: present status. *Spectrochimica Acta Part B: Atomic Spectroscopy*, 51(11):1297–1307, 1996. doi:10.1016/0584-8547(96)01507-8 5

[37] Oliveira, Ed. Sample preparation for atomic spectroscopy: evolution and future trends. *Journal of the Brazilian Chemical Society*, 14(2):174–182, 2003. doi:10.1590/S0103-50532003000200004 5

[38] Mitra, S. *Sample preparation techniques in analytical chemistry*, vol. 237. John Wiley & Sons, 2004 5

[39] Sneddon, J, et al. Sample Preparation of Solid Samples for Metal Determination by Atomic Spectroscopy—An Overview and Selected Recent Applications. *Applied Spectroscopy Reviews*, 41(1):1–14, 2006. doi:10.1080/05704920500385445 5

[40] Rao, CNR, et al. Graphene: The New Two-Dimensional Nanomaterial. *Angewandte Chemie International Edition*, 48(42):7752–7777, 2009. doi:10.1002/anie.200901678 5

[41] Radisavljevic, B, et al. Single-layer MoS2 transistors. *Nature Nanotechnology*, 6(3):147–150, 2011. doi:10.1038/nnano.2010.279 5

[42] Lyn, JA, et al. Measurement uncertainty from physical sample preparation: estimation including systematic error. *The Analyst*, 128(11):1391, 2003. doi:10.1039/b307581h 5

[43] Meyer, E, Hug, HJ, and Bennewitz, R. *Scanning probe microscopy: the lab on a tip*. Springer Science & Business Media, 2013 5, 6, 7, 8

[44] Stroscio, J, et al. *Scanning Tunneling Microscopy*. Methods of Experimental Physics. Elsevier Science, 2013 5

[45] Rohrer, H. STM: 10 years after. *Ultramicroscopy*, 42:1–6, 1992. doi:10.1016/0304-3991(92)90239-G 6

[46] Hund, F. Zur Deutung der Molekelspektren. III. *Zeitschrift für Physik*, 43(11-12):805–826, 1927. doi:10.1007/BF01397249 6

[47] Gamow, G. Zur Quantentheorie des Atomkernes. *Zeitschrift für Physik*, 51(3-4):204–212, 1928. doi:10.1007/BF01343196 6

[48] Gurney, RW and Condon, EU. Wave mechanics and radioactive disintegration. *Nature*, 122(3073):439, 1928 6

[49] Jeffreys, H. On Certain Approximate Solutions of Lineae Differential Equations of the Second Order. *Proceedings of the London Mathematical Society*, s2-23(1):428–436, 1925. doi:10.1112/plms/s2-23.1.428 6

[50] Wentzel, G. Eine Verallgemeinerung der Quantenbedingungen für die Zwecke der Wellenmechanik. *Zeitschrift für Physik*, 38(6-7):518–529, 1926. doi:10.1007/BF01397171 6

[51] Kramers, HA. Wellenmechanik und halbzahlige Quantisierung. *Zeitschrift für Physik*, 39(10-11):828–840, 1926. doi:10.1007/BF01451751 6

[52] Brillouin, L. La mécanique ondulatoire de Schrödinger; une méthode générale de résolution par approximations successives. *CR Acad Sci*, 183(11):24–26, 1926 6

[53] Fowler, RH and Nordheim, L. Electron Emission in Intense Electric Fields. *Proceedings of the Royal Society of London A: Mathematical, Physical and Engineering Sciences*, 119(781):173–181, 1928. doi:10.1098/rspa.1928.0091 6

[54] Frenkel, J. On the Electrical Resistance of Contacts between Solid Conductors. *Physical Review*, 36(11):1604–1618, 1930. doi:10.1103/PhysRev.36.1604 6

[55] Holm, R. The Electric Tunnel Effect across Thin Insulator Films in Contacts. *Journal of Applied Physics*, 22(5):569–574, 1951. doi:10.1063/1.1700008 6

[56] Esaki, L. New Phenomenon in Narrow Germanium $p - n$ Junctions. *Physical Review*, 109(2):603–604, 1958. doi:10.1103/PhysRev.109.603 7

[57] Giaever, I. Electron Tunneling Between Two Superconductors. *Physical Review Letters*, 5(10):464–466, 1960. doi:10.1103/PhysRevLett.5.464 7

[58] Giaever, I. Energy Gap in Superconductors Measured by Electron Tunneling. *Physical Review Letters*, 5(4):147–148, 1960. doi:10.1103/PhysRevLett.5.147 7

[59] Young, R, Ward, J, and Scire, F. Observation of Metal-Vacuum-Metal Tunneling, Field Emission, and the Transition Region. *Physical Review Letters*, 27(14):922–924, 1971. doi:10.1103/PhysRevLett.27.922 7

[60] Giaever, I. Nobel Lecture: Electron Tunneling and Superconductivity. In S Lundqvist, editor, *Nobel Lectures, Physics 1971-1980*. World Scientific Publishing Co., Singapore, 1992 7

[61] Young, R, Ward, J, and Scire, F. The Topografiner: An Instrument for Measuring Surface Microtopography. *Review of Scientific Instruments*, 43(7):999–1011, 1972. doi:10.1063/1.1685846 7

[62] Wiesendanger, R. *Scanning Probe Microscopy and Spectroscopy: Methods and Applications*. Cambridge University Press, 1994 7

[63] Tersoff, J and Hamann, DR. Theory and Application for the Scanning Tunneling Microscope. *Physical Review Letters*, 50(25):1998–2001, 1983. doi:10.1103/PhysRevLett.50.1998 8

[64] Tersoff, J and Hamann, DR. Theory of the scanning tunneling microscope. In H Neddermeyer, editor, *Scanning Tunneling Microscopy*, no. 6 in Perspectives in Condensed Matter Physics, pp. 59–67. Springer Netherlands, 1985. DOI: 10.1007/978-94-011-1812-5_5 8

[65] Ohnishi, S and Tsukada, M. Molecular orbital theory for the scanning tunneling microscopy. *Solid State Communications*, 71(5):391–394, 1989. doi:10.1016/0038-1098(89)90777-1 8

[66] Chen, CJ. Effects of m $\neq$ 0 tip states in scanning tunneling microscopy: The explanations of corrugation reversal. *Physical Review Letters*, 69(11):1656–1659, 1992. doi:10.1103/PhysRevLett.69.1656 8

[67] Chen, CJ. *Introduction to scanning tunneling microscopy*. Oxford University Press, 2008 8

[68] CreaTec Fischer & Co. GmbH, E, Industriestr. 9. www.createc.de 8, 9

[69] Binnig, G and Smith, DPE. Single-tube three-dimensional scanner for scanning tunneling microscopy. *Review of Scientific Instruments*, 57(8):1688–1689, 1986. doi:10.1063/1.1139196 8

[70] Renner, C, et al. A vertical piezoelectric inertial slider. *Review of Scientific Instruments*, 61(3):965–967, 1990. doi:10.1063/1.1141450 8

[71] Pohl, DW. Some design criteria in scanning tunneling microscopy. *IBM Journal of Research and Development*, 30(4):417–427, 1986. doi:10.1147/rd.304.0417 8

[72] Holmes, M, Hocken, R, and Trumper, D. The long-range scanning stage: a novel platform for scanned-probe microscopy. *Precision Engineering*, 24(3):191–209, 2000. doi:10.1016/S0141-6359(99)00044-6 8

[73] MacLeod, JM, et al. Two linear beetle-type scanning tunneling microscopes. *Review of Scientific Instruments*, 74(4):2429–2437, 2003. doi:10.1063/1.1544423 8

[74] Meyer, G, Zöphel, S, and Rieder, KH. Scanning Tunneling Microscopy Manipulation of Native Substrate Atoms: A New Way to Obtain Registry Information on Foreign Adsorbates. *Physical Review Letters*, 77(10):2113–2116, 1996. doi:10.1103/PhysRevLett.77.2113 8, 35

[75] Seufert, KJ. *Nanochemistry with porphyrins - a 2D perspective*. Dissertation, Technische Universität München, München, 2011 9, 11

[76] Wiengarten, AC. *Scanning tunneling microscopy investigation of structure and electronic properties of surface-confined tetrapyrrolic species*. Ph.D. thesis, Technische Universität München, 2015 9, 56

[77] SPECS Surface Nano Analysis GmbH, B, Voltastrasse 5. www.specs.de 9

[78] Fischer, S. *Combined STM and X-ray spectroscopy study of surface-confined biologically relevant molecules*. Ph.D. thesis, Technische Universität München, 2013 9, 60

[79] Oh, SC. *Single layer films of functional molecules on noble metal surfaces visited by scanning tunneling microscopy and X-ray spectroscopy*. Ph.D. thesis, Technische Universität München, 2014 9, 60

[80] Stirling, J. Control theory for scanning probe microscopy revisited. *Beilstein Journal of Nanotechnology*, 5:337–345, 2014. doi:10.3762/bjnano.5.38 9, 10

[81] Rabe, JP and Buchholz, S. Commensurability and Mobility in Two-Dimensional Molecular Patterns on Graphite. *Science*, 253(5018):424–427, 1991. doi:10.1126/science.253.5018.424 11

[82] Tait, SL, et al. One-dimensional self-assembled molecular chains on Cu (100): Interplay between surface-assisted coordination chemistry and substrate commensurability. *The Journal of Physical Chemistry C*, 111(29):10982–10987, 2007 11

[83] Hara, M, et al. Epitaxial Growth of Organic Thin Films by Organic Molecular Beam Epitaxy. *Japanese Journal of Applied Physics*, 28(Part 2, No. 2):L306–L308, 1989. doi:10.1143/JJAP.28.L306 13

[84] So, FF, et al. Quasi-epitaxial growth of organic multiple quantum well structures by organic molecular beam deposition. *Applied Physics Letters*, 56(7):674–676, 1990. doi:10.1063/1.102733 13

[85] Schreiber, F. Organic molecular beam deposition: Growth studies beyond the first monolayer. *physica status solidi (a)*, 201(6):1037–1054, 2004. doi:10.1002/pssa.200404334 13

[86] Vestal, ML. Methods of Ion Generation. *Chemical Reviews*, 101(2):361–376, 2001. doi:10.1021/cr990104w 15

[87] McEwen, CN and Larsen, BS. Fifty years of desorption ionization of nonvolatile compounds. *International Journal of Mass Spectrometry*, 377:515–531, 2015. doi:10.1016/j.ijms.2014.07.018 15

[88] Cole, R. *Electrospray and MALDI Mass Spectrometry: Fundamentals, Instrumentation, Practicalities, and Biological Applications*. Wiley, 2011 15

[89] Plateau, J. Mémoire sur les phénomènes que présente une masse liquide et soustraite à l'action de la pesanteur. *Nouveaux mémoires de l'Académie Royale des Sciences et Belles-Lettres de Bruxelles*, 16:1, 1843 16

[90] Rayleigh, L. On the Capillary Phenomena of Jets. *Proceedings of the Royal Society of London Series I*, 29:71–97, 1879 16

[91] Rayleigh, L. XX. On the equilibrium of liquid conducting masses charged with electricity. *The London, Edinburgh, and Dublin Philosophical Magazine and Journal of Science*, 14(87):184–186, 1882 16, 18

[92] Zeleny, J. The Electrical Discharge from Liquid Points, and a Hydrostatic Method of Measuring the Electric Intensity at Their Surfaces. *Physical Review*, 3(2):69–91, 1914. doi:10.1103/PhysRev.3.69 16

[93] Zeleny, J. Instability of Electrified Liquid Surfaces. *Physical Review*, 10(1):1–6, 1917. doi:10.1103/PhysRev.10.1 16

[94] Wilson, CTR and Taylor, GI. The bursting of soap-bubbles in a uniform electric field. *Mathematical Proceedings of the Cambridge Philosophical Society*, 22(05):728–730, 1925. doi:10.1017/S0305004100009609 16

[95] Macky, WA. Some Investigations on the Deformation and Breaking of Water Drops in Strong Electric Fields. *Proceedings of the Royal Society of London A: Mathematical, Physical and Engineering Sciences*, 133(822):565–587, 1931. doi:10.1098/rspa.1931.0168 16

[96] Taylor, G. Disintegration of Water Drops in an Electric Field. *Proceedings of the Royal Society of London A: Mathematical, Physical and Engineering Sciences*, 280(1382):383–397, 1964. doi:10.1098/rspa.1964.0151 16

[97] Taylor, GI and McEwan, AD. The stability of a horizontal fluid interface in a vertical electric field. *Journal of Fluid Mechanics*, 22(01):1–15, 1965. doi:10.1017/S0022112065000538 16

[98] Taylor, G. The Force Exerted by an Electric Field on a Long Cylindrical Conductor. *Proceedings of the Royal Society of London A: Mathematical, Physical and Engineering Sciences*, 291(1425):145–158, 1966. doi:10.1098/rspa.1966.0085 16

[99] Taylor, G. Electrically Driven Jets. *Proceedings of the Royal Society of London A: Mathematical, Physical and Engineering Sciences*, 313(1515):453–475, 1969. doi:10.1098/rspa.1969.0205 16

[100] Dole, M, et al. Molecular Beams of Macroions. *The Journal of Chemical Physics*, 49(5):2240–2249, 1968. doi:10.1063/1.1670391 16

[101] Yamashita, M and Fenn, JB. Electrospray ion source. Another variation on the free-jet theme. *The Journal of Physical Chemistry*, 88(20):4451–4459, 1984. doi:10.1021/j150664a002 16

[102] Yamashita, M and Fenn, JB. Negative ion production with the electrospray ion source. *The Journal of Physical Chemistry*, 88(20):4671–4675, 1984. doi:10.1021/j150664a046 16

[103] Fenn, JB, et al. Electrospray ionization for mass spectrometry of large biomolecules. *Science*, 246(4926):64–71, 1989. doi:10.1126/science.2675315 16

[104] Carswell, DJ and Milsted, J. A new method for the preparation of thin films of radioactive material of thin films of radioactive material. *Journal of Nuclear Energy (1954)*, 4(1):51–54, 1957. doi:10.1016/0891-3919(57)90115-8 16

[105] Hoyer, B, et al. Electrostatic Spraying: A Novel Technique for Preparation of Polymer Coatings on Electrodes. *Analytical Chemistry*, 68(21):3840–3844, 1996. doi:10.1021/ac9605509 16

[106] Morozov, VN and Morozova, TY. Electrospray Deposition as a Method for Mass Fabrication of Mono- and Multicomponent Microarrays of Biological and Biologically Active Substances. *Analytical Chemistry*, 71(15):3110–3117, 1999. doi:10.1021/ac981412h 16

[107] Morozov, VN and Morozova, TY. Electrospray Deposition as a Method To Fabricate Functionally Active Protein Films. *Analytical Chemistry*, 71(7):1415–1420, 1999. doi:10.1021/ac9808775 16

[108] Rauschenbach, S, et al. Electrospray Ion Beam Deposition of Clusters and Biomolecules. *Small*, 2(4):540–547, 2006. doi:10.1002/smll.200500479 16

[109] Walz, A. *Design and Optimization of Transmission Performance in an ESIBD System*. Master's thesis, Technische Universität München, 2015 17, 59, 69, 71, 77, 79, 80, 81, 82, 95

[110] Wilm, MS and Mann, M. Electrospray and Taylor-Cone theory, Dole's beam of macromolecules at last? *International Journal of Mass Spectrometry and Ion Processes*, 136(2):167–180, 1994. doi:10.1016/0168-1176(94)04024-9 17

[111] Cloupeau, M and Prunet-Foch, B. Electrohydrodynamic spraying functioning modes: a critical review. *Journal of Aerosol Science*, 25(6):1021–1036, 1994. doi:10.1016/0021-8502(94)90199-6 17

[112] Juraschek, R and Röllgen, FW. Pulsation phenomena during electrospray ionization. *International Journal of Mass Spectrometry*, 177(1):1–15, 1998. doi:10.1016/S1387-3806(98)14025-3 17

[113] Nemes, P, Marginean, I, and Vertes, A. Spraying Mode Effect on Droplet Formation and Ion Chemistry in Electrosprays. *Analytical Chemistry*, 79(8):3105–3116, 2007. doi:10.1021/ac062382i 17, 18

[114] Konermann, L, Silva, EA, and Sogbein, OF. Electrochemically Induced pH Changes Resulting in Protein Unfolding in the Ion Source of an Electrospray Mass Spectrometer. *Analytical Chemistry*, 73(20):4836–4844, 2001. doi:10.1021/ac010545r 17

[115] Rohner, TC, Lion, N, and Girault, HH. Electrochemical and theoretical aspects of electrospray ionisation. *Physical Chemistry Chemical Physics*, 6(12):3056–3068, 2004. doi:10.1039/B316836K 17

[116] Duft, D, et al. Coulomb fission: Rayleigh jets from levitated microdroplets. *Nature*, 421(6919):128–128, 2003. doi:10.1038/421128a 17

[117] Labowsky, M, Fenn, JB, and Fernandez de la Mora, J. A continuum model for ion evaporation from a drop: effect of curvature and charge on ion solvation energy. *Analytica Chimica Acta*, 406(1):105–118, 2000. doi:10.1016/S0003-2670(99)00595-4 19

[118] Kebarle, P and Peschke, M. On the mechanisms by which the charged droplets produced by electrospray lead to gas phase ions. *Analytica Chimica Acta*, 406(1):11–35, 2000. doi:10.1016/S0003-2670(99)00598-X 19

[119] Fernandez de la Mora, J. Electrospray ionization of large multiply charged species proceeds via Dole's charged residue mechanism. *Analytica Chimica Acta*, 406(1):93–104, 2000. doi:10.1016/S0003-2670(99)00601-7 19

[120] Konermann, L, et al. Unraveling the Mechanism of Electrospray Ionization. *Analytical Chemistry*, 85(1):2–9, 2013. doi:10.1021/ac302789c 19

[121] Iribarne, JV and Thomson, BA. On the evaporation of small ions from charged droplets. *The Journal of Chemical Physics*, 64(6):2287–2294, 1976. doi:10.1063/1.432536 19

[122] Gomez, A and Tang, K. Charge and fission of droplets in electrostatic sprays. *Physics of Fluids (1994-present)*, 6(1):404–414, 1994. doi:10.1063/1.868037 19

[123] Hogan, CJ, et al. Combined Charged Residue-Field Emission Model of Macromolecular Electrospray Ionization. *Analytical Chemistry*, 81(1):369–377, 2009. doi:10.1021/ac8016532 20

[124] Konermann, L, Rodriguez, AD, and Liu, J. On the Formation of Highly Charged Gaseous Ions from Unfolded Proteins by Electrospray Ionization. *Analytical Chemistry*, 84(15):6798–6804, 2012. doi:10.1021/ac301298g 20

[125] Busch, H. Berechnung der Bahn von Kathodenstrahlen im axialsymmetrischen elektromagnetischen Felde. *Annalen der Physik*, 386(25):974–993, 1926. doi:10.1002/andp.19263862507 20

[126] Gans, R. Electron Paths in Electron-Optical Systems. *Z tech Physik*, 18:41–48, 1937 20

[127] Gray, F. Electrostatic Electron-Optics. *Bell System Technical Journal*, 18(1):1–31, 1939. doi:10.1002/j.1538-7305.1939.tb00805.x 20

[128] Paul, W and Steinwedel, H. Notizen: Ein neues Massenspektrometer ohne Magnetfeld. *Zeitschrift für Naturforschung A*, 8(7):448–450, 1953 20

[129] Paul, W, Reinhard, HP, and Zahn, Uv. Das elektrische Massenfilter als Massenspektrometer und Isotopentrenner. *Zeitschrift für Physik*, 152(2):143–182, 1958. doi:10.1007/BF01327353 20

[130] Dawson, P. Quadrupole mass analyzers: performance, design and some recent applications. *Mass Spectrometry Reviews*, 5(1):1–37, 1986 20, 25

[131] Dawson, PH. *Quadrupole Mass Spectrometry and Its Applications*. Elsevier, 1976 20, 30

[132] Osovets, SM. Use of high-frequency electromagnetic fields for plasma containment and stabilization. *Journal of Nuclear Energy Part C, Plasma Physics, Accelerators, Thermonuclear Research*, 6(4):421, 1964. doi:10.1088/0368-3281/6/4/308 20

[133] Rosenzweig, J and Serafini, L. Transverse particle motion in radio-frequency linear accelerators. *Physical Review E*, 49(2):1599–1602, 1994. doi:10.1103/PhysRevE.49.1599 20

[134] Reiser, M. *Theory and Design of Charged Particle Beams*. Wiley Series in Beam Physics and Accelerator Technology. Wiley, 2008 20

[135] Heddle, D. *Electrostatic Lens Systems, 2nd edition*. CRC Press, 2000 20

[136] Orloff, J. *Handbook of Charged Particle Optics, Second Edition*. CRC Press, 2008 20

[137] Landau, L and Lifshitz, E. *Mechanics*. Course of theoretical physics. Pergamon, 1960 21

[138] Nicholson, D. *Introduction to plasma theory*. Wiley series in plasma physics. Wiley, 1983 21

[139] Dawson, PH. Energetics of ions in quadrupole fields. *International Journal of Mass Spectrometry and Ion Physics*, 20(2–3):237–245, 1976. doi:10.1016/0020-7381(76)80152-0 21

[140] Szabo, I. New ion-optical devices utilizing oscillatory electric fields. I. Principle of operation and analytical theory of multipole devices with two-dimensional electric fields. *International Journal of Mass Spectrometry and Ion Processes*, 73(3):197–235, 1986. doi:10.1016/0168-1176(86)80001-5 22

[141] Hägg, C and Szabo, I. New ion-optical devices utilizing oscillatory electric fields. II. Stability of ion motion in a two-dimensional hexapole field. *International Journal of Mass Spectrometry and Ion Processes*, 73(3):237–275, 1986. doi:10.1016/0168-1176(86)80002-7 22

[142] Hägg, C and Szabo, I. New ion-optical devices utilizing oscillatory electric fields. III. Stability of ion motion in a two-dimensional octopole field. *International Journal of Mass Spectrometry and Ion Processes*, 73(3):277–294, 1986. doi:10.1016/0168-1176(86)80003-9 22

[143] Hägg, C and Szabo, I. New ion-optical devices utilizing oscillatory electric fields. IV. Computer simulations of the transport of an ion beam through an ideal quadrupole, hexapole, and octopole operating in the rf-only mode. *International Journal of Mass Spectrometry and Ion Processes*, 73(3):295–312, 1986. doi:10.1016/0168-1176(86)80004-0 22

[144] Gerlich, D. Inhomogeneous RF Fields: A Versatile Tool for the Study of Processes with Slow Ions. In CY Ng, M Baer, I Prigogine, and SA Rice, editors, *Advances in Chemical Physics*, pp. 1–176. John Wiley & Sons, Inc., 1992 22, 23, 25, 26

[145] Dehmelt, H and others. Radiofrequency spectroscopy of stored ions I: Storage. *Advances in Atomic and Molecular Physics*, 3:53–72, 1967 23

[146] Zahn, Uv. Präzisions-Massenbestimmungen mit dem elektrischen Massenfilter. *Zeitschrift für Physik*, 168(2):129–142, 1962. doi:10.1007/BF01379263 24

[147] Matsuda, H and Matsuo, T. A new method of producing an electric quadrupole field. *International Journal of Mass Spectrometry and Ion Physics*, 24(1):107–118, 1977. doi:10.1016/0020-7381(77)83008-8 24

[148] Tosi, P, et al. Transport of an ion beam through an octopole guide operating in the R.F.-only mode. *International Journal of Mass Spectrometry and Ion Processes*, 93(1):95–105, 1989. doi:10.1016/0168-1176(89)83077-0 24

[149] Xu, HJ, et al. A new cooling and focusing device for ion guide. *Nuclear Instruments and Methods in Physics Research Section A: Accelerators, Spectrometers, Detectors and Associated Equipment*, 333(2):274–281, 1993. doi:10.1016/0168-9002(93)91166-K 24

[150] Syed, SUAH, et al. Experimental Investigation of the 2D Ion Beam Profile Generated by an ESI Octopole-QMS System. *Journal of The American Society for Mass Spectrometry*, 25(10):1780–1787, 2014. doi:10.1007/s13361-014-0958-0 24

[151] Tolmachev, AV, Udseth, HR, and Smith, RD. Charge Capacity Limitations of Radio Frequency Ion Guides in Their Use for Improved Ion Accumulation and Trapping in Mass Spectrometry. *Analytical Chemistry*, 72(5):970–978, 2000. doi:10.1021/ac990729u 24

[152] Douglas, DJ and French, JB. Collisional focusing effects in radio frequency quadrupoles. *Journal of the American Society for Mass Spectrometry*, 3(4):398–408, 1992. doi:10.1016/1044-0305(92)87067-9 25

[153] Kellerbauer, A, et al. Buffer gas cooling of ion beams. *Nuclear Instruments and Methods in Physics Research Section A: Accelerators, Spectrometers, Detectors and Associated Equipment*, 469(2):276–285, 2001. doi:10.1016/S0168-9002(01)00286-8 25

[154] Shaffer, SA, et al. A novel ion funnel for focusing ions at elevated pressure using electrospray ionization mass spectrometry. *Rapid Communications in Mass Spectrometry*, 11(16):1813–1817, 1997. doi:10.1002/(SICI)1097-0231(19971030)11:16<1813::AID-RCM87>3.0.CO;2-D 26

[155] Shaffer, SA, et al. An Ion Funnel Interface for Improved Ion Focusing and Sensitivity Using Electrospray Ionization Mass Spectrometry. *Analytical Chemistry*, 70(19):4111–4119, 1998. doi:10.1021/ac9802170 26

[156] Kim, T, et al. Design and Implementation of a New Electrodynamic Ion Funnel. *Analytical Chemistry*, 72(10):2247–2255, 2000. doi:10.1021/ac991412x 26, 79

[157] Kelly, RT, et al. The ion funnel: Theory, implementations, and applications. *Mass Spectrometry Reviews*, 29(2):294–312, 2010. doi:10.1002/mas.20232 26, 79

[158] Tolmachev, AV, et al. Simulation-based optimization of the electrodynamic ion funnel for high sensitivity electrospray ionization mass spectrometry. *International Journal of Mass Spectrometry*, 203(1–3):31–47, 2000. doi:10.1016/S1387-3806(00)00265-7 26, 28

[159] Sernicola, NR. *Aufbau und Simulation einer Ionenoptik im Feinvakuum*. Bachelor's thesis, Technische Universität München, 2014 26, 59, 77, 79, 81

[160] Julian, RR, Mabbett, SR, and Jarrold, MF. Ion Funnels for the Masses: Experiments and Simulations with a Simplified Ion Funnel. *Journal of the American Society for Mass Spectrometry*, 16(10):1708–1712, 2005. doi:10.1016/j.jasms.2005.06.012 27

[161] Dawson, JM. Particle simulation of plasmas. *Reviews of Modern Physics*, 55(2):403–447, 1983. doi:10.1103/RevModPhys.55.403 28, 29

[162] Birdsall, CK and Langdon, AB. *Plasma Physics via Computer Simulation*. CRC Press, 2004 28

[163] Verboncoeur, JP. Particle simulation of plasmas: review and advances. *Plasma Physics and Controlled Fusion*, 47(5A):A231, 2005. doi:10.1088/0741-3335/47/5A/017 28

[164] Dahl, DA, Delmore, JE, and Appelhans, AD. SIMION PC/PS2 electrostatic lens design program. *Review of Scientific Instruments*, 61(1):607–609, 1990. doi:10.1063/1.1141932 28

[165] Dahl, DA. simion for the personal computer in reflection. *International Journal of Mass Spectrometry*, 200(1–3):3–25, 2000. doi:10.1016/S1387-3806(00)00305-5 28

[166] Manura, D and Dahl, D. *SIMION (R) 8.0 User Manual*. Scientific Instrument Services, Inc., NJ 08551, 2016 28, 29

[167] Lollobrigida, V, et al. Electron trajectory simulations of time-of-flight spectrometers for core level high-energy photoelectron spectroscopy at pulsed X-ray sources. *Journal of Electron Spectroscopy and Related Phenomena*, 205:98–105, 2015. doi:10.1016/j.elspec.2015.09.005 28

[168] Schiwietz, G, et al. The retarding Bessel-Box–An electron-spectrometer designed for pump/probe experiments. *Journal of Electron Spectroscopy and Related Phenomena*, 203:51–59, 2015. doi:10.1016/j.elspec.2015.06.011 28

[169] Schwartz, JC, Senko, MW, and Syka, JEP. A two-dimensional quadrupole ion trap mass spectrometer. *Journal of the American Society for Mass Spectrometry*, 13(6):659–669, 2002. doi:10.1016/S1044-0305(02)00384-7 28

[170] Han, F, et al. Computational fluid dynamics-Monte Carlo method for calculation of the ion trajectories and applications in ion mobility spectrometry. *International Journal of Mass Spectrometry*, 309:13–21, 2012. doi:10.1016/j.ijms.2011.08.017 28

[171] Appelhans, AD and Dahl, DA. SIMION ion optics simulations at atmospheric pressure. *International Journal of Mass Spectrometry*, 244(1):1–14, 2005. doi:10.1016/j.ijms.2005.03.010 28

[172] Tolmachev, AV, Udseth, HR, and Smith, RD. Modeling the ion density distribution in collisional cooling RF multipole ion guides. *International Journal of Mass Spectrometry*, 222(1–3):155–174, 2003. doi:10.1016/S1387-3806(02)00960-0 28

[173] Hasch, P and Schlichting, H. private communication, 2016 28

[174] Sydora, RD. Low-noise electromagnetic and relativistic particle-in-cell plasma simulation models. *Journal of Computational and Applied Mathematics*, 109(1–2):243–259, 1999. doi:10.1016/S0377-0427(99)00161-2 29

[175] Konenkov, NV, Sudakov, M, and Douglas, DJ. Matrix methods for the calculation of stability diagrams in quadrupole mass spectrometry. *Journal of the American Society for Mass Spectrometry*, 13(6):597–613, 2002. doi:10.1016/S1044-0305(02)00365-3 30

[176] Richards, JA, Huey, RM, and Hiller, J. A new operating mode for the quadrupole mass filter. *International Journal of Mass Spectrometry and Ion Physics*, 12(4):317–339, 1973. doi:10.1016/0020-7381(73)80102-0 30

[177] Sheretov, EP, et al. Hyperboloid mass spectrometers for space exploration. *International Journal of Mass Spectrometry*, 189(1):9–17, 1999. doi:10.1016/S1387-3806(99)00041-X 30

[178] Sterzl, S. *Aufbau und Charakterisierung eines neuartigen Hochfrequenz-Ionenleiters für hochmolekulare Ionen*. Bachelor's thesis, Technische Universität München, 2013 30, 59, 77, 81

[179] Sadat Kiai, SM, et al. Study of a quadrupole ion trap supplied with a periodic impulsional potential. *International Journal of Mass Spectrometry and Ion Processes*, 107(2):191–203, 1991. doi:10.1016/0168-1176(91)80058-U 30

[180] Sheretov, EP. Opportunities for optimization of the rf signal applied to electrodes of quadrupole mass spectrometers.: Part I. General theory. *International Journal of Mass Spectrometry*, 198(1–2):83–96, 2000. doi:10.1016/S1387-3806(00)00165-2 30

[181] Ding, L, Sudakov, M, and Kumashiro, S. A simulation study of the digital ion trap mass spectrometer. *International Journal of Mass Spectrometry*, 221(2):117–138, 2002. doi:10.1016/S1387-3806(02)00921-1 30

[182] Landais, B, et al. Varying the radio frequency: a new scanning mode for quadrupole analyzers. *Rapid Communications in Mass Spectrometry*, 12(6):302–306, 1998. doi:10.1002/(SICI)1097-0231(19980331)12:6<302::AID-RCM154>3.0.CO;2-U 30

[183] Schlunegger, UP, Stoeckli, M, and Caprioli, RM. Frequency scan for the analysis of high mass ions generated by matrix-assisted laser desorption/ionization in a Paul trap. *Rapid Communications in Mass Spectrometry*, 13(18):1792–1796, 1999. doi:10.1002/(SICI)1097-0231(19990930)13:18<1792::AID-RCM715>3.0.CO;2-S 30

[184] Sessoli, R, et al. High-spin molecules: [Mn12O12(O2CR)16(H2O)4]. *Journal of the American Chemical Society*, 115(5):1804–1816, 1993. doi:10.1021/ja00058a027 31

[185] Sessoli, R, et al. Magnetic bistability in a metal-ion cluster. *Nature*, 365(6442):141–143, 1993. doi:10.1038/365141a0 31

[186] Leuenberger, MN and Loss, D. Quantum computing in molecular magnets. *Nature*, 410(6830):789–793, 2001. doi:10.1038/35071024 31

[187] Ardavan, A, et al. Will Spin-Relaxation Times in Molecular Magnets Permit Quantum Information Processing? *Physical Review Letters*, 98(5):057201, 2007. doi:10.1103/PhysRevLett.98.057201 31

[188] Mannini, M, et al. Magnetic memory of a single-molecule quantum magnet wired to a gold surface. *Nature Materials*, 8(3):194–197, 2009. doi:10.1038/nmat2374 31

[189] Vitali, L, et al. Electronic Structure of Surface-supported Bis(phthalocyaninato) terbium(III) Single Molecular Magnets. *Nano Letters*, 8(10):3364–3368, 2008. doi:10.1021/nl801869b 32

[190] Branzoli, F, et al. Spin Dynamics in the Negatively Charged Terbium (III) Bis-phthalocyaninato Complex. *Journal of the American Chemical Society*, 131(12):4387–4396, 2009. doi:10.1021/ja808649g 32

[191] Stepanow, S, et al. Spin and Orbital Magnetic Moment Anisotropies of Monodispersed Bis(Phthalocyaninato)Terbium on a Copper Surface. *Journal of the American Chemical Society*, 132(34):11900–11901, 2010. doi:10.1021/ja105124r 32

[192] Lodi Rizzini, A, et al. Coupling Single Molecule Magnets to Ferromagnetic Substrates. *Physical Review Letters*, 107(17):177205, 2011. doi:10.1103/PhysRevLett.107.177205 32

[193] Ganzhorn, M, et al. Strong spin-phonon coupling between a single-molecule magnet and a carbon nanotube nanoelectromechanical system. *Nature Nanotechnology*, 8(3):165–169, 2013. doi:10.1038/nnano.2012.258 32

[194] Komeda, T, et al. Variation of Kondo Peak Observed in the Assembly of Heteroleptic 2,3-Naphthalocyaninato Phthalocyaninato Tb(III) Double-Decker Complex on Au(111). *ACS Nano*, 7(2):1092–1099, 2013. doi:10.1021/nn304035h 32

[195] Dreiser, J, et al. Exchange Interaction of Strongly Anisotropic Tripodal Erbium Single-Ion Magnets with Metallic Surfaces. *ACS Nano*, 8(5):4662–4671, 2014. doi:10.1021/nn500409u 32

[196] Komeda, T, Katoh, K, and Yamashita, M. Double-decker phthalocyanine complex: Scanning tunneling microscopy study of film formation and spin properties. *Progress in Surface Science*, 89(2):127–160, 2014. doi:10.1016/j.progsurf.2014.03.001 32

[197] Woodruff, DN, Winpenny, REP, and Layfield, RA. Lanthanide Single-Molecule Magnets. *Chemical Reviews*, 113(7):5110–5148, 2013. doi:10.1021/cr400018q 32

[198] Gimenez-Agulla, N, et al. Single-Molecule-Magnet Behavior in the Family of [Ln(OETAP)2] Double-Decker Complexes (Ln=Lanthanide, OETAP=Octa(ethyl)tetraazaporphyrin). *Chemistry – A European Journal*, 20(40):12817–12825, 2014. doi:10.1002/chem.201402869 32

[199] Otsuki, J, et al. Rotational Libration of a Double-Decker Porphyrin Visualized. *Journal of the American Chemical Society*, 132(20):6870–6871, 2010. doi:10.1021/ja907077e 32

[200] Écija, D, et al. Assembly and Manipulation of Rotatable Cerium Porphyrinato Sandwich Complexes on a Surface. *Angewandte Chemie International Edition*, 50(17):3872–3877, 2011. doi:10.1002/anie.201007370 32

[201] Cirera, B, et al. Characterization of Surface-Decoupled Double-Decker Complexes on Coinage Metals, In preparation 33, 34, 35, 49

[202] Held, G. Low-energy electron diffraction crystallography of surfaces and interfaces. *Bunsen-Magazin 12*, (12):124–131, 2010 34, 44, 47

[203] Böhringer, M, et al. Adsorption site determination of PTCDA on Ag(110) by manipulation of adatoms. *Surface Science*, 419(1):L95–L99, 1998. doi:10.1016/S0039-6028(98)00733-X 35

[204] Bieri, M, et al. Two-Dimensional Polymer Formation on Surfaces: Insight into the Roles of Precursor Mobility and Reactivity. *Journal of the American Chemical Society*, 132(46):16669–16676, 2010. doi:10.1021/ja107947z 36

[205] Mendez, J, Lopez, MF, and Martin-Gago, JA. On-surface synthesis of cyclic organic molecules. *Chemical Society Reviews*, 40(9):4578–4590, 2011. doi:10.1039/C0CS00161A 36

[206] Inose, T, et al. Switching of Single-Molecule Magnetic Properties of TbIII–Porphyrin Double-Decker Complexes and Observation of Their Supramolecular Structures on a Carbon Surface. *Chemistry – A European Journal*, 20(36):11362–11369, 2014. doi:10.1002/chem.201402669 39

[207] Tseng, TC, et al. Charge-transfer-induced structural rearrangements at both sides of organic/metal interfaces. *Nature Chemistry*, 2(5):374–379, 2010. doi:10.1038/nchem.591 40, 45

[208] Boffetta, P, Jourenkova, N, and Gustavsson, P. Cancer risk from occupational and environmental exposure to polycyclic aromatic hydrocarbons. *Cancer Causes & Control*, 8(3):444–472, 1997. doi:10.1023/A:1018465507029 41

[209] Mastral, AM and Callén, MS. A Review on Polycyclic Aromatic Hydrocarbon (PAH) Emissions from Energy Generation. *Environmental Science & Technology*, 34(15):3051–3057, 2000. doi:10.1021/es001028d 41

[210] Vijh, UP, Witt, AN, and Gordon, KD. Discovery of Blue Luminescence in the Red Rectangle: Possible Fluorescence from Neutral Polycyclic Aromatic Hydrocarbon Molecules? *The Astrophysical Journal Letters*, 606(1):L65, 2004. doi:10.1086/421106 41

[211] Tielens, A. Interstellar Polycyclic Aromatic Hydrocarbon Molecules*. *Annual Review of Astronomy and Astrophysics*, 46(1):289–337, 2008. doi:10.1146/annurev.astro.46.060407.145211 41

[212] Gredel, R, et al. Abundances of PAHs in the ISM: confronting observations with experimental results. *Astronomy & Astrophysics*, 530:A26, 2011. doi:10.1051/0004-6361/201116602 41

[213] Birks, JB. Excimers. *Reports on Progress in Physics*, 38(8):903, 1975. doi:10.1088/0034-4885/38/8/001 41

[214] Park, YH, et al. Theoretical investigation of tetra-substituted pyrenes for organic light emitting diodes. *Current Applied Physics*, 6(4):691–694, 2006. doi:10.1016/j.cap.2005.04.021 41

[215] Lo, MY, et al. Organic-Inorganic Hybrids Based on Pyrene Functionalized Octavinylsilsesquioxane Cores for Application in OLEDs. *Journal of the American Chemical Society*, 129(18):5808–5809, 2007. doi:10.1021/ja070471m 41

[216] Figueira-Duarte, TM and Müllen, K. Pyrene-Based Materials for Organic Electronics. *Chemical Reviews*, 111(11):7260–7314, 2011. doi:10.1021/cr100428a 41

[217] Lee, OP, et al. Efficient Small Molecule Bulk Heterojunction Solar Cells with High Fill Factors via Pyrene-Directed Molecular Self-Assembly. *Advanced Materials*, 23(45):5359–5363, 2011. doi:10.1002/adma.201103177 41

[218] Nakashima, N, Tomonari, Y, and Murakami, H. Water-Soluble Single-Walled Carbon Nanotubes via Noncovalent Sidewall-Functionalization with a Pyrene-Carrying Ammonium Ion. *Chemistry Letters*, (6):638–638, 2002. doi:10.1246/cl.2002.638 41

[219] Zhang, J, et al. Photoluminescence and Electronic Interaction of Anthracene Derivatives Adsorbed on Sidewalls of Single-Walled Carbon Nanotubes. *Nano Letters*, 3(3):403–407, 2003. doi:10.1021/nl025952c 41

[220] Ehli, C, et al. Interactions in Single Wall Carbon Nanotubes/Pyrene/Porphyrin Nanohybrids. *Journal of the American Chemical Society*, 128(34):11222–11231, 2006. doi:10.1021/ja0624974 41

[221] Ramakrishna Matte, HSS, et al. Quenching of fluorescence of aromatic molecules by graphene due to electron transfer. *Chemical Physics Letters*, 506(4–6):260–264, 2011. doi:10.1016/j.cplett.2011.03.031 41

[222] Zhang, X, et al. Morphology-Controllable Synthesis of Pyrene Nanostructures and Its Morphology Dependence of Optical Properties. *The Journal of Physical Chemistry B*, 109(40):18777–18780, 2005. doi:10.1021/jp052385j 41

[223] Endo, M, et al. Pyrene-Stacked Nanostructures Constructed in the Recombinant Tobacco Mosaic Virus Rod Scaffold. *Chemistry – A European Journal*, 12(14):3735–3740, 2006. doi:10.1002/chem.200501309 41

[224] Ferris, DP, et al. Light-Operated Mechanized Nanoparticles. *Journal of the American Chemical Society*, 131(5):1686–1688, 2009. doi:10.1021/ja807798g 41

[225] Llanes-Pallas, A, et al. Engineering of Supramolecular H-Bonded Nanopolygons via Self-Assembly of Programmed Molecular Modules. *Journal of the American Chemical Society*, 131(2):509–520, 2009. doi:10.1021/ja807530m 41, 42

[226] Stylianou, KC, et al. A Guest-Responsive Fluorescent 3D Microporous Metal-Organic Framework Derived from a Long-Lifetime Pyrene Core. *Journal of the American Chemical Society*, 132(12):4119–4130, 2010. doi:10.1021/ja906041f 41

[227] Sezi, S and Wagenknecht, HA. DNA-templated formation of fluorescent self-assembly of ethynyl pyrenes. *Chemical Communications*, 49(81):9257–9259, 2013. doi:10.1039/C3CC44733B 41

[228] Wang, D, et al. Adlayer structures of pyrene and perylene on Cu (111): an in situ STM study. *Surface science*, 478(1):L320–L326, 2001 41

[229] France, CB and Parkinson, BA. Naphtho[2,3-a]pyrene Forms Chiral Domains on Au(111). *Journal of the American Chemical Society*, 125(42):12712–12713, 2003. doi:10.1021/ja037056o 41

[230] Yip, HL, et al. Two-Dimensional Self-Assembly of 1-Pyrylphosphonic Acid: Transfer of Stacks on Structured Surface. *Journal of the American Chemical Society*, 128(17):5672–5679, 2006. doi:10.1021/ja0563152 41

[231] Zhang, Xm, et al. Triphenylene Substituted Pyrene Derivative: Synthesis and Single Molecule Investigation. *The Journal of Physical Chemistry C*, 117(1):307–312, 2013. doi:10.1021/jp3095616 41

[232] Pham, TA, et al. Self-assembly of pyrene derivatives on Au(111): substituent effects on intermolecular interactions. *Chemical Communications*, 50(91):14089–14092, 2014. doi:10.1039/C4CC02753A 41

[233] Mistry, A, et al. The Synthesis and STM/AFM Imaging of 'Olympicene' Benzo[cd]pyrenes. *Chemistry – A European Journal*, 21(5):2011–2018, 2015. doi:10.1002/chem.201404877 41

[234] Kaposi, T, et al. Supramolecular spangling, crocheting and knitting of functionalized pyrene molecules on a silver surface, Submitted to ACS Nano 41, 52

[235] Hoh, T. *Scanning Tunneling Microscopy Investigations of Functionalized Pyrenes and Quaterphenyls on Metal and Insulating Substrates*. Bachelor's thesis, Technische Universität München, 2013 42

[236] Piot, L, et al. Selective Formation of Bi-Component Arrays Through H-Bonding of Multivalent Molecular Modules. *Advanced Functional Materials*, 19(8):1207–1214, 2009. doi:10.1002/adfm.200801419 42

[237] Heim, D, et al. Self-Assembly of Flexible One-Dimensional Coordination Polymers on Metal Surfaces. *Journal of the American Chemical Society*, 132(19):6783–6790, 2010. doi:10.1021/ja1010527 42

[238] Ecija, D, et al. Hierarchic Self-Assembly of Nanoporous Chiral Networks with Conformationally Flexible Porphyrins. *ACS Nano*, 4(8):4936–4942, 2010. doi:10.1021/nn1013337 42

[239] Kepler, J. *Harmonices mundi libri V*. 1619 46

[240] Zavitsas, AA. The Relation between Bond Lengths and Dissociation Energies of Carbon-Carbon Bonds. *The Journal of Physical Chemistry A*, 107(6):897–898, 2003. doi:10.1021/jp0269367 48

[241] Alshareef, AH, et al. Effect of Chemical Structure on the Cracking and Coking of Archipelago Model Compounds Representative of Asphaltenes. *Energy & Fuels*, 26(3):1828–1843, 2012. doi:10.1021/ef300035p 48

[242] Markopoulos, G and Grunenberg, J. Predicting Kinetically Unstable C-C Bonds from the Ground-State Properties of a Molecule. *Angewandte Chemie International Edition*, 52(40):10648–10651, 2013. doi:10.1002/anie.201303821 48

[243] Blake, E, et al. Thermal Stability as a Function of Chemical Structure. *Journal of Chemical & Engineering Data*, 6(1):87–98, 1961. doi:10.1021/je60009a020 48

[244] Johns, IB, McElhill, EA, and Smith, JO. Thermal Stability of Some Organic Compounds. *Journal of Chemical & Engineering Data*, 7(2):277–281, 1962. doi:10.1021/je60013a036 48

[245] Korshak, VV, Khomutov, VA, and Doroshenko, YY. A study of thermal stability in a number of aromatic and nitrogen containing polycyclic compounds. *Polymer Science USSR*, 18(3):597–603, 1976. doi:10.1016/0032-3950(76)90253-7 48

[246] Fanelli, D. Negative results are disappearing from most disciplines and countries. *Scientometrics*, 90(3):891–904, 2011. doi:10.1007/s11192-011-0494-7 48

[247] Ioannidis, JPA. Why Most Published Research Findings Are False. *PLoS Med*, 2(8):e124, 2005. doi:10.1371/journal.pmed.0020124 48

[248] Prinz, F, Schlange, T, and Asadullah, K. Believe it or not: how much can we rely on published data on potential drug targets? *Nature Reviews Drug Discovery*, 10(9):712–712, 2011. doi:10.1038/nrd3439-c1 48

[249] Begley, CG and Ellis, LM. Drug development: Raise standards for preclinical cancer research. *Nature*, 483(7391):531–533, 2012. doi:10.1038/483531a 48

[250] Kay, AW, et al. Multi-atom resonant photoemission. *Journal of Electron Spectroscopy and Related Phenomena*, 114–116:1179–1189, 2001. doi:10.1016/S0368-2048(00)00429-1 48

[251] Amsler, C, et al. Review of Particle Physics. *Physics Letters B*, 667(1–5):1–6, 2008. doi:10.1016/j.physletb.2008.07.018 48

[252] Bischoff, F and Gimenez-Agullo, N. private communication, 2015 50

[253] Kröger, I, et al. Submonolayer growth of copper-phthalocyanine on Ag(111). *New Journal of Physics*, 12(8):083038, 2010. doi:10.1088/1367-2630/12/8/083038 50

[254] Zeitouny, J, et al. On the route to mimic natural movements: synthesis and photophysical properties of a molecular arachnoid. *Chemical Communications*, 47(1):451–453, 2010. doi:10.1039/C0CC03045G 52

[255] Marangoni, T, et al. Thermosolutal Self-Organization of Supramolecular Polymers into Nanocraters. *Langmuir*, 27(4):1513–1523, 2011. doi:10.1021/la104276y 52

[256] Yoosaf, K, et al. From Molecular to Macroscopic Engineering: Shaping Hydrogen-Bonded Organic Nanomaterials. *Chemistry – A European Journal*, 17(11):3262–3273, 2011. doi:10.1002/chem.201002103 52

[257] Forstmann, F, Berndt, W, and Büttner, P. Determination of the Adsorption Site by Low-Energy Electron Diffraction for Iodine on Silver (111). *Physical Review Letters*, 30(1):17–19, 1973. doi:10.1103/PhysRevLett.30.17 53

[258] Lindon, J. *Encyclopedia of Spectroscopy and Spectrometry*. Elsevier Science, 2010 54

[259] Leblebici, SY, et al. Near-Infrared Azadipyrromethenes as Electron Donor for Efficient Planar Heterojunction Organic Solar Cells. *ACS Applied Materials & Interfaces*, 3(11):4469–4474, 2011. doi:10.1021/am201157d 56

[260] Leblebici, SY, et al. Reducing Exciton Binding Energy by Increasing Thin Film Permittivity: An Effective Approach To Enhance Exciton Separation Efficiency in Organic Solar Cells. *ACS Applied Materials & Interfaces*, 5(20):10105–10110, 2013. doi:10.1021/am402744k 56

[261] Steinacher, R. *Development of Soft Landing Instrumentation for SPM Investigation*. Master's thesis, Technische Universität München, 2012 59, 77

[262] Buberl, T. *Charakterisierung neuartiger Ionenleiter für ionenstrahlgestützte Deposition: Experiment und Simulation*. Bachelor's thesis, Technische Universität München, 2013 59, 81

[263] Reinisch, D. *Entwurf und Aufbau einer ESI-Quelle*. Bachelor's thesis, Technische Universität München, 2013 59

[264] Sigl, L. *Probenpräparation für ionenstrahlgestützte Deposition und Rastersondenmikroskopie*. Bachelor's thesis, Technische Universität München, 2014 59, 95

[265] Walz, M. *Design of an electronic control unit for an ESIBD System*. Master's thesis, Technische Universität München, 2015 59, 88, 89

[266] Page, JS, et al. Subambient Pressure Ionization with Nanoelectrospray Source and Interface for Improved Sensitivity in Mass Spectrometry. *Analytical Chemistry*, 80(5):1800–1805, 2008. doi:10.1021/ac702354b 63

[267] Marginean, I, et al. Achieving 50% Ionization Efficiency in Subambient Pressure Ionization with Nanoelectrospray. *Analytical Chemistry*, 82(22):9344–9349, 2010. doi:10.1021/ac1019123 63

[268] Wilm, M and Mann, M. Analytical Properties of the Nanoelectrospray Ion Source. *Analytical Chemistry*, 68(1):1–8, 1996. doi:10.1021/ac9509519 64

[269] Gamero-Castano, M, et al. On the current emitted by Taylor cone-jets of electrolytes in vacuo: Implications for liquid metal ion sources. *Journal of Applied Physics*, 83(5):2428–2434, 1998. doi:10.1063/1.367002 64

[270] Lieberman, M and Lichtenberg, A. *Principles of Plasma Discharges and Materials Processing*. Wiley, 2005 65, 66

[271] Slade, P and Taylor, E. Electrical breakdown in atmospheric air between closely spaced (0.2 μm-40 μm) electrical contacts. *IEEE Transactions on Components and Packaging Technologies*, 25(3):390–396, 2002. doi:10.1109/TCAPT.2002.804615 66

[272] Rauschenbach, S and Rinke, G. private communication, 2012 67

[273] Pauly, M, et al. A hydrodynamically optimized nano-electrospray ionization source and vacuum interface. *The Analyst*, 139(8):1856, 2014. doi:10.1039/c3an01836a 69

[274] El-Faramawy, A, Siu, KWM, and Thomson, BA. Efficiency of Nano-Electrospray Ionization. *Journal of the American Society for Mass Spectrometry*, 16(10):1702–1707, 2005. doi:10.1016/j.jasms.2005.06.011 69

[275] Page, JS, et al. Biases in Ion Transmission Through an Electrospray Ionization-Mass Spectrometry Capillary Inlet. *Journal of the American Society for Mass Spectrometry*, 20(12):2265–2272, 2009. doi:10.1016/j.jasms.2009.08.018 69

[276] Walz, A. private communication, 2016 70

[277] O'Hanlon, J. *A User's Guide to Vacuum Technology*. John Wiley & Sons, 2003 70

[278] Jousten, K. *Handbook of Vacuum Technology*. John Wiley & Sons, 2008 70, 72, 73

[279] Tamenori, Y. Development of a differential pumping system for soft X-ray beamlines for windowless experiments under normal atmospheric conditions. *Journal of Synchrotron Radiation*, 17(2):243–249, 2010. doi:10.1107/S0909049509052571 71

[280] Miller, DR. Free jet sources. In G Scoles, editor, *Atomic and molecular beam methods*, vol. 1. Oxford University Press: New York, 1988 72

[281] Bomelburg, HJ. Estimation of gas leak rates through very small orifices and channels. Tech. rep., Battelle Pacific Northwest Labs., 1977 72

[282] Haaland, SE. Simple and Explicit Formulas for the Friction Factor in Turbulent Pipe Flow. *Journal of Fluids Engineering*, 105(1):89–90, 1983. doi:10.1115/1.3240948 73

[283] Ogletree, DF, et al. A differentially pumped electrostatic lens system for photoemission studies in the millibar range. *Review of Scientific Instruments*, 73(11):3872–3877, 2002. doi:10.1063/1.1512336 74

[284] Pozar, DM. *Microwave Engineering*. John Wiley & Sons, 2012 86

[285] Feulner, P and Menzel, D. Simple ways to improve "flash desorption" measurements from single crystal surfaces. *Journal of Vacuum Science & Technology*, 17(2):662–663, 1980. doi:http://dx.doi.org/10.1116/1.570537 95

[286] Schlichting, H and Menzel, D. Techniques for wide range, high resolution and precision, thermal desorption measurements: I. Principles of apparatus and operation. *Surface Science*, 285(3):209 – 218, 1993. doi:http://dx.doi.org/10.1016/0039-6028(93)90431-I 95

[287] Auwärter, W, et al. Porphyrins at interfaces. *Nature Chemistry*, 7(2):105–120, 2015 97

[288] Jiang, L, Walz, A, and Zhang, B. private communication, 2016 98

[289] Wiengarten, A, et al. Surface-assisted dehydrogenative homocoupling of porphine molecules. *Journal of the American Chemical Society*, 136(26):9346–9354, 2014 99

[290] Horcas, I, et al. WSXM: A software for scanning probe microscopy and a tool for nanotechnology. *Review of Scientific Instruments*, 78(1):013705, 2007. doi:10.1063/1.2432410 105

Acknowledgment

First and foremost, my deepest and very personal gratitude goes to my family for their unwavering love and support all these years, especially my wife Marlene, to whom I dedicate this work. The stuff you guys had to put up with...

On a more professional level I am greatly indebted to an illustrious group of people for various reasons, all of whom I've had the great pleasure of becoming acquainted with. In no logical or chronological order these are:

Andi and Michi Walz, who are masterminds in finding mechanical and IT solutions, respectively, and solving problems in general, and the best M.Sc. students and lab partners one can possibly hope for. In addition to them, it has been a great pleasure to collaborate with Theresa Buberl, Julian Lloyd, Seung Cheol Oh, David Reinisch, Nicolo Sernicola, Lukas Sigl, Richard Steinacher, and Sabrina Sterzl on the ESIBD system. The same goes for projects at the STM, where Martin Schwarz, Nacho Urgel, Alissa Wiengarten, and Domenik Zimmermann always created an enjoyable and relaxed working atmosphere. Special thanks are extended in this experimental regard to Felix Bischoff, Karl Eberle, Li Jiang, Mateusz Paszkiewicz, and Bodong Zhang, who all made significant contributions to measurements on machines which I lacked the necessary expertise for.

Johannes Barth, who gave me both the opportunity to work on a fiendishly challenging project, as well as unquestioning support when things looked questionable. Hartmut Schlichting, for teaching me a whole new spectrum of skills both theoretical and practical, and extending a level of sympathy and understanding, which, quite frankly, I haven't really earned. Peter Feulner, for an inestimable amount of advice, both professional and personal, and many inspiring and fruitful discussions during lunch and over a sip of "coffee". Willi Auwärter, for being a great supervisor and teaching me a lot about STM and rigorous experimental practice. Joachim Reichert, for fruitful discussions, support during the ESIBD preparations, and a very enjoyable teaching collaboration. Flo Klappenberger and CA Palma, for their support with XPS measurements and discus-

sions removing the scales from my eyes regarding a career in science. All post-docs not mentioned so far (Alex, Anthoula, David, David (not a typo), Francesco, Knud, Manuela, Özge, Yiqi, Yuanyuan), for a generally enjoyable working environment and great company.

This work would have been impossible without the help and profound expertise of a number of very talented and motivated people, who made things possible very quickly which would otherwise have cost a significant amount of time and nerves. The two Karls, Kölbl and Eberle, savants in all things metal and vacuum, respectively. Reinhold Schneider, who can solder contacts invisible to the naked eye and holds sway over an unfathomable repository of (somtimes exotic) electronic spare parts. Max Glanz and Viktoria Blaschek, for unquestioning help and support with IT and administrative problems. All employees of the E11, E15, and central chemistry and physics machine shops, for many a part quickly made, and advice in mechanical matters. It is a true pity that this kind of service is regarded so lowly nowadays and more and more technical assistant positions are being axed every year.

Finally, the last few years have been made all the more worthwhile by an amazingly cooperative spirit and fun atmosphere among the students, especially Flo (you sneaky bastard!) and the other office mates Andi, Nacho, Peter and Runyuan, but also some very important people from other offices and the "Kofferraum": Alissa, Claudia, Daniel, Felix, Jacob, Kathi, Mateusz, Martin, Martin, Martin (not a typo either), Michi, Murat, Nenad, Peter, Sybille, Tobias, Wastl, and Wolfgang. It's hard to find suitable words to describe this feeling of camaraderie, although many a good one surely has been exchanged during lunch breaks and other opportunities, time and again. Woe be unto me if I should have forgotten anyone and a beer unto that person who feels wronged by being left out of this collection of awesome people. I hope I have given to the group at least some bit of what I have gained from your friendship. Good memories.